Spring 1-1-2011

Atmospheric Coupling Through Gravity Waves During Stratospheric Sudden Warmings: Gravity Wave Variations, Generation Mechanisms, and Impacts

Chihoko Yamashita
University of Colorado at Boulder, yamashic@colorado.edu

Recommended Citation

Yamashita, Chihoko, "Atmospheric Coupling Through Gravity Waves During Stratospheric Sudden Warmings: Gravity Wave Variations, Generation Mechanisms, and Impacts" (2011). *Aerospace Engineering Sciences Graduate Theses & Dissertations*. 39.
https://scholar.colorado.edu/asen_gradetds/39

Atmospheric Coupling Through Gravity Waves During Stratospheric Sudden Warmings: Gravity Wave Variations, Generation Mechanisms, and Impacts

by

Chihoko Yamashita

B.S., Nihon University, 2004

M.S., University of Colorado, 2008

A thesis submitted to the

Faculty of the Graduate School of the

University of Colorado in partial fulfillment

of the requirements for the degree of

Doctor of Philosophy

Department of Aerospace Engineering Sciences

2011

This thesis entitled:
Atmospheric Coupling Through Gravity Waves During Stratospheric Sudden Warmings: Gravity Wave Variations, Generation Mechanisms, and Impacts
written by Chihoko Yamashita
has been approved for the Department of Aerospace Engineering Sciences

Professor Xinzhao Chu (Chair)

Professor Han-Li Liu

Date ____________________

The final copy of this thesis has been examined by the signatories, and we find that both the content and the form meet acceptable presentation standards of scholarly work in the above mentioned discipline.

Yamashita, Chihoko (Ph.D., Aerospace Engineering Sciences)

Atmospheric Coupling Through Gravity Waves During Stratospheric Sudden Warmings: Gravity Wave Variations, Generation Mechanisms, and Impacts

Thesis directed by Professors Han-Li Liu and Xinzhao Chu

Full understanding of gravity wave influences on the middle and upper atmosphere remains an unresolved research topic. The goals of this work are two-fold. First, gravity wave sources and propagation characteristics are explored using assimilated meteorological analyses from the European Centre for Medium-Range Weather Forecasting (ECMWF) during the 2009 stratospheric sudden warming (SSW). Second, gravity wave impacts on polar temperatures in the middle and upper atmosphere are examined by modulating the gravity wave parameterization scheme in the Thermosphere-Ionosphere-Mesosphere-Electrodynamics General Circulation Model (TIME-GCM). Gravity waves that are resolved in ECMWFT799 are validated with satellite and lidar observations.

ECMWF gravity wave potential energy density (GW-Ep) shows two enhancements, on January 5 and 15–22, prior to the peak 2009 SSW on January 23–24. The two gravity wave enhancements are associated with the amplifications of planetary wave 1 and wave 2, respectively, and there is a sudden decay of GW-Ep after the peak 2009 SSW. GW-Ep enhancements prior to the SSW correspond well with the positive vertical gradients of total perturbation energy flux (F_E), indicating an in-situ energy source. The spatial and temporal distributions of gravity wave activities correlate with those of the residual tendencies introduced by Snyder et al. [2009]. These results suggest that the two peaks of GW-Ep are caused by the enhancements of the wave excitation in the stratosphere due to the residual tendency forcings.

The sudden decay of gravity wave amplitudes correlates well with the suppressions of gravity wave propagation from the troposphere to the stratosphere obtained from the ray-tracing model. In addition, the vertical derivatives of F_E decay after January 22. These results indicate that the sudden decay of gravity waves after the wind reversal is likely due to suppressions of gravity wave propagation from the troposphere along with the reductions of in-situ gravity wave excitation by the polar night jet.

The responses of the mesosphere and lower thermosphere (MLT) temperatures to gravity waves during SSWs are investigated using TIME-GCM through modifying gravity wave parameters. This study confirms that the height of gravity wave forcing region is mainly determined by gravity wave amplitude and wavelength, and the vertical depth is closely tied to the spectral width of gravity wave phase speed. The gravity wave forcings control the pattern and strength of residual circulation and thereby the characteristics of MLT cooling and warming regions. The planetary wave forcings in the MLT also affect the vertical depth and magnitude of MLT temperature anomalies through further modifying the residual circulation. These planetary wave forcings are likely generated in-situ by the gravity wave forcings at high latitudes. Therefore, the mechanisms of gravity wave controlling the MLT temperature during a SSW are directly through gravity wave forcing and indirectly through generating planetary waves in-situ.

Realistic gravity wave variations during the 2009 SSW obtained from ECMWF-T799 are implemented in TIME-GCM. The following two simulations are examined. Case 1 includes the enhanced gravity waves with longitudinal variations. Case 2 suppresses gravity waves with horizontal wavelength longer than 150 km. Both cases improve the TIME-GCM simulations of the MLT temperature responses to the 2009 SSW, indicating that realistic gravity wave variations have impacts on the MLT thermal structure.

Dedication

For their continuous encouragement, support, and unconditional love, I dedicate this dissertation to my parents Masanori and Kazuyo, my brother Hirohisa, and my sister Yukiko.

Acknowledgements

I would like to extend my utmost gratitude to my two advisors, Professor Xinzhao Chu and Dr. Hanli Liu. Professor Chu's instruction in the areas of atmospheric science and lidar observation was of paramount importance to my success. Though not directly displayed in this dissertation, her work as a mentor, investing her time in me and always ready with support and advice, made this dissertation possible. Working with my NCAR advisor, Dr. Liu, has been a great honor for me as well as his knowledge and boundless ideas regarding atmospheric dynamics have provided insight that has been invaluable throughout this work. I want to thank you both for your continuous guidance, support, and patience.

I am very grateful to my committee members, Dr. Lynn Harvey, Professor Walter Robinson, and Professor Jeffrey Forbes for their support of my research and my dissertation. I also would like to acknowledge Dr. Chris Snyder at NCAR/MMM and Professor Varavut Limpasuvan at Coastal Carolina University for their advice on the study of gravity waves. Dr. Peter Bechtold kindly ran the ECMWF model to provide the high temporal resolution ECMWF, and Dr. Steven Eckermann provided the GROGRAT ray-tracing model.

I would like to extend a thank you to my colleagues and friends: Drs. Loren Chang, Amal Chandran, Tzu-Wei Fang, Xian Lu, Wentao Huang, and Evan Cullens. I am thankful for my parents, brother, and sister for their encouragement and support during my graduate studies.

Finally, I am sincerely grateful to the National Center for Atmospheric Research (NCAR) / High Altitude Observatory (HAO) Newkirk Graduate Fellowship for its generous support during the four years of my Ph.D. research and the opportunity to work with the amazing scientists there.

Contents

Chapter

1 Introduction 1

1.1 Gravity Waves 2
1.2 Stratospheric Sudden Warming 7
1.3 Research Objective 13
1.4 Outline of Thesis 14

2 Validations of Gravity Waves Resolved in ECMWF-T799 16

2.1 ECMWF 16
2.2 Background of Gravity Waves in ECMWF 18
2.3 Analysis Methods 22
  2.3.1 ECMWF Data Analysis Method 22
  2.3.2 Lidar Data Analysis 23
  2.3.3 COSMIC/GPS Data Analysis 24
2.4 Comparison of Analysis and Forecast Versions within ECMWF-T799 25
2.5 Validations with lidar and GPS for Seasonal Variations 25
2.6 Short Term Variations 30
  2.6.1 Validations with COSMIC/GPS 30
  2.6.2 Validations with GEOS-5 and ARPS models 30
2.7 Conclusions 36

3 Gravity Wave Variations during the 2009 SSW 37

3.1 Introduction 37

3.2 The 2009 Stratospheric Sudden Warming 39

3.3 Gravity Wave Variations during the 2009 SSW 39

3.4 Conclusions 49

4 Physical Mechanisms of Gravity Wave Variations during the 2009 SSW 50

4.1 Introduction 50

4.2 Gravity Wave Propagation and Source 53

4.2.1 Orographic Gravity Waves 54

4.2.2 Nonorographic Gravity Waves 58

4.2.3 Propagation of Convective Gravity Waves from the Tropics to Polar Region . 60

4.2.4 In-situ Gravity Wave Sources 63

4.3 In-situ Gravity Wave Generations 68

4.3.1 Temporal and Spatial Variations of Residual Tendencies 68

4.3.2 Case Study of In-situ Wave Generations 75

4.3.3 Shear Instability 86

4.4 Conclusions 87

5 Sensitivity Study of the MLT Temperature Responses to Gravity Wave Forcing during SSWs 89

5.1 Introduction 89

5.2 TIME-GCM 92

5.3 Responses of the MLT Temperatures to Gravity Wave Forcing during Stratospheric Sudden Warming 94

5.3.1 Profile Study using Gravity Wave Parameterization Scheme 94

5.3.2 Temperature Anomaly in TIME-GCM 94

5.3.3 Residual Circulation Induced by Gravity Wave and Planetary Wave Forcings 97

5.4 Roles of Gravity Waves in Downward Progression of Temperature Anomaly 101

5.5 Conclusions 106

6 Impacts of Gravity Wave Variations on the Upper Atmosphere for the 2009 Stratospheric Sudden Warming 108

6.1 Introduction 108

6.2 Method 111

6.3 TIME-GCM: Base Case 114

6.4 TIME-GCM: Control Case 1 117

6.5 TIME-GCM: Control Case 2 120

6.6 Discussion 123

6.7 Conclusions 125

7 Conclusions and Outlook 127

7.1 Conclusions 127

7.2 Future Work 131

Bibliography 135

Appendix

A Comparison of Gravity Wave Variations during the 2009 and the 2010 SSWs 145

Tables

Table

5.1 Gravity wave parameters used in TIME-GCM simulations 93

Figures

Figure

1.1 CIRA climatology of zonal mean flow 4
1.2 Schematics depicting the influence of gravity wave drag on the wind structure during summer and winter 4
1.3 The mechanisms of SSWs 8
1.4 Schematics illustrating global impacts due to SSWs 10
1.5 Schematics of changes in gravity wave filtering during SSWs 12
1.6 Schematics illustrating temperature anomalies induced by atmospheric waves during SSWs 12

2.1 Schematics of ECMWF model level 17
2.2 Comparisons between the model level and pressure level 18
2.3 Comparison among ECMWF-T799, WRF, and AIRS 20
2.4 Comparison between AIRS satellite and ECMWF-T799 21
2.5 Antarctica map with major lidar stations 23
2.6 Comparison between analysis and forecast versions 1 26
2.7 Comparison between analysis and forecast versions 2 26
2.8 Comparison between the lidar observations and ECMWF-T799 in Antarctica 27
2.9 Climatology of gravity waves from ECMWF-T799 29
2.10 Climatology of gravity waves from CHAMP/GPS observations 29

2.11 Comparison between COSMIC/GPS observations and ECMWF-T799 31

2.12 Comparison between GEOS-5 and ECMWF-T799 33

2.13 Comparison between ARPS model and ECMWF-T799 1 34

2.14 Comparison between ARPS model and ECMWF-T799 2 35

3.1 Stratospheric Sudden warming in 2009 40

3.2 Comparison between SABER and ECMWF-T799 41

3.3 Evolutions of gravity waves during the 2009 SSW 43

3.4 Variations of GW-Ep during the 2009 SSW 45

3.5 Spectral dependence of GW-Ep variations 47

3.6 Comparison between ECMWF-T799 and ECMWF-T1279 1 48

4.1 Polar plots of orographic gravity wave amplitudes 56

4.2 Polar plots of wind rotation 57

4.3 GROGRAT ray-tracing results 59

4.4 Convective Precipitation 61

4.5 Gravity wave momentum and energy fluxes 62

4.6 Line plots of total energy flux of gravity waves 64

4.7 Polar plots of vertical gradient of F_E 66

4.8 Time-series of vertical gradient of F_E 67

4.9 Schematics of gravity wave generation 70

4.10 Polar plots of Fu at 1 hPa 72

4.11 Polar plots of Fv at 1 hPa 73

4.12 Time-series of Fu and Fv 74

4.13 Background structure at 1 hPa 76

4.14 Background structure at 10 hPa 77

4.15 Time-series of gravity wave variances 79

4.16 Evolutions of gravity wave from January 16 at 8-11 UT 80

4.17 Evolutions of gravity wave on January 16 at 13–18 UT 81

4.18 Vertical slice of gravity waves on January 16 at 14 and 18UT 83

4.19 Vertical slice of Fu and Fv on January 16 at 14, and 18 UT 84

5.1 Comparison between TIME-GCM and SABER observations 91

5.2 Schematics of gravity wave parameterization scheme 93

5.3 Profile study of gravity wave forcing 95

5.4 TIME-GCM simulation with four different gravity wave parameters 96

5.5 Residual circulations and forcings for different cases 99

5.6 Comparisons of downward progressions of SSWs 103

5.7 Comparisons of planetary wave 1 105

6.1 Longitudinal variations of weighting function 113

6.2 Comparison between the TIME-GCM base case and SABER observations 115

6.3 Zonal wind and gravity wave forcing from the TIME-GCM base case 116

6.4 Comparisons of temperatures for case 1 118

6.5 Comparisons of temperature anomalies for case 1 118

6.6 Differences between the base case and control case 1 119

6.7 Comparisons of temperature for case 2 121

6.8 Comparisons of temperature anomaly for case 2 122

6.9 Zonal wind in the base case and case 1 124

6.10 Gravity wave forcing in the base case and case 1 124

A.1 Temperature and Wind Variations during the 2009 SSW 146

A.2 Temperature and Wind Variations during the 2010 SSW 147

A.3 Planetary Wave during the 2009 SSW 148

A.4 Planetary Wave during the 2010 SSW 149

A.5 Gravity wave variations during the 2009 SSW 150

A.6 Gravity wave variations during the 2010 SSW 150

Chapter 1

Introduction

The Earth's atmosphere consists of four vertical layers: the troposphere, the stratosphere, the mesosphere, and the thermosphere, that are categorized based on the thermal structure. Traditionally, atmospheric studies tend to be confined to one of the vertical layers. Recently, the importance of global atmospheric coupling from the lower to the upper atmosphere began to gain strong attention through the advancements of observational and computational resources. However, atmospheric coupling is not well represented in weather forecast models, climate models, or space weather forecast models because of their limited model domains and the lack or poor representation of atmospheric coupling mechanisms. One of the most important elements involved in atmospheric coupling is the propagation of waves in the atmosphere. Planetary waves, tides, and gravity waves, carry momentum and energy away from their source region. Through momentum and energy transport, these waves couple the atmosphere both horizontally and vertically. Among these atmospheric waves, gravity waves are the least understood component because small-scale gravity waves with broad spectra are difficult to observe with current technologies. Owing to simplified gravity wave parameterizations in numerical models, the mechanisms of atmospheric coupling through gravity waves are not well understood. In this dissertation, the in-depth analysis of gravity wave source variations and their roles in driving atmospheric coupling will be conducted using high resolution European Centre for Medium-Range Weather Forecasting (ECMWF-T799) and the Thermosphere-Ionosphere-Mesosphere-Electrodynamic General Circulation Model (TIME-GCM).

1.1 Gravity Waves

Gravity waves result from vertical displacements of air parcels in the stable layer and have a buoyancy restoring force. Known gravity wave sources include flow over topography, convection, atmospheric instabilities, and geostrophic adjustment [Fritts and Alexander, 2003; Sato, 2000]. Gravity wave amplitudes are small in the source regions where they are generated, but they grow exponentially as they propagate upward because the atmospheric density decreases with increasing altitude. The characteristics of gravity waves are described by the dispersion relation obtained from the linear gravity wave theory [Fritts and Alexander, 2003]:

$$\omega_i = \frac{N^2k^2 + f^2\left(m^2 + 1/4H^2\right)}{k^2 + m^2 + 1/4H^2} \tag{1.1}$$

where ω_i is the intrinsic frequency, N is the Brunt-Väisäilä frequency, k is the horizontal wavenumber, m is the vertical wavenumber, H is the scale height, and f is the Coriolis parameter.

In the atmosphere, N is defined as $N = \sqrt{\frac{g}{\theta}\frac{\partial\theta}{\partial z}}$, where θ is potential temperature, g is the local gravitational acceleration, and z is geometric height. The scale height, H, is equal to $\frac{k_BT}{Mg}$ where k_B is the Boltzmann constant, T is temperature, and M is the mean molecular mass of dry air. The intrinsic frequency can also be written as:

$$\omega_i = \omega - ku_0 \tag{1.2}$$

where ω is the ground-relative frequency, and u_0 is the background flow along the gravity wave propagation direction. When gravity wave speeds and the background flow become equal, they break and deposit momentum to the mean flow.

The forcing exerted on the mean flow induced by gravity wave breaking is called gravity wave drag. The Eliassen-Palm theorem states that gravity wave drag accelerates the mean flow toward the phase velocity of waves [Eliassen and Plan, 1961]. The Eliassen-Palm theorem can be written as [Lindzen, 1990]:

$$\overline{p'w'} = \rho\,(c - u_0)\,\overline{u'w'} \tag{1.3}$$

where p', w', and u' are wave perturbations in pressure, vertical wind, and horizontal wind along the gravity wave propagation direction, respectively, c is the ground-relative horizontal phase velocity, and u_0 is the background flow along the wave propagation direction, $\overline{p'w'}$ is the vertical energy flux, $\overline{u'w'}$ is the vertical flux of horizontal momentum, and ρ is atmospheric density. The theories of the Eliassen-Palm and the critical layer explain the roles of gravity waves in determining the atmospheric wind structure. Figure 1.1 shows the climatology of mean flow from the COSPAR International Reference Atmosphere (CIRA) 1972 [Lindzen, 1981]. In general, the eastward jet stream in winter hemisphere and the westward jet stream in summer hemisphere exist between the stratosphere and the mesosphere and exhibit daily variability. Gravity wave drag weakens the jet streams in the mesosphere as explained by the schematics in Figure 1.2. In the winter hemisphere, westward gravity waves are dominant in the mesosphere because the eastward jet stream filters eastward propagating gravity waves. The westward gravity waves break in the mesosphere, which decelerates the eastward jet. The same situation occurs in the summer hemisphere where both the mean flow and gravity wave directions are reversed. These zonal wind changes induced by gravity wave breaking alter the meridional and vertical circulation due to the conservation of angular momentum. Changes in the vertical flow result in changes to the thermal structure.

In addition to gravity wave drag, temperature perturbations induced by gravity waves are important for polar stratospheric clouds (PSCs) and polar mesospheric clouds (PMCs) [Jensen and Thomas, 1994; Gerrard et al., 2004; Innis and Klekociuk, 2006; Chu et al., 2009; Alexander et al., 2011]. PSCs occur in the winter stratosphere and are required for catalytic ozone destruction that is responsible for the Antarctic ozone hole [Solomon, 1999; Tolbert and Toon, 2001]. PMCs appear in the summer mesopause region where temperature is the coldest in the Earths atmosphere. PMCs are sensitive to the changes in mesospheric water vapor and temperature [Thomas, 1991]. The increased concentration of CH_4, which oxidizes to form water vapor in the mesopause region

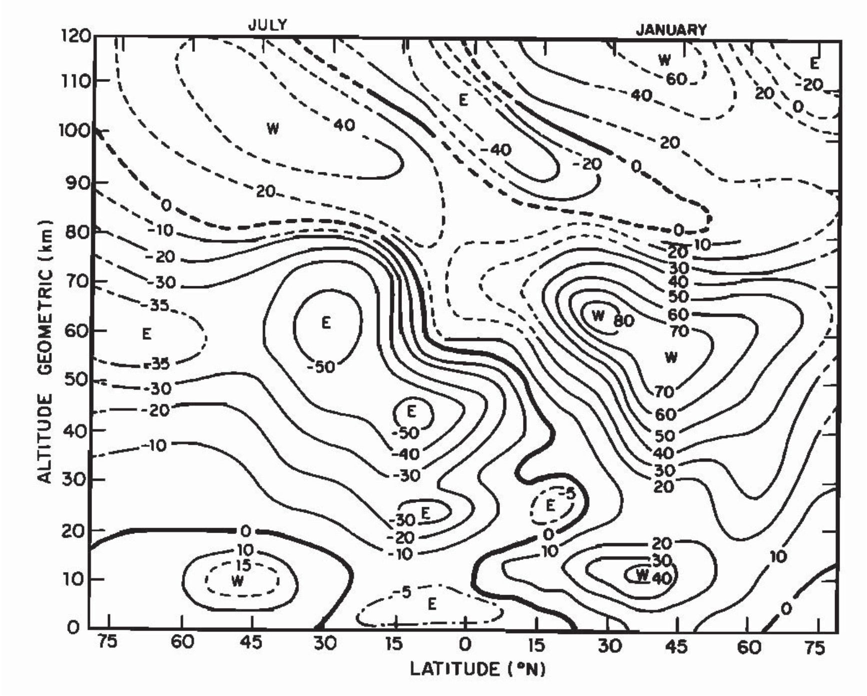

Figure 1.1: CIRA climatology of zonal mean flow. This figure is taken from Lindzen [1981]

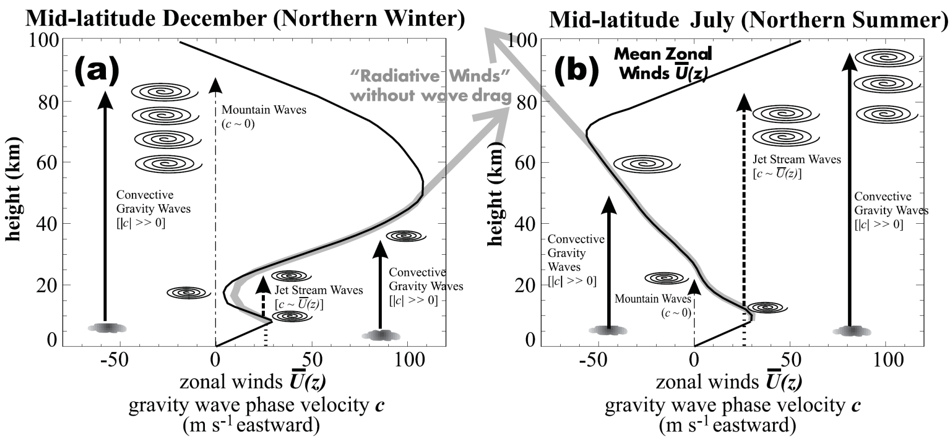

Fig. 1 Typical mid-latitude zonal winds $\overline{U}(z)$ during northern (a) winter and (b) summer. Black curve shows observed winds, grey curve shows model "radiative" winds that result without a wave drag parametrization. Sources of gravity waves with various phase speeds *c* are also depicted, with the source and wave breaking symbols similar to those defined in Fig. 10. On these plots, waves ascend vertically upwards since *c* remains constant, until they break or reach a critical level $c = \overline{U}(z_C)$. (Based on a presentation first used by Lindzen, 1981)

Figure 1.2: Schematics depicting the influence of gravity wave drag on the wind structure during summer and winter. This Figure is from Kim et al. [2003]

[Thomas et al., 1989], and CO_2 which possibly cools the middle and upper atmosphere [Portman et al., 1995], could lead to the increase of PMC brightness and occurrence frequency [Thomas, 1996]. Thus, PMCs provide a potential indicator of global climate change, which has fueled the intensive study of PMCs in recent years. Both PSCs and PMCs are very sensitive to temperature, and temperature perturbations induced by gravity waves alter cloud properties and occurrence frequency [Jensen and Thomas, 1994; Gerrard et al., 2004; Chu et al., 2009]. Therefore, gravity waves are a key element in establishing the large-scale circulation, influencing the thermal structure thus cloud occurrences and properties, and act to couple different vertical layers of the atmosphere.

Current Status and Problems in Gravity Wave Parameterization

Despite the important role of gravity waves in the atmosphere discussed above, small-scale gravity waves cannot be resolved in general circulation models (GCMs) because their wavelengths are usually smaller than (or equal to) the horizontal resolution in the model. In order to account for gravity wave effects, enormous efforts have been put into the development of gravity wave parameterization schemes with various dissipation mechanisms in GCMs [e.g., Lindzen, 1981; Holton, 1982; McFarlane, 1987; Hines, 1991; Alexander and Dunkerton, 1999; Richter et al., 2010]. One of the severe problems in gravity wave parameterization schemes is the representation of gravity wave source properties. According to McLandress and Scinocca [2005], GCM simulations are more sensitive to the gravity wave source properties than to detailed dissipation mechanisms in gravity wave parameterization schemes. Most of these classic parameterizations require to specify gravity wave source spectra and distributions. Unfortunately, most GCMs employ simplified gravity wave spectra and distributions of wave sources without much variations, leading to large uncertainties in GCMs.

The knowledge of gravity wave source properties is very limited because tracing gravity waves back to their source regions is extremely difficult using a single observational instrument or even with a high-resolution model. Recently, Richter et al. [2010] implemented in WACCM the physically based gravity wave parameterization scheme that launches gravity waves associated with the occurrences of deep convection, frontal system, and flow over topography. The new scheme and the considerations of turbulent mountain stress improve the occurrence frequency of stratospheric sudden warmings (SSWs) in WACCM.

Despite the recent progress, the in-situ wave sources related to the tropospheric jets and the stratospheric jets are not included in the gravity wave parameterization scheme developed by Richter et al. [2010]. The in-situ gravity wave sources tend to be overlooked due to the difficulty of separating in-situ generated gravity waves from waves originating in the troposphere. The in-situ gravity wave excitations by unbalanced flow related to jet structures are normally indicated by the intensity of unbalanced flow. The Lagrangian Rossby number [Koch and Dorian, 1988; Zhang et al., 2000; Zhang and Koch, 2000; Liu and Meriwether, 2004], the residual of nonlinear balance (ΔNBE) [Zhang, 2004; Wang et al., 2007], potential vorticity (PV) inversions [Zhang et al., 2000] have been used to identify the in-situ gravity wave sources related to the unbalanced flow, such as geostrophic adjustment [O'sullivan and Dunkerton, 1995], spontaneous emissions [Ford, 2000], generalized geostrophic adjustment [Zhang, 2004], spontaneous responses [Snyder et al., 2007; 2009]. However, unlike orographic gravity waves identified by well-known topographical features, the in-situ gravity wave excitations by unbalanced flow are still difficult to determine, resulting in the lack of in-situ sources in GCMs.

Although it is difficult to determine the in-situ sources, there are observational evidences indicating the importance of the in-situ gravity wave generation related to the jet structures and unbalanced flow [e.g., Uccellini and Koch, 1987; Sato et al., 1994; Yamashita et al., 2009; Plougonven et al., 2003; Guest et al., 2000; Hei et al., 2008; Yoshiki and Sato, 2000]. Uccellini and Koch [1987] observed gravity waves generated by geostrophic adjustment associated with the tropospheric jet, and these waves were always found in the exit region of the jet streak. Yoshiki and Sato [2000] showed downward propagating gravity waves in the stratosphere and the troposphere at Syowa station in Antarctica, indicating that the in-situ wave sources were above their observational heights. Yamashita et al. [2009] reported upward phase progressions of gravity waves (i.e., possibly downward propagating gravity waves) at both the South Pole and Rothera stations in Antarctica. These results also suggested that gravity waves might be generated in-situ by adjustments of unbalanced flow above their observational heights of 30-45 km [Yamashita et al., 2009]. Sato and Yoshiki [2008] found downward propagating of gravity waves that correlated well with the unbalanced flow indicator of ΔNBE. In addition to the ground-based observations, Hei et al. [2008] showed correlations between gravity wave activity and the structure of the stratospheric jet using the CHAllenging Mini-Satellite Payload (CHAMP/GPS). They argued that the in-situ gravity wave sources related to the stratospheric jet were generally more important than orographic sources in the polar regions. Idealized simulations of gravity waves generated by the adjustments of the tropospheric jets suggested that adjustments of unbalanced flows could excite gravity waves with various spectra from high frequency to inertia gravity waves [O'sullivan and Dunkerton, 1995; Zhang, 2004; Snyder et al., 2007, 2009; Wang et al., 2007, 2010].

As discussed above, observations demonstrate the existence of in-situ gravity wave sources and their importance. However, such wave sources are not considered in most gravity wave parameterization schemes. It is thus necessary to investigate the in-situ gravity wave excitation mechanisms due to the unbalanced flow and their impacts on atmospheric dynamics and coupling. The in-situ gravity wave sources related to the polar night jet can be prominent when the polar vortex is highly disturbed, such as during SSWs. Hence, this dissertation focuses on gravity waves during SSWs to study in-situ wave generations and their impacts.

1.2 Stratospheric Sudden Warming

A SSW is one of the most dynamic phenomena in the stratosphere. A SSW causes extreme disturbances in the polar winter stratosphere with sudden increases in temperature and zonal wind reversals. SSWs are categorized into the major and minor SSWs based on the magnitudes of temperature and wind anomalies. According to the World Meteorological Organization (WMO), if the temperature increases poleward from 60° and the zonal mean zonal wind reverses from the eastward to the westward at 10 hPa, then it is called a major SSW. Temperature increases without the wind reversals are defined as minor warmings.

The first SSW was observed by Scherhag [1958; 1960] using radiosondes over Berlin. Since then, the major SSWs have been observed about six times per decade in the Northern Hemisphere (NH) but only once in the Southern Hemisphere (SH) in 2002 [Charlton et al., 2007]. Minor SSWs occur more often both in the NH and SH. The causes of SSWs are widely accepted as amplifications of planetary waves and their interactions with the mean flow as they propagate upward [Matsuno, 1971]. Figure 1.3 (taken from Andrews et al. [1987]) is a schematics that shows the meridional and vertical motions induced by breaking planetary waves during a SSW. This schematic is based on the theory proposed by Matsuno [1971]. The dissipations of westward propagating planetary waves accelerate the mean flow westward, and the westward acceleration causes poleward flow due to the Coriolis force. The poleward flow further induces the downward and upward flow, resulting in the adiabatic warming in the stratosphere and the adiabatic cooling in the mesosphere. Planetary waves in the SH are usually weaker than those in the NH due to the less land-see contrast and the relatively featureless topography, explaining why SSWs occur more often in the NH than in the SH.

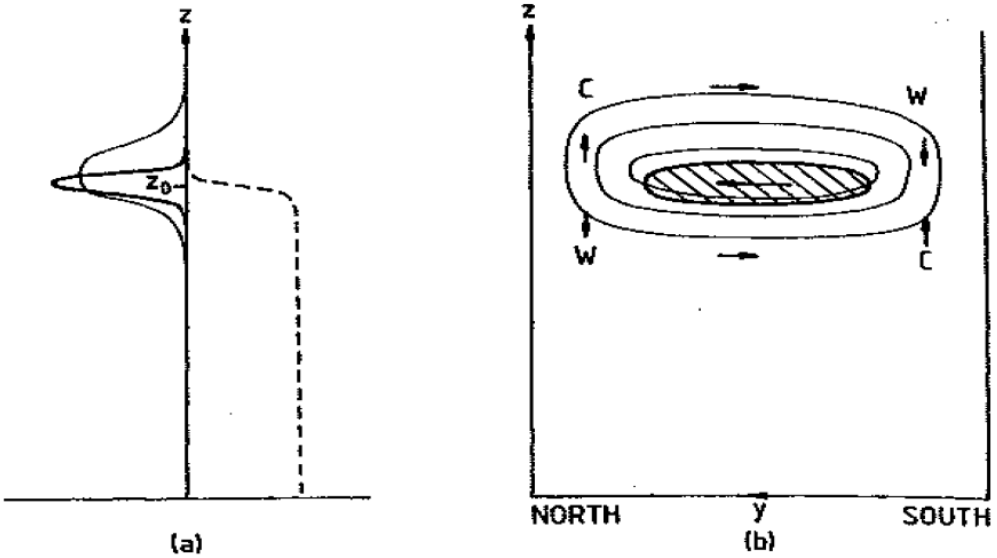

Figure 1.3: The schematics of physical mechanisms of occurrence of SSWs from Andrews et al. [1987] based on Matsuno [1971]. (left) planetary wave activity (dashed line), divergence of EP flux (heavy solid), and acceleration of mean flow (thin solid). (right) divergence of EP flux (shaded region), acceleration of mean flow (thin contour), residual circulation (arrow), warming (W), and cooling (C).

Occurrences of SSWs are also affected by the QBO and the solar cycle [e.g., Andrews et al., 1987]. During the westward phase of QBO, the winter polar region tends to be warmer and more disturbed than those during the eastward phase of QBO [Holton and Tan, 1980]. Consequently, SSWs occur more frequently during the westward phase of QBO [Labitzke, 1981; Holton and Austin, 1991]. Solar cycle influences on SSWs are also reported [Labitzke, 1987; Gray et al., 2004] whereby SSWs are more common during solar maximum.

Atmospheric Coupling Associated With Stratospheric Sudden Warmings

Although SSWs only occur in the polar winter stratosphere, SSWs have significant impacts globally from the troposphere to the thermosphere as follows: (1) there are cooling in the mesosphere and the warming in the lower thermosphere at high latitudes in the winter hemisphere [Holton, 1983; Labitzke, 1972; Liu and Roble, 2002; Siskind et al, 2005], (2) there are cooling in the mid-latitude thermosphere and E×B drift and total electron content (TEC) anomalies in the equatorial ionosphere [Goncharenko and Zhang; 2008; Chau et al., 2009; Goncharenko et al. 2010; Liu et al., 2010], (3) there are warming of summer mesopause and reductions of brightness and occurrence of PMCs at high latitudes [Karlsson et al., 2007, 2009], (4) there are cooling in the tropical stratosphere [Fritz and Soules,1970], (5) there are enhancements of tropical convection by altering the Brewer-Dobson circulation [Eguchi and Kodera, 2007], and (6) there is downward propagation of warming anomalies into the troposphere [Bladwin and Dunkerton, 2001; Sun and Robinson, 2009; Kuroda, 2008]. Figure 1.4 summarizes the global effects due to SSWs.

A key to vertical atmospheric coupling from the winter stratosphere to the winter thermosphere is gravity waves [Holton, 1983; Liu and Roble, 2002]. Figure 1.5 explains the changes in gravity wave propagation due to background wind reversals, and Figure 1.6 summarized the changes in temperatures due to gravity waves and planetary waves during SSWs. Under the typical winter condition (before SSWs), the strong eastward jet exists in the polar winter stratosphere. The eastward jet allows westward gravity waves to propagate up to the mesosphere while the eastward gravity waves are filtered. During SSWs, the eastward polar night jet is reversed to be westward

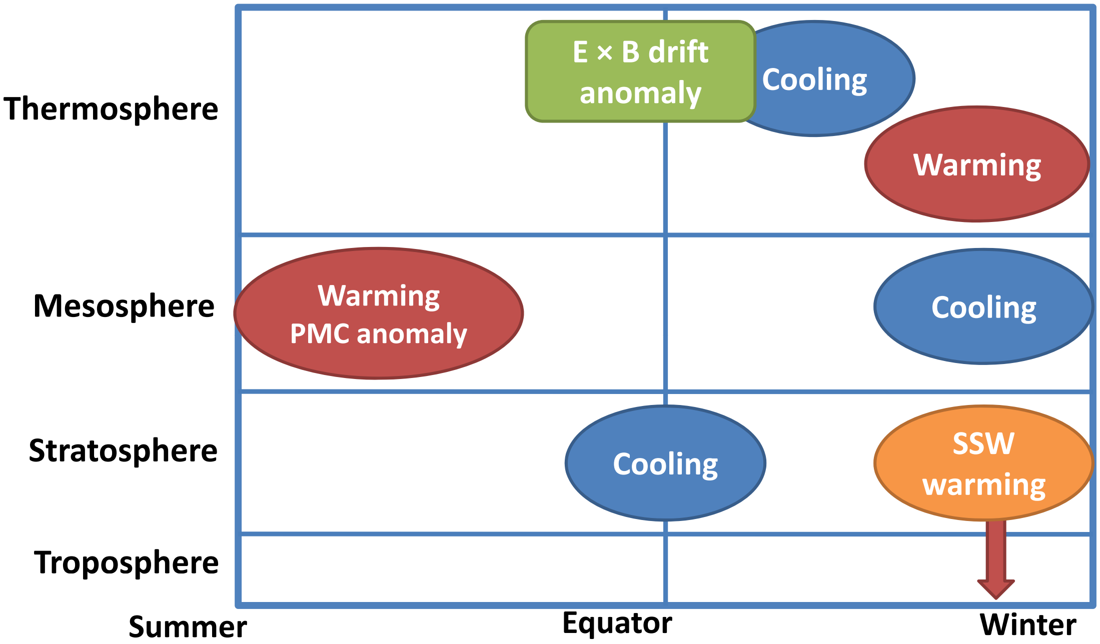

Figure 1.4: Schematics illustrating global impacts due to SSWs.

by the interactions between the mean flow and planetary waves, and then the background wind conditions become westward. Because of the zonal winds during SSWs, the eastward gravity waves, instead of the westward gravity waves, propagate to the mesosphere. The changes in filtering of gravity waves lead to changes in the direction that gravity waves accelerate the zonal flow in the MLT region. The changes in gravity wave forcings from westward to eastward at mid- to high-latitudes induce an equatorward flow in the upper mesosphere. Such flow drives upward flow in the mesosphere and downward flow in the lower thermosphere, resulting in adiabatic cooling and warming in the mesosphere and the lower thermosphere, respectively [Liu and Roble, 2002].

Other essential features to understand the mechanisms of vertical coupling during SSWs are the downward progression of temperature and wind anomalies from the mesosphere to the stratosphere [Hoffman et al., 2002, 2007; Dowdy et al., 2004; Bhattcharya et al., 2004]. Hoffman et al. [2002, 2007] showed the wind reversal in the mesosphere observed ∼6 days before the 2006 SSW. Further, for 51 SSWs between 1989 ad 2000, Hoffman et al. [2007] report that 53% of the time there are concurrent reversals in mesospheric zonal winds. Dowdy et al. [2004] also found that zonal wind reversal occurred in the mesosphere about one week earlier than that occurred in the stratosphere. The wind reversal was also observed by Michelson Interferometer at Resolute Bay (74.9°N, 94.9°W) during the peak warming period associated with cooling and warming [Bhattacharya et al., 2004]. Liu and Roble [2005] successfully simulated the downward progression of wind anomalies from the mesosphere to the stratosphere using TIME-GCM for the 2002 SSW simulation in the SH. Their simulated wind reversal started in the mesosphere and gradually progressed downward during the episode of several minor warmings, and then the wind reversal reached 10 hPa pressure level during the peak warming. The downward progression of zonal wind anomalies during SSWs are directly tied to the downward movement of the zonal mean zero-wind line [Coughlin and Tan, 2005; Liu and Roble, 2005]. The zero-wind line is a critical layer for the stationary planetary waves. The locations of mean flow and planetary wave interactions descend with the downward progression of the zero-wind line height. The height of the zero-wind line is strongly controlled by gravity wave forcings [e.g., Sassi et al., 2002], and thus gravity waves can play an important role in establishing

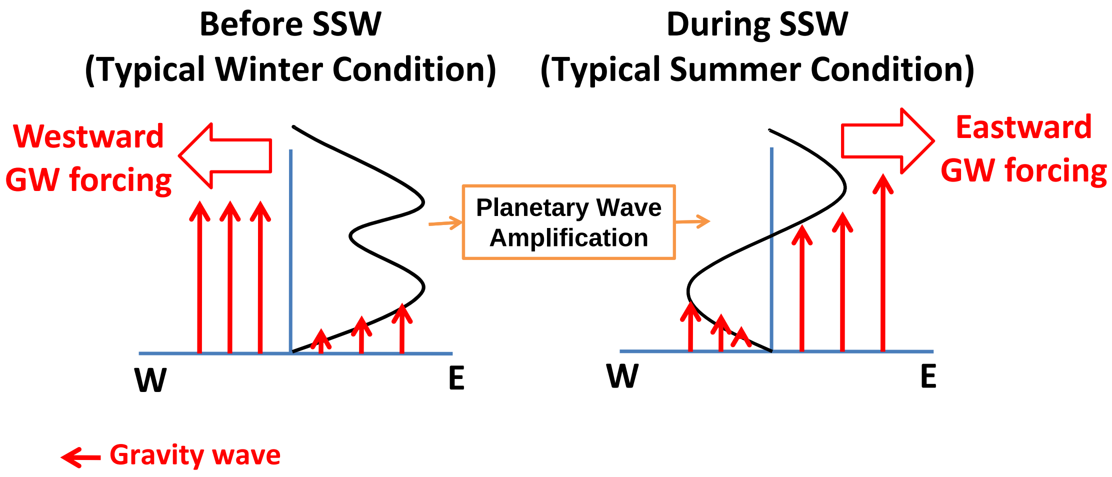

Figure 1.5: Schematics of gravity wave propagation and forcing under the typical winter conditions and SSW conditions. The x-axis and y-axis represent the horizontal axis from the west to the east and altitude, respectively. The black line is the typical zonal wind, the red thin arrows represent gravity waves, and the red block arrows show the direction of gravity wave forcings.

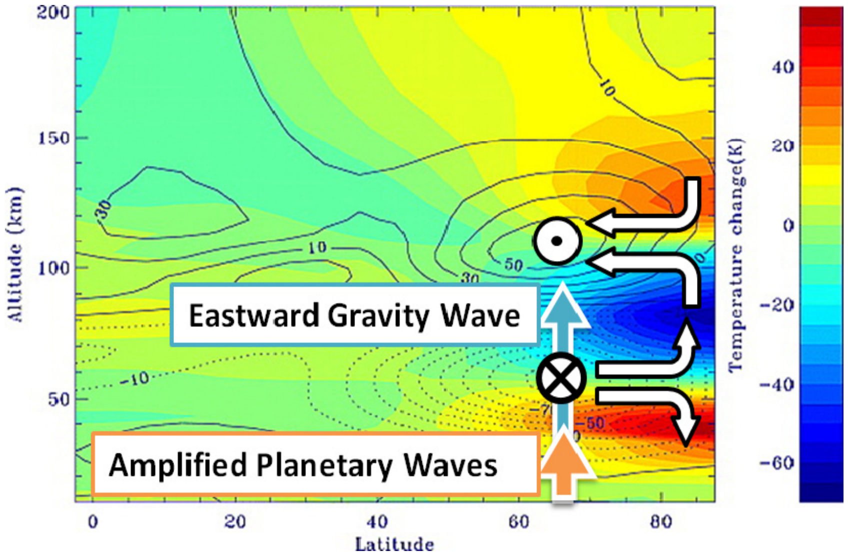

Figure 1.6: Latitude-altitude plot of zonal mean zonal wind, meridional wind, vertical wind, and temperature anomalies during a SSW from Liu and Roble [2002]. The orange arrow shows the amplified planetary waves, the blue arrow represents the vertical propagation of eastward gravity waves, and white arrows depict the induced meridional and vertical flow due to gravity waves and planetary waves.

the adequate height of the zero-wind line for planetary wave and mean flow interactions.

Problems in Atmospheric Coupling Study

While gravity waves are know to influence atmospheric coupling during SSWs [Holton, 1983; Liu and Roble, 2002], the understanding of gravity wave variations and their mechanisms during SSWs was insufficient to gain a compete picture of atmospheric coupling. Previous studies showed significant variations of gravity waves associated with SSWs [Whiteway and Carswell, 1994; Duck et al., 1998; Vankat Ratnam et al. 2004; Wang and Alexander, 2009; Thurairajah et al., 2010]. Enhancement and reduction of gravity waves have been observed to be dependent on the relative locations to the edge of polar vortex, the SSW type, and the instrument capabilities. These gravity wave variations associated with SSWs were mainly explained by the changes in gravity wave propagation due to the modulation of the background flow. Although the distorted polar vortex during SSWs can create conditions favorable for the in-situ gravity wave generations by the unbalanced flow, studies of such gravity wave source variations are still missing.

1.3 Research Objective

This dissertation aims to investigate (1) the gravity wave variation during SSWs, (2) the physical mechanisms causing such gravity wave variations along with the generation mechanisms of gravity waves, and (3) the impacts of the gravity wave variations on the upper atmosphere. The following scientific questions will be answered:

(1) **How do gravity waves vary during the 2009 SSW in the stratosphere and lower mesosphere?**

Observations of gravity wave activities during SSWs are still rare and existing observations sometimes show conflicting results. In order to obtain a comprehensive picture of gravity wave variations associate with SSWs, the high-resolution ECMWF-T799 data is used to investigate the spatial, temporal, and spectral dependence of gravity wave variablity. Acquiring a complete picture of the gravity wave variations is a necessary step to understand the physical mechanisms behind these variations.

(2) **What are the physical mechanisms causing these gravity wave variations during the 2009 SSW?**

Studies of gravity wave variations associated with SSWs have been attributed to the changes in gravity wave propagation. However, the stratospheric polar vortex is highly disturbed due to the planetary wave growth associated with SSWs. It is thus possible that the in-situ gravity wave sources related to the polar night jet enhance during SSWs in concurrence with the changes in gravity wave propagation. This dissertation examines both the changes in gravity wave propagation and sources, and their relative contributions to gravity wave variability by utilizing the high-resolution ECMWF-T799 data and the Gravity-wave Regional Or Global Ray Tracer (GROGRAT) models.

(3) **What are the impacts of gravity waves on the MLT during SSWs?**

Most GCMs employ a simplified source function in their gravity wave parameterization schemes. It limits our knowledge of the role of gravity waves in atmospheric coupling. In this study, the representation of gravity waves in the TIEM-GCM is improved by incorporating the gravity wave variations obtained from ECMWF-T799 analysis. Utilizing the improved TIME-GCM, gravity wave influences on the characteristics and downward progression of MLT temperature anomalies and the elevated stratopause are then examined.

1.4 Outline of Thesis

This dissertation consists of seven chapters. Following the introduction, Chapter 2 provides a description of the ECMWF and detailed validations of gravity waves resolved in ECMWF-T799. Gravity waves resolved in ECMWF-T799 are validated with ground-based lidar observations and satellite observations. Chapter 3 summarized the spatial, temporal, and spectral dependences of gravity wave variations during the 2009 SSW revealed by ECMWF-T799. Chapter 4 discusses the physical mechanisms causing the gravity wave variations during the 2009 SSW. Chapter 5 explores gravity wave impacts on the characteristics and downward progression of temperature and wind anomalies through sensitivity study. In Chapter 6, gravity wave variations obtained from ECMWF-T799 are implemented in TIME-GCM to study impacts of realistic gravity wave variations on MLT dynamics. Finally, this dissertation is concluded with summary and future research in Chapter 7.

Chapter 2

Validations of Gravity Waves Resolved in ECMWF-T799

The version of ECMWF-T799 with a horizontal resolution of 25 km has the capability of partially resolving meso-scale gravity waves. Utilizing the high-resolution ECMWF-T799, gravity wave variations and their physical mechanisms are investigated in this dissertation. This chapter introduces ECMWF-T799 and demonstrates the capability of ECMWF-T799 through validating gravity waves resolved in ECMWF-T799 with ground-based lidar data and satellite observations along with the high-resolution models of the the University of Oklahoma's Advanced Regional Prediction Systems (ARPS) and the Goddard Earth Observing System Model, Verison 5 (GEOS-5) assimilated data.

2.1 ECMWF

ECMWF model provides the assimilated atmospheric data. Wind, temperature, humidity, ozone, and surface pressure are provided by the four dimensional data assimilation system. ECMWF is a hydrostatic spectral model solving non-linear equations. ECMWF employs the hybrid vertical coordinate and the reduced Gaussian horizontal grid. The hybrid coordinate consists of terrain following coordinate below ∼70 hPa and constant pressure level above ∼70 hPa as shown in Figure 2.1. In the reduced Gaussian grid, the number of grid points along longitudes is reduced towards the poles.

The version of T799 from May 2008 to April 2010 is open to public for Year of Tropical Convection (YOTC) projects. The YOTC version of ECMWF-T799 has the horizontal resolution of 0.25° × 0.25° (latitude × longitude) and 91 vertical levels from surface to 0.01 hPa (~80 km). The horizontal resolution is ~25 km, and ECMWF-T799 is capable of resolving gravity waves with horizontal wavelength longer than 100–150 km. The vertical resolutions are ~0.4 km in the lower stratosphere and ~1–2 km in the stratosphere [Wu and Eckermann, 2008]. As discussed in Wu and Eckermann [2008], ECMWF-T799 has limitations of resolving gravity waves with vertical wavelength less than ~4-6 km in the stratosphere. The model time step for ECMWF-T799 is 12 minute. ECMWF-T799 uses the Rayleigh friction above 9.9 hPa and an orographic gravity wave parameterization. Recently, ECMWF replaced the Rayleigh friction by nonorographic gravity wave parameterization and upgraded their model resolution to ~15 km as T1279 version. There are two types of ECMWF data available, analysis and forecast versions. The analysis version is assimilated data combined with forecast data similar to the initial condition of forecast version. Analysis version provides the 6-hourly output (0:00, 6:00, 12:00, and 18:00 UT) with both the pressure vertical levels and the model vertical levels. The model levels are raw vertical coordinates with 91 levels. The pressure levels consist of 25 vertical levels from 1000 hPa to 1 hPa interpolated from the model levels. The differences between the vertical resolutions of the model and pressure levels are shown in Figure 2.2. For the forecast version, the model is initialized at 12 UT every day, and

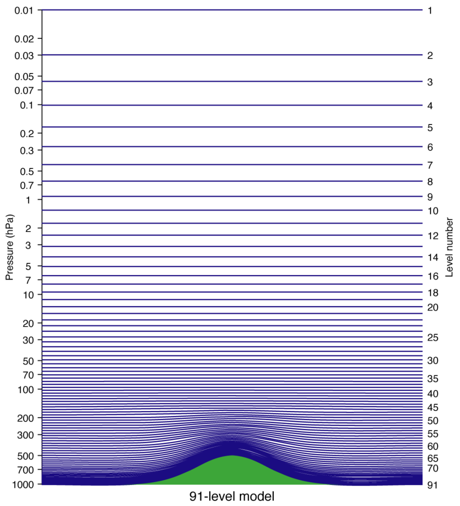

Figure 2.1: Schematics of ECMWF model level.

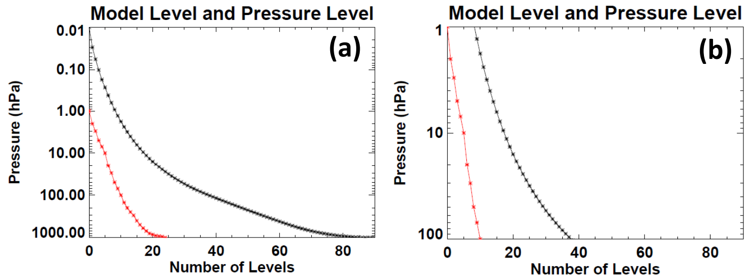

Figure 2.2: (a) The comparison between the model level and pressure level from 1000 hPa to 0.01 hPa. (b) the zoom-in version of comparison from 100 hPa to 1 hPa.

hourly forecast outputs from 12 h to 36 h are provided by ECMWF. In this study, the analysis version is mainly used for gravity wave study because the high vertical resolution in analysis version is suitable for gravity wave study (91 vertical level vs. 25 vertical level). The hourly forecast data is used for studying the flow evolution. The hourly forecast data are available from January 7 to January 25 for this study.

2.2 Background of Gravity Waves in ECMWF

Although ECMWF has been used for atmospheric sciences by providing realistic background wind and temperature, studies on their resolved gravity waves are still rare. Plougonven and Teitelbaum [2003] and Hertzog et al. [2001, 2002] used ECMWF-T511 and T319 and compared with radiosonde and super balloon observations. Plougonven and Teitelbaum [2003] concluded that the location and timing of gravity wave occurrences in ECMWF-T511 agreed with radiosonde data, though the characteristics of gravity waves in ECMWF-T511 did not match with radiosonde results. The discrepancies in wave characteristics might be caused by the model resolutions [Plougonven and Teitelbaum, 2003]. On the other hand, Alexander and Teitelbaum [2007] showed a case study of propagating mountain waves in Antarctica Peninsula by comparing the ECMWF-T511 and the Atmospheric Infrared Sounder (AIRS) observations. Gravity waves resolved in ECMWF-T511 showed a good agreement with AIRS observations in terms of vertical and horizontal wavelengths, amplitudes, and timing.

Gravity waves resolved in the newer version of ECMWF-T799 have been validated with satellite data and a high-resolution weather forecast model by the following studies. The daily and seasonal variations of gravity waves resolved in ECMWF-T799 were compared with SABER observations in the tropics, the mid-latitudes, and the polar regions [Schroeder et al., 2009]. In the polar region, ECMWF-T799 and SABER observations generally matched well, though the magnitudes of gravity waves in ECMWF were a factor of two smaller than those in SABER observations. In the tropics, gravity waves were not well represented in ECMWF-T799. Schroeder et al. [2009] speculated that the convection was not well resolved in ECMWF-T799 due to the model resolution, resulting in the discrepancies between ECMWF-T799 and SABER gravity waves. In contrast to the validations by Schroeder et al. [2009], Kim et al. [2009] concluded that ECMWF-T799 has an ability to resolve typhoon generated gravity waves in the low-latitudes. Gravity waves generated by a typhoon event in ECMWF-T799 were well compared with AIRS observations and the weather forecast and research (WRF) model simulations as shown in Figure 2.3. Their results indicated the capability of resolving convectively generated gravity waves in ECMWF-T799. Furthermore, the global distributions of gravity waves in ECMWF-T799 were validated with the Microwave Limb Sounder (MLS) observations by Wu and Eckermann [2008] as shown in Figure 2.4. ECMWF-T799 captured the hot spots of gravity waves, such as at the Antarctica Peninsula, the edge of the polar vortex, and the tropics related to the deep convection. These hot spots can also be seen from the MLS observations in Figure 2.4.

Although these previous studies encourage us to use ECMWF-T799 for gravity wave study, ECMWF-T799 in the stratosphere has not been compared with the ground-based observations that cover different portions of gravity wave spectra. In addition, the capability of resolving gravity waves under the highly dynamic condition, such as SSWs, has not been validated and examined. In this chapter, gravity waves in ECMWF-T799 are further validated with ground-based lidar observations for climatological validations and with the Constellation Observing System for Meteorology Ionosphere and Climate (COSMIC)/Formosa Satellite 3 (FORMOSAT-3)/GPS for short-term validations during the 2009 SSW. Moreover, gravity waves in ECMWF-T799 are compared with the

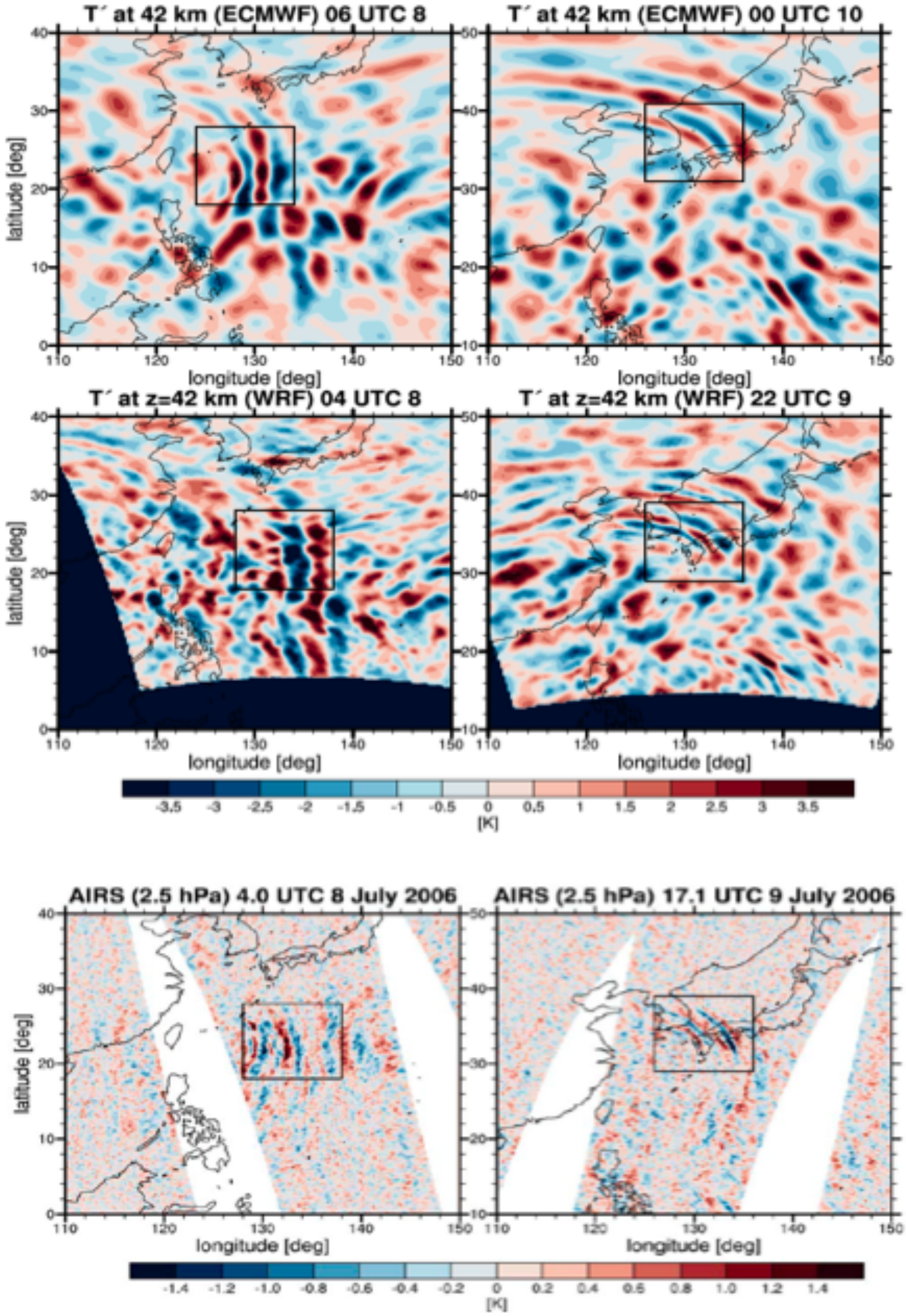

Figure 2.3: Gravity wave temperature variances obtained from (top) ECMWF-T799 data, (middle) WRF simulations, and (bottom) AIRS observations. This figure is taken from Kim et al. [2009].

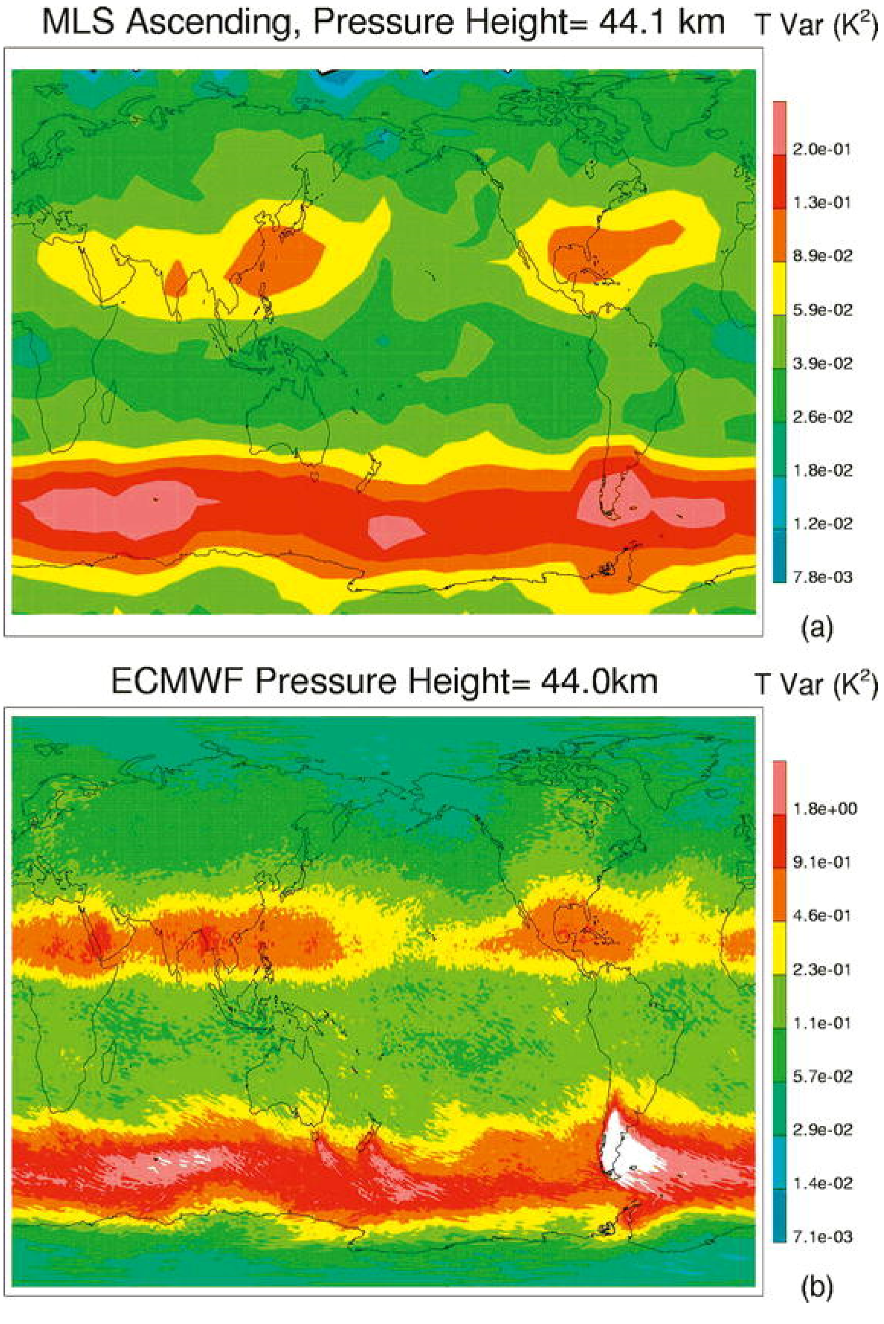

Figure 2.4: Gravity wave temperature variances at ∼44km from (top) AIRS satellite observations and (bottom) ECMWF-T799 analysis version in August 2006. This figure is taken from Wu and Eckermann [2008].

GEOS-5 and the ARPS model for the 2009 SSW, which provides us further confidence in gravity waves resolved in ECMWF-T799.

2.3 Analysis Methods

2.3.1 ECMWF Data Analysis Method

For the study in this section, the ECMWF data are interpolated onto a regular 2-km vertical grid. To remove large scale waves such as tides and planetary waves, gravity wave perturbations with zonal wavelength shorter than 2400 km and larger than 100 km (4×Δh) are extracted from temperature (T), zonal wind (U), meridional wind (V), and vertical wind (W) using wavelet analysis. Gravity waves are further decomposed into five zonal wavelength bands of 100–200 km, 200–400 km, 400–800 km, 800–1600km, and 1600–2400 km ranges. For each band, GW-Ep [$\overline{Ep} = 1/2\,(g/N)^2\,\overline{(T'/T_0)^2}$], energy flux ($\overline{p'w'}$), and the vertical fluxes of zonal momentum ($\rho\overline{u'w'}$) and meridional momentum ($\rho\overline{v'w'}$) are calculated. Here T_0 is background temperature, T', u', v', w' are perturbations of T, U, V, and W, respectively, N is the Brunt-Väisälä frequency, and g is the gravitational acceleration. The overbar indicates the spatial average over one zonal wavelength for $\overline{Ep}$, $\overline{p'w'}$, $\rho\overline{u'w'}$, and $\rho\overline{v'w'}$. The vertical fluxes of zonal momentum and meridional momentum have the following relations based on the dispersion and polarization relations under the assumption of one dominant wave in each band:

$$\left(\frac{\rho\overline{v'w'}}{\rho\overline{u'w'}}\right) = \frac{l}{k} \tag{2.1}$$

Utilizing the relations of Equation 2.1, the horizontal wavenumber, h, is derived as

$$h = \sqrt{k^2 + l^2} = \sqrt{k^2 + \left[\left(\frac{\rho\overline{v'w'}}{\rho\overline{u'w'}}\right) k\right]^2} \tag{2.2}$$

where k and l are the zonal and meridional wavenumbers, respectively. k is estimated according to each zonal wavelength band of the wavelet analysis.

2.3.2 Lidar Data Analysis

Lidar (Light Detection and Ranging) is an active remote sensing instrument. The Fe Boltzman Temperature/Rayleigh lidar developed by the University of Illinois Urbana-Champaign is a zenith-pointing lidar with dual channels operating at 372 and 374 nm [Chu et al., 2002]. Observations were first made at the South Pole (90°S) from December 1999 to October 2001. The lidar system was then relocated to Rothera (67.5°S, 68.0°W) and operated there from December 2002 to March 2005 in collaboration with the British Antarctic Survey. Locations of the South Pole and Rothera are illustrated in Figure 2.5. For gravity wave analysis, relative density perturbations were used to characterize gravity waves in Antarctica with temporal resolutions of 5 min and vertical resolutions of 192 m in the altitude range of 30–45 km.

These data were analyzed for gravity wave study by Yamashita et al. [2009]. Analysis procedure is repeated here to show the spectrum coverage of gravity waves analyzed with lidar for the comparison with ECMWF-T799 data. Gravity waves are extracted from relative density

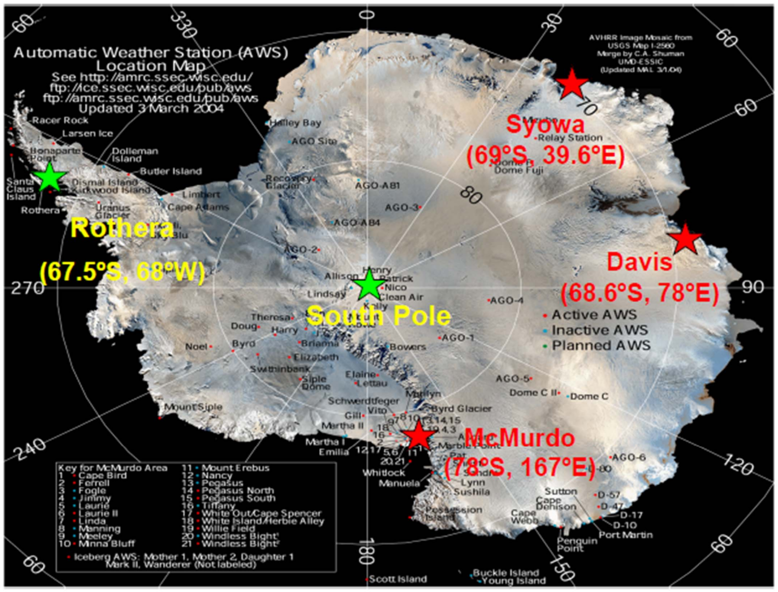

Figure 2.5: Antarctica map with major lidar stations.

profiles following Gardner et al. [1989], Senft and Gardner [1991], and Gerrard et al. [1998]. Gravity waves are obtained by subtracting the background atmospheric relative density from each 5 min density profiles. The background atmospheric density is derived for each 3-h sliding window in the following steps: (1) The perturbed relative density profiles in a 3-h window are averaged to remove short-period waves and form a 3-h averaged profile; (2) A 5th order polynomial fit is applied to this profile to simulate the unperturbed background and long-period waves with long wavelengths, and then the fit is subtracted from the 3-h averaged profile to obtain a residual; (3) The residual profile is filtered by a low-pass filter with vertical wave-number cutoff of 0.5 km-1 to reduce photon noise but retain the residual long-period waves with short wavelengths; (4) The filtered residual is then added back to the 5th order polynomial fit to form the background relative density for this 3-h window. The obtained background density is the sum of the unperturbed background density and perturbations induced by long-period waves (such as tides and planetary waves). By subtracting the 3-hourly background density from each 5-min density profile, the long-period waves are removed so the obtained relative density perturbation contains only short-period waves. To reduce photon noise, the relative density perturbations is low-pass filtered with a vertical cutoff wavelength of 2 km and a temporal cutoff period of 60 min. The mean potential energy density per unit mass (GW-Ep) is obtained through averaging over 3-h and 15-km window. GW-Ep contains gravity waves with period of ∼1–6 hours and vertical wavelength of ∼2–30 km. The further detailed analysis method and data selection criteria can be found in Yamashita et al. [2009].

2.3.3 COSMIC/GPS Data Analysis

The COSMIC/FORMOSAT-3 was launched in April 2006 [Rockenet al., 2000]. COSMIC/GPS provides global coverage of temperature profiles from near surface to ∼60 km. Due to the ionospheric contaminations, we can only use temperature data up to ∼35 km. COSMIC/GPS temperature profiles have been used for the climatology study of gravity waves [Alexander et al., 2009] and the short-term variations of gravity waves during the 2008 SSW [Wang and Alexander, 2009]. In this study, gravity waves are extracted from COSMIC/GPS temperature profiles based on a classic method introduced by Tsuda et al. [2000] and utilized by Baumgaertner and McDonald [2007]. Temperature perturbations with the vertical wavelength less than 10 km are kept as gravity waves through high-pass filtering on COSMIC/GPS temperature data [Tsuda et al., 2000].

2.4 Comparison of Analysis and Forecast Versions within ECMWF-T799

As discussed above, the analysis version of ECMWF-T799 data is mainly used for gravity wave study. One of the concerns using assimilated data for gravity wave study is whether assimilation process generates artificial meso-scale perturbation. If this specious gravity wave generation is significant due to data assimilation, the resolved gravity waves in the forecast version of ECMWF-T799 are expected to be smaller than those in the analysis version. Figure 2.6 compares the weekly mean GW-Ep obtained by the analysis and forecast versions of ECMWF-T799 from a one-year output at 10 hPa. The forecast times are at 12, 24, 48, and 240 hours after initialization. The comparison is done at Rothera because of the availabilities of observational data. The magnitudes and variations of GW-Ep are comparable between the analysis and forecast sets. Some discrepancies between analysis version and 10 days forecast version can result from the different evolutions of background flow. In addition to the seasonal variations, snapshots of gravity waves are also compared. Figure 2.7 shows the polar plots of vertical winds on January 16 in 2009 from analysis and the 12 hour forecast data. Both snapshots capture two distinct peaks of gravity wave activities around 150–200°E and 300–360°E in 60–70°N with comparable amplitudes. These comparisons suggest that the data assimilation process does not impart significant influences on gravity waves.

2.5 Validations with lidar and GPS for Seasonal Variations

Here, the seasonal variations of gravity waves resolved in ECMWF-T799 are validated with lidar and GPS satellite observations along with various previous studies to understand the capability of ECMWF resolving the general trend of gravity waves. Figure 2.8 shows the comparisons of GW-Ep between ECMWF-T799 and available lidar observations from two Antarctic stations: the South Pole and Rothera, as reported by Yamashita et al. [2009]. Here, the ECMWF-T799 data were

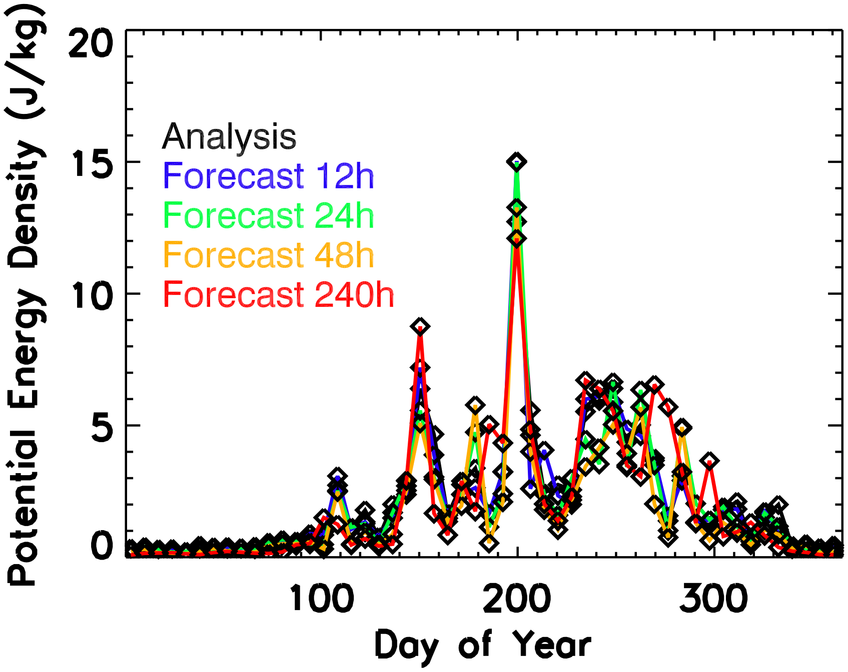

Figure 2.6: The weekly-mean total GW-Ep at Rothera at 10 hPa for analysis and forecast versions with forecast hours of 12h, 24h, 48h, and 240h.

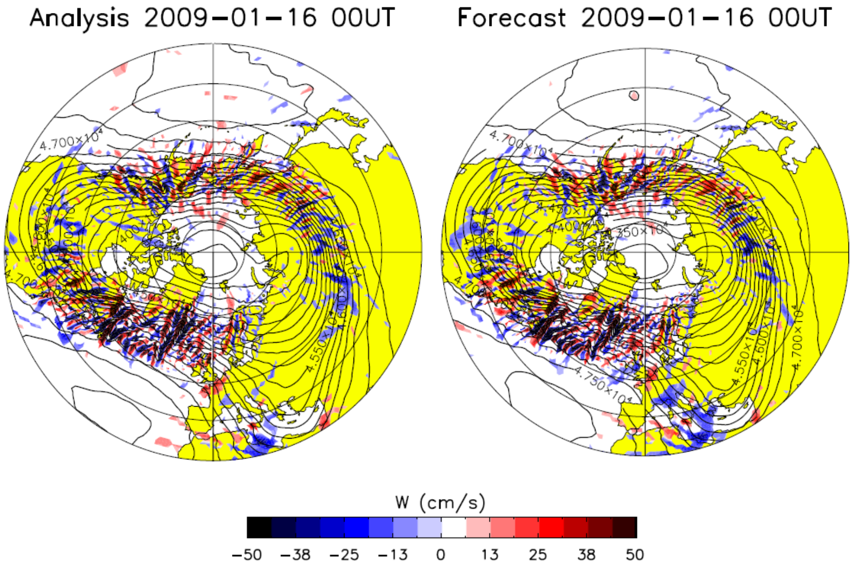

Figure 2.7: Polar plots of vertical winds (color contours) and geopotential height (line contours) on January 16 at 00 UT at 1 hPa from (left) analysis version and (right) 12 hour forecast version. Continents are filled with yellow color.

processed according to the lidar data processing approach. That is, GW-Ep is averaged over the altitude range of 30–45 km, rather than over one horizontal wavelength, to be consistent with lidar data analysis. Because of the 6-hourly ECMWF-T799 data, the mean background temperatures removed from actual temperature profiles are daily means in ECMWF-T799, instead of the 3-hour means in lidar. This difference in background estimation and limitations in model resolution may lead to spectral coverage differences. Nevertheless, ECMWF-T799 properly captures the different seasonal variations observed by the lidars at these two stations: a large seasonal variation with a maximum in winter and a minimum in summer at Rothera and quiescent GW-Ep through the year at the South Pole. Such favorable comparison further validates the ECMWF-T799 simulated gravity waves in the polar region.

Figure 2.9 displays the seasonal variations of gravity waves in ECMWF-T799. GW-Ep is averaged over the Arctic (50°N to 90°N) and the Antarctic (50°S to 90°S). Both GW-Ep in the

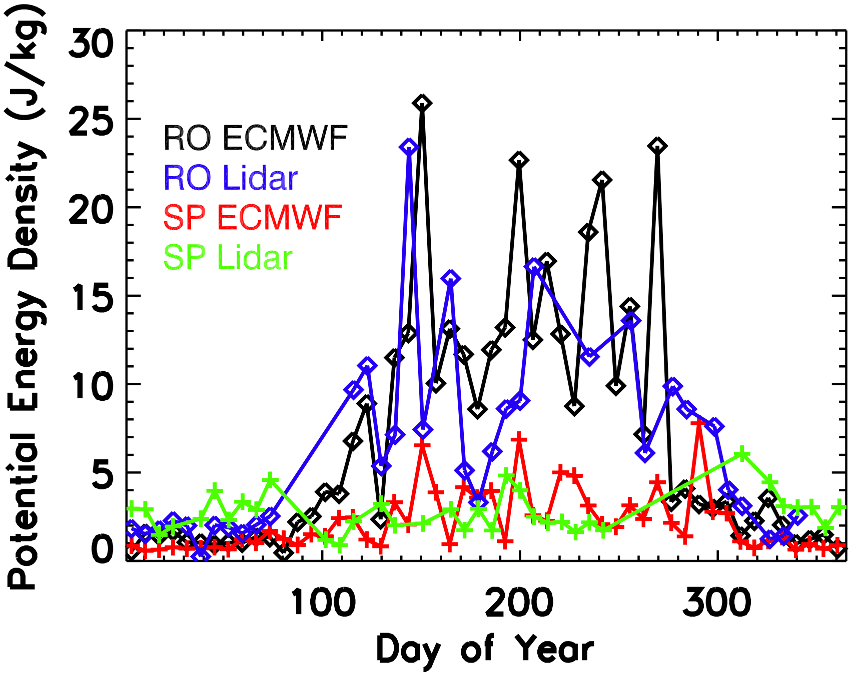

Figure 2.8: The weekly mean GW-Ep at Rothera (RO) in 2003–2005 and the South Pole (SP) in 1999–2001 obtained by lidar, compared with ECMWF-T799 in July 2008 – June 2009 between 30–45 km. Every five other days of ECMWF-T799 data are used to obtain seasonal variations.

Arctic and Antarctic show clear seasonal variations with a maximum in winter and a minimum in summer. Figures 2.9c–d show the line plots of GW-Ep averaged over the altitude range of 26–33 km to compare with CHAMP/GPS observations later. The peak GW-Ep occurs in January and December in the Arctic. On the other hand, in the Antarctic, GW-Ep peaks in August and September at the time of transition from the summer to the fall. The peak GW-Ep in the Antarctic is delayed by about two months compared to results from the Arctic in ECMWF-T799. The phase differences of seasonal variations between two hemispheres are also observed by CHAMP/GPS in Figure 2.10 [Hei et al., 2008]. Figure 2.10 shows the climatology of GW-Ep from CHAMP/GPS observations averaged over the Arctic and Antarctic. GW-Ep peaks on December and January almost every year in the Arctic, and the peaks in the Antarctic occur around August, September, and October, similar to ECMWF-T799 simulations.

The seasonal variations of GW-Ep at Rothera and the South Pole and in the Antarctica and Arctic from ECMWF-T799 are also comparable to other reported observations. The MLS measurements showed the wave variance to be maximum in winter and minimum in summer around Drake Passage (50°S to 70°S latitude and 290°E to 315°E longitude) near Antarctica Peninsula at 28 km and 43 km [Wu and Jiang, 2002]. Baumgaertner and McDonald [2007] reported GW-Ep seasonal variations in Antarctica from ground to 35 km using CHAMP/GPS occultation temperature data. They took an average of the GW-Ep over the entire Antarctic (60°S to 90°S) and showed a peak of GW-Ep in August between 30 and 35 km. This is comparable to ECMWF-T799 results at Rothera, but different from those at the South Pole. The results of Hertzog et al. [2008] showed that wave momentum fluxes in Antarctica were generally larger from September to October than during December to January, but they exhibited a decrease in momentum flux as one approaches the pole. Similarly, gravity wave observations made with a MF radar at Rothera revealed a peak wind variance in winter in the mesosphere [Hibbins et al., 2007]. Finally, lidar observations at Sondrestrom, Greenland (67°N, 310°E) exhibited wave perturbation in the altitude range of 30–45 km maximizing in winter and minimizing in summer [Gerrard et al., 2000], very similar to the ECMWF-T799 trend. Therefore, ECMWF-T799 successfully reproduces the general trend of

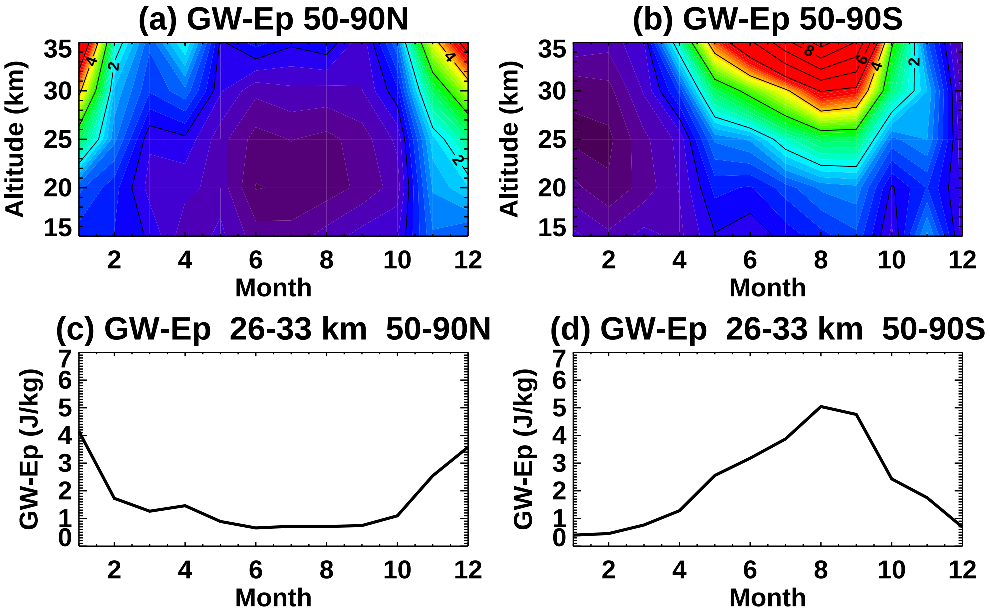

Figure 2.9: ECMWF monthly mean total GW-Ep averaged over entire (a) Arctic (50°N–90°N) and (b) Antarctica (50°S–90°S) in 2008–2009. Month mean ECMWF GW-Ep averaged over altitude range of 26–33 km and (c) Arctic and (d) Antarctica.

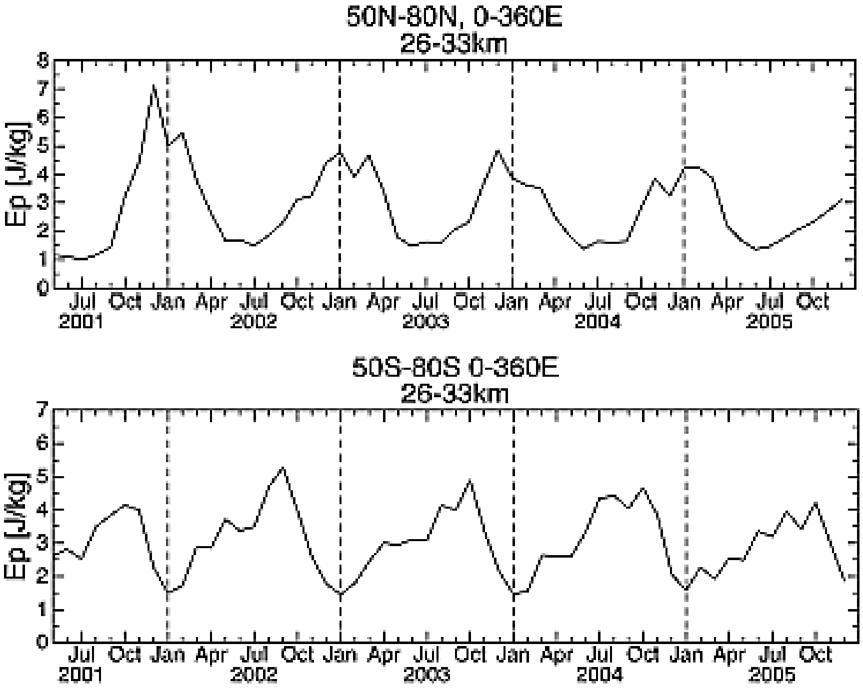

Figure 2.10: GW-Ep obtained by CHAMP/GPS averaged over (top) Arctic (50°N–80°N) and (bottom) Antarctica (50°S–80°S)and over the altitude range of 26–33 km. The plots are published by Hei et al. [2008]

gravity wave seasonal variations in the polar regions.

2.6 Short Term Variations

2.6.1 Validations with COSMIC/GPS

The daily variations of gravity waves are validated with COSMIC/GPS temperature observations focusing on the period of the SSW in 2009 in the NH. Figures 2.11a–b and 2.11c–d show the daily-zonal mean of total GW-Ep in January 2009 obtained from ECMWF-T799 and COSMIC/GPS observations, respectively. GW-Ep amplitudes from the COSMIC/GPS are largest on January 21–25, around the peak 2009 SSW period. The magnitude of GW-Ep is slightly smaller in ECMWF-T799 than in COSMIC/GPS. ECMWF-T799 shows the GW-Ep enhancement several days earlier than COSMIC/GPS. Despite these differences, the GW-Ep variations in ECMWF-T799 are generally comparable with COSMIC/GPS observations. This comparison provides an additional validation of gravity waves resolved in ECMWF-T799.

2.6.2 Validations with GEOS-5 and ARPS models

In addition to observations, gravity waves in ECMWF-T799 are further compared with assimilated data and a numerical model. GEOS-5 is developed by NASA and similar to ECMWF-T799 that employs the 4-D data assimilations system. The horizontal resolution of GEOS-5 used in this study is 0.66°, which is about two times coarser than ECMWF-T799. Figure 2.12 shows the polar plots of gravity waves obtained from ECMWF-T799 and GEOS-5 on December 20, January 5, and January 16, 2009 during the 2009 SSW period. On January 5, both ECMWF-T799 and GEOS-5 simulate gravity waves with a peak in the longitudinal range of 60°–130°E. As similar to January 5, on January 16, two peaks of gravity waves are simulated by both ECMWF-T799 and GEOS-5 in the longitudinal range of 140°–220°E and 300°–360°E. In contrast to January 5 and 16, gravity waves on December 20 show discrepancies between ECMWF-T799 and GEOS-5. GEOS-5 does not simulate gravity wave enhancements at around 0°E and 180°E as ECMWF-T799, but

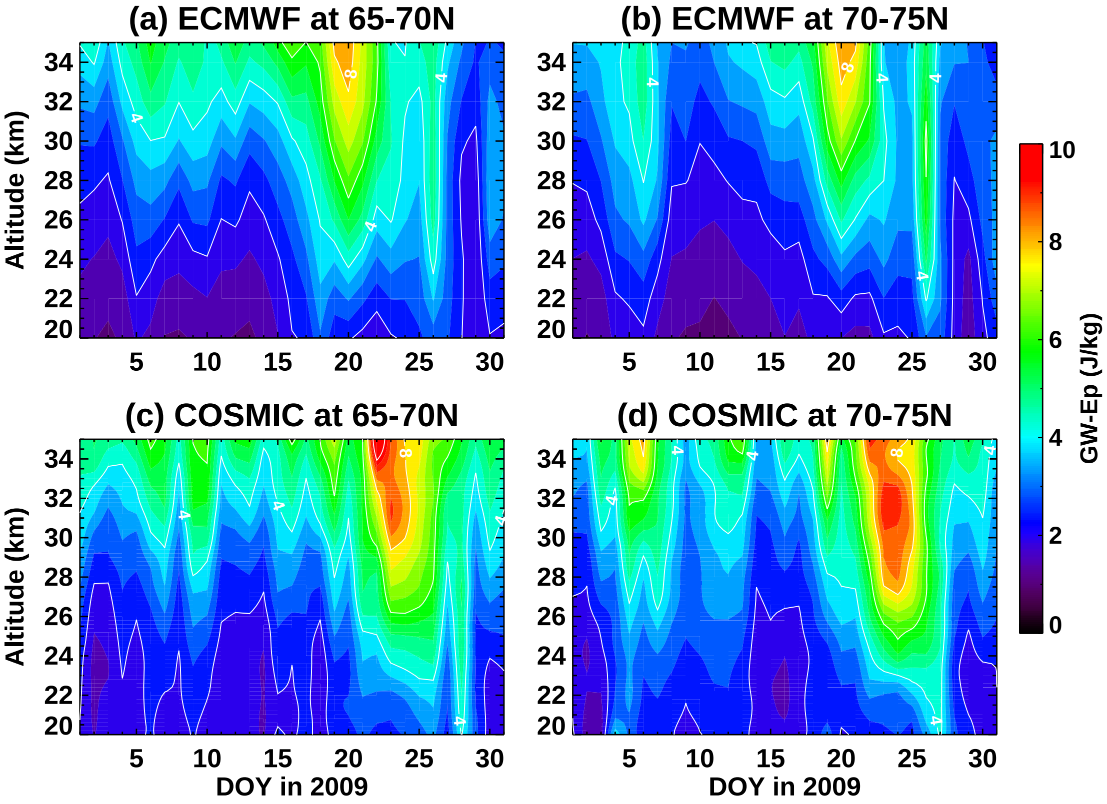

Figure 2.11: ECMWF GW-Ep averaged over latitude range of (a) 65–70°N and (b) 70–75°N. COSMIC GW-Ep averaged over latitude range of (c) 65–70°N and (d) 70–75°N.

gravity waves at the edge of polar vortex are simulated in both ECWMF and GEOS-5 on this day. Although ECMWF-T799 resolves smaller scale waves than GEOS-5 owing to the higher horizontal and vertical resolution, the locations and timing of strong gravity wave enhancements generally agree well with GEOS-5.

Finally, ECMWF-T799 is compared with the high-resolution numerical model during the 2009 SSW period. Figures 2.13 and 2.14 show the comparisons between ECMWF-T799 and the ARPS model during the 2009 SSW on January 10 and 30, 2009 at three different pressure levels, 240 hPa, 57 hPa, and 3 hPa. ARPS results are taken from Limpasuvan et al. [2011]. ARPS used the horizontal resolution of 10 km and vertical resolution of 400 m in the stratosphere. Both horizontal and vertical resolutions are higher than ECMWF-T799. Due to the limited computational resources, Limpasuvan et al. [2011] only simulated the key date during the 2009 SSW, January 10, 20, 25, and 30. The comparisons of gravity waves on January 10 and 30 show good agreements in terms of locations and timing as shown in Figure 2.13 and 2.14. For example, on January 10 at 3 hPa, the ARPS simulates three significant peaks around 0–45°E and 50–70°N, 100–120°E and 60–70°N, and 220-270°E and 50–70°N. These peaks are also simulated by ECMWF-T799 with coarse and broader wave structure. The significantly weak gravity wave activities on January 30 are simulated by both ECMWF-T799 and ARPS models. There are some differences between two simulations due to different horizontal and vertical resolutions and detailed model setup. However, the general agreements with the ARPS model that has the higher horizontal and vertical resolutions encourage us to use ECMWF-T99 model.

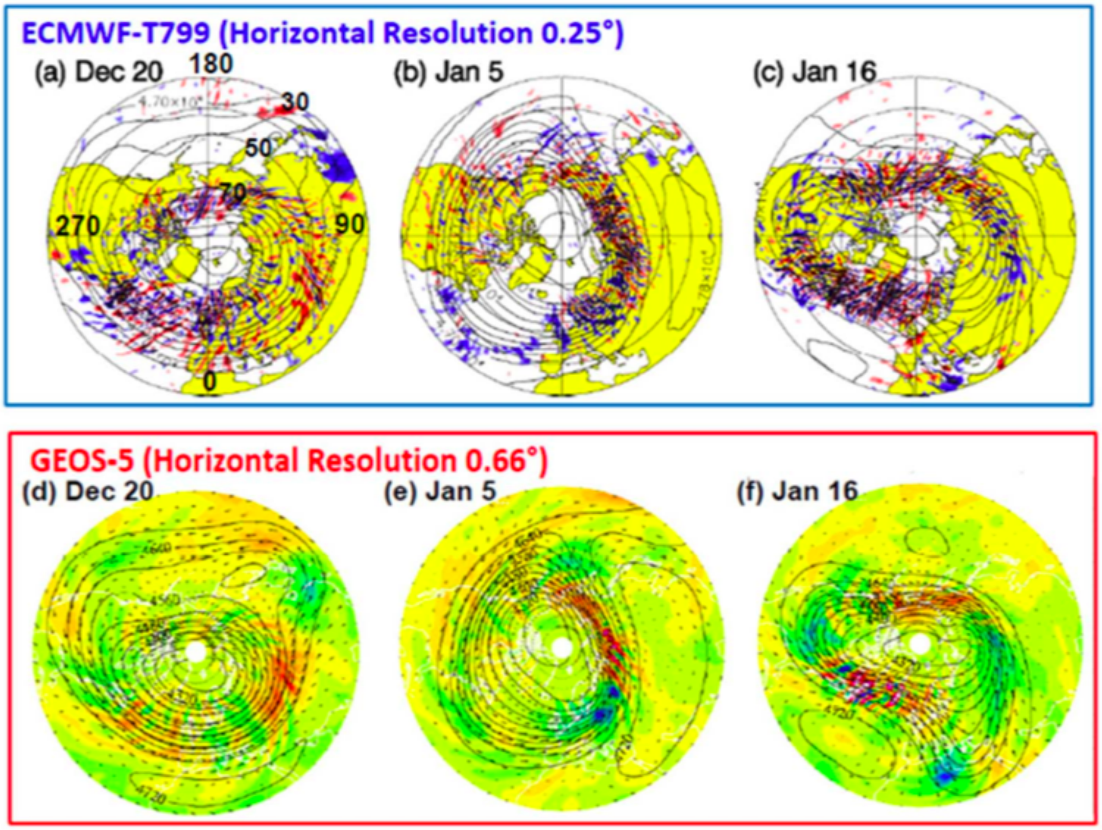

Figure 2.12: (top) polar plots of ECMWF vertical wind and geopotential height. Filled and line contours represent the vertical wind (cm/s) and geopotential height (m), respectively, at 1 hPa on (a) Dec. 20, (b) Jan. 5, and (c) Jan. 16. Geopotential height line contour interval is 400 m. Only vertical winds larger than 8 cm/s are plotted. Continents are filled with yellow color. (bottom) polar plots of GEOS-5 horizontal wind divergence and geopotential height at 1 hPa on (d) Dec 20, (e) Jan 5, and (f) Jan 16. GEOS-5 plots are provided by Dr. Varavut Limpasuvan.

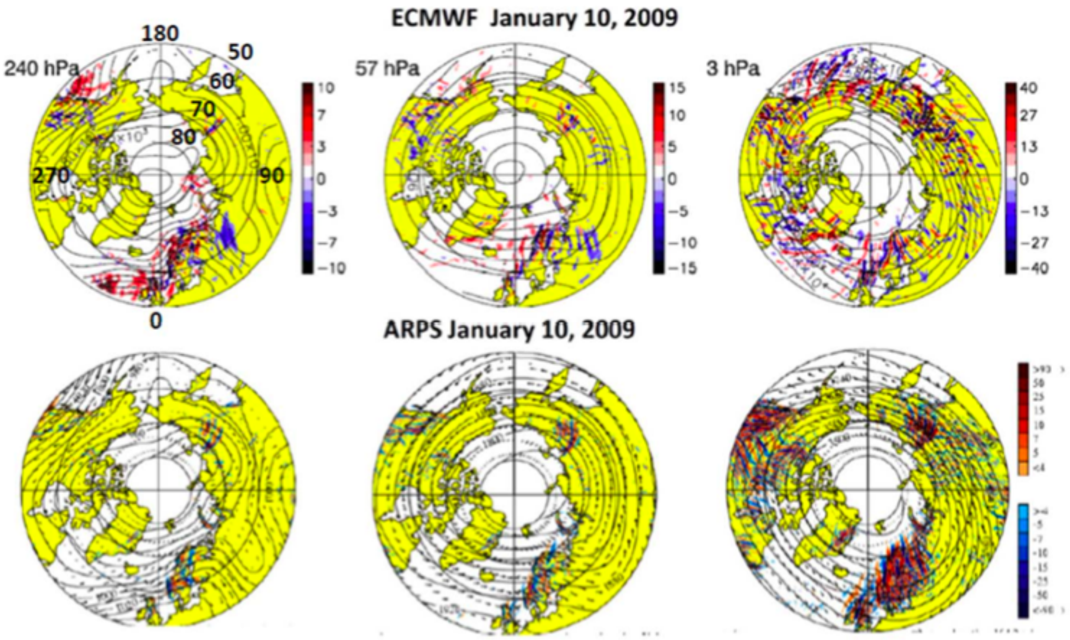

Figure 2.13: Comparisons between (top) ECMWF vertical wind (cm/s) and geopotential height and (bottom) ARPS horizontal divergence and geopotental height at (left) 240 hPa, (middle) 57 hPa, and (right) 3 hPa on January 10, 2009. Continents are filled with yellow color. ARPS plots are taken from Limpasuvan et al. [2011]. ECMWF plots are similar to plots in Figure 2.12

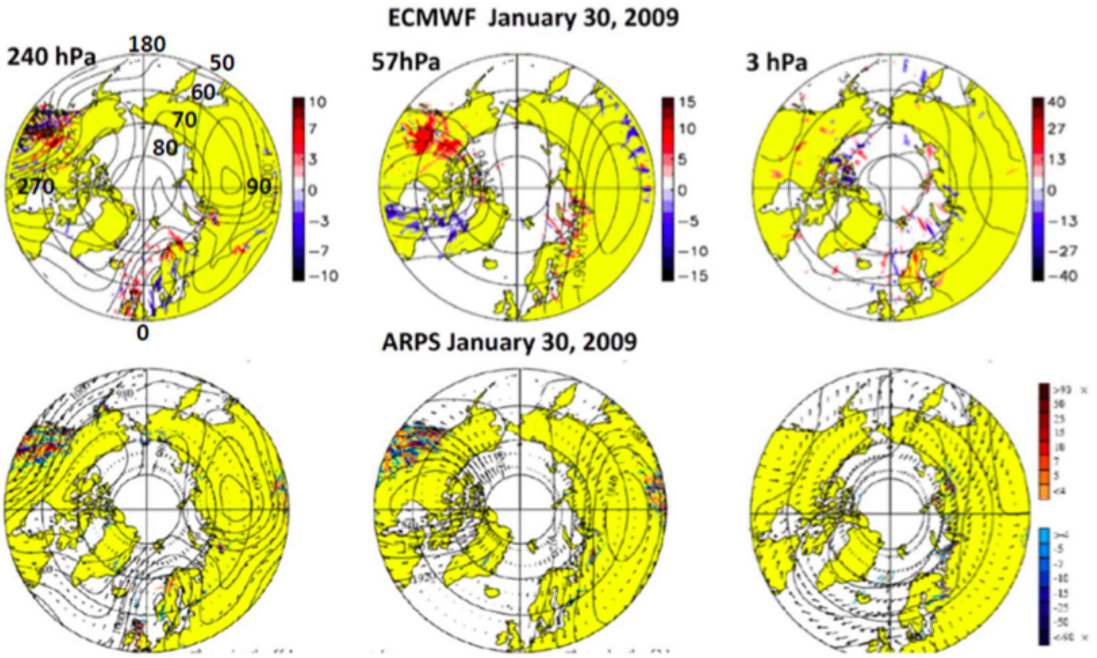

Figure 2.14: Comparisons between (top) ECMWF vertical wind (cm/s) and geopotential height and (bottom) ARPS horizontal divergence and geopotental height at (left) 240 hPa, (middle) 57 hPa, and (right) 3 hPa on January 30, 2009. Continents are filled with yellow color. ARPS plots are taken from Limpasuvan et al. [2011]. ECMWF plots are similar to plots in Figure 2.12 but at different height and date

2.7 Conclusions

ECMWF-T799 is the new version of ECMWF with the horizontal resolutions of ∼25 km. Due to the improvement of the horizontal and vertical resolutions, ECMWF-T799 has the capabilities of resolving meso-scale gravity waves with horizontal wavelengths longer than 100–150 km. The comparisons between forecast and analysis version of gravity waves show good agreements, indicating that there is no significant influence by data assimilation process on gravity waves.

ECMWF-T799 is further validated with the ground-based lidar and COSMIC/GPS observations and GEOS-5 and ARPS models. ECMWF-T799 simulates the seasonal variations of gravity waves at Rothera with a maximum in winter and a minimum in summer and at the South Pole with relatively flat variations. These two distinct seasonal variations at Rothera and the South Pole are comparable with the ground-based lidar observations. In addition to the seasonal variations of gravity waves, the daily variations of gravity waves are compared with COSMIC/GPS observations. Although the timing and magnitude of GW-Ep peak are slightly different from COSMIC/GPS observations, the general features of gravity wave variations are well simulated by ECMWF-T799 compared with COSMIC/GPS observations. The locations and timing of gravity wave activities are also validated with the GEOS-5 and the ARPS models. These validations along with the previous studies using ECMWF-T799 demonstrate the capabilities of resolving meso-scale gravity waves in ECMWF-T799. Therefore, ECMWF-T799 is further used to study gravity wave variations and their mechanisms during the 2009 SSW.

Chapter 3

Gravity Wave Variations during the 2009 SSW

Encouraged by the positive validations of gravity waves resolved in ECMWF-T799, a goal in this chapter is to investigate the temporal, spatial, and spectral dependence of gravity wave variations during the 2009 SSW using ECMWF-T799.

3.1 Introduction

As shown by Holton [1983] and Liu and Roble [2002] and discussed in Chapter 1, gravity waves have significant influences on the MLT temperature responses to SSWs. Despite the importance of gravity waves during SSWs, the limited knowledge of gravity wave variations prevents from obtaining the in-depth knowledge of gravity wave impacts on atmospheric coupling during SSWs. There are several observations of gravity waves, but results are sometime conflicting and inconclusive. Whiteway and Carswell [1994] presented gravity wave variations during the 1993 SSW in the Northern Hemisphere at Eureka (80°N, 86°W) by Rayleigh lidar in the altitude range of 25–55 km. They observed the smaller gravity wave potential energy density (GW-Ep), stronger dissipation in the stratosphere, and less wave propagation into the mesosphere during the 1993 SSW than non-warming period. On the other hand, Duck et al. [1998] showed the enhancements of GW-Ep at the same location with the same instrument as Whiteway and Carswell [1994] but during a different SSW event. Duck et al. [1998] explained this conflict by the positions of the polar vortex edge that affected the background wind above Eureka. Thurairajah et al. [2010] compared gravity wave variations from 2002 to 2005 at Chatanika, Alaska (65°N, 147°W) including the 2003

SSW and the 2004 SSW in the altitude range of 40-50 km. GW-Ep weakened during SSWs when wind reversal occurred, and GW-Ep was the largest during non-warming period in 2004–2005.

In addition to ground-based observations, CHAMP/GPS observations showed the enhancements of GW-Ep during the 2002 SSW in the Antarctic [Vankat Ratnam et al., 2004]. The GW-Ep in the altitude range of 20–30 km were averaged over entire Antarctica from 60°S to 90°S. Their results showed the GW-Ep enhancements starting from a few days before the 2002 SSW and continuing until the end of the warming. Most of GW-Ep enhancements were observed at the edge of the polar vortex and outside the polar vortex. Following Vankat Ratman et al. [2004], Wang and Alexander [2009] also showed the enhancements of gravity wave temperature variance during the 2008 SSW observed by both COSMIC/GPS and CHAMP/GPS. In contrast to Vankat Ratnam et al. [2004], Wang and Alexander [2009] did not observe the GW-Ep enhancements prior to the 2008 SSW but at the peak warming period. They showed the strong longitudinal variations of gravity wave activities, and such variations corresponded well with the strength of the background wind. Significant decrease of gravity wave momentum flux from the HIRDLS satellite after the 2006 SSW was also reported [Wright et al., 2010].

In the mesosphere, Hoffmann et al. [2007] presented the variations of gravity wave wind variances observed by MF Rader at Andenes (69°N, 16°E) in the altitude range of 70–85 km. The reductions of gravity waves are observed during the strong planetary wave activities. After planetary waves were weakened, the enhancements of gravity waves were observed in the mesosphere. Wang et al. [2006] showed gravity wave variations observed by falling sphere during the 2003 SSW in the NH. Gravity waves peaked at ∼45-50 km and at ∼60 km during the period of mesospheric cooling.

While these observations indicate the strong variability of gravity waves associated with SSWs, the comprehensive pictures of gravity wave variations are still missing. One way to better understand the gravity wave variation is to conduct detailed analysis of high-resolution model outputs, which can at least partially resolve gravity waves [e.g., Sato et al., 1999; Watanabe et al., 2008]. Our goal in this chapter is to investigate the temporal, spatial, and spectral dependence of gravity wave variations during the 2009 SSW using ECMWF-T799 data. Analysis methods used here are summarized in Chapter 2.

3.2 The 2009 Stratospheric Sudden Warming

A major SSW was observed in the Arctic in January 2009 [Manney et al., 2009]. The zonal mean zonal wind, temperature, temperature changes (anomalies) simulated by ECMWF-T799 starting January 1 are shown in Figure 3.1. The temperature increases by over ∼60 K at 80°N and the zonal wind reversal occurs at 10 hPa (∼30 km) on January 23–24 (the peak warming). At 1 hPa (∼45 km), the zonal wind reversal occurs on January 20–21, several days before the peak warming at 10 hPa. Figure 3.2 compares the temperature and temperature changes (changes from January 10) between ECMWF-T799 and SABER observations. ECMWF-T799 does not use SABER temperature for the assimilation process. Although there are less observations above ∼30 km, ECMWF-T799 captures the reasonable temperature changes compared to SABER. The downward progression of warm temperature anomalies from ∼50 km to ∼30 km is simulated by ECMWF-T799 with comparable amplitudes with SABER warm temperature anomalies in Figure 3.2a–b. The mesospheric cooling and stratospheric warming are both well simulated in ECMWF-T799 compared with SABER; however, the mesospheric cooling in ECMWF-T799 above 55 km is weaker than that in SABER. This is likely due to the lack of downward flow induced by gravity wave breaking in the mesosphere because the upper boundary of ECMWF-T799 locates at the middle of the mesosphere. In general, ECMWF-T799 shows good agreements with SABER observations.

3.3 Gravity Wave Variations during the 2009 SSW

Figure 3.3 shows the polar plots of vertical wind (filled contours) and geopotential height (line contours) at 1 hPa in the Northern Hemisphere. The vertical wind is used as a proxy for gravity wave perturbations. The wave-1 geopotential height perturbation (PW1) occurs on January 5 when the significant, localized enhancements of gravity waves are seen between 45°–135°E, where the background wind is the strongest. The wave-2 geopotential height perturbation (PW2) starts to

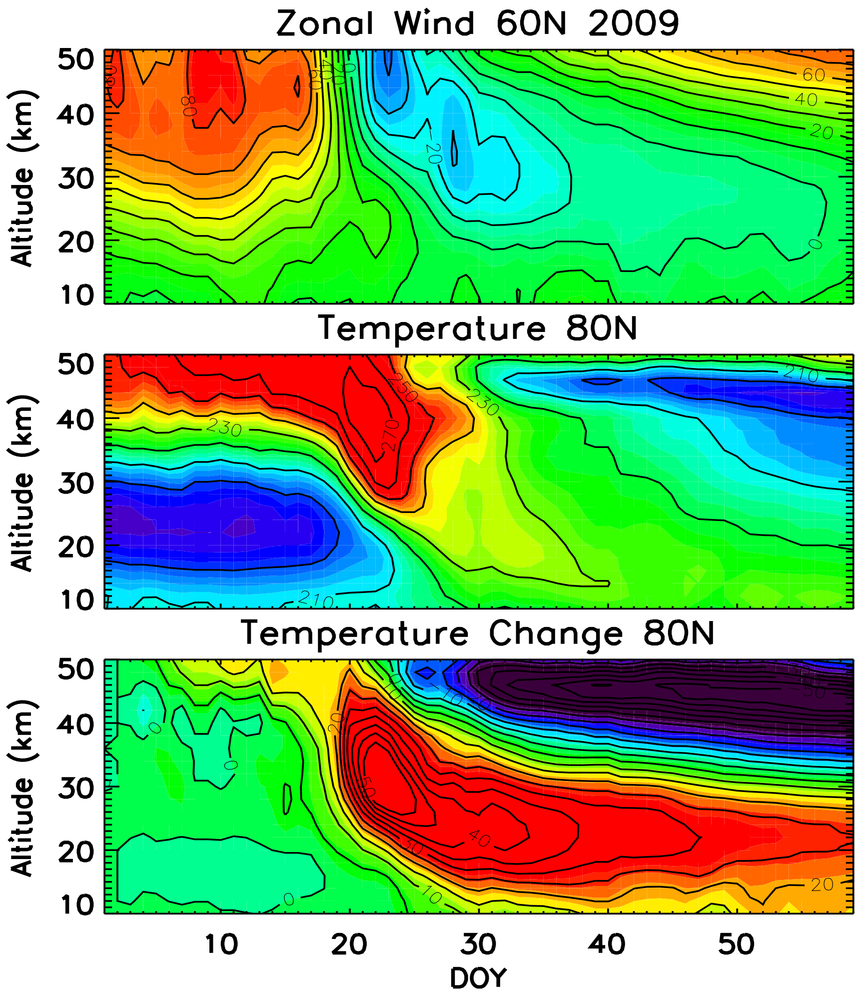

Figure 3.1: ECMWF-T799 simulations of the 2009 SSW. (a) Zonal mean zonal wind at 60°N, (b) zonal mean temperature at 80°N, and (c) zonal mean temperature changes from January 1 at 80°N obtained by ECMWF-T799.

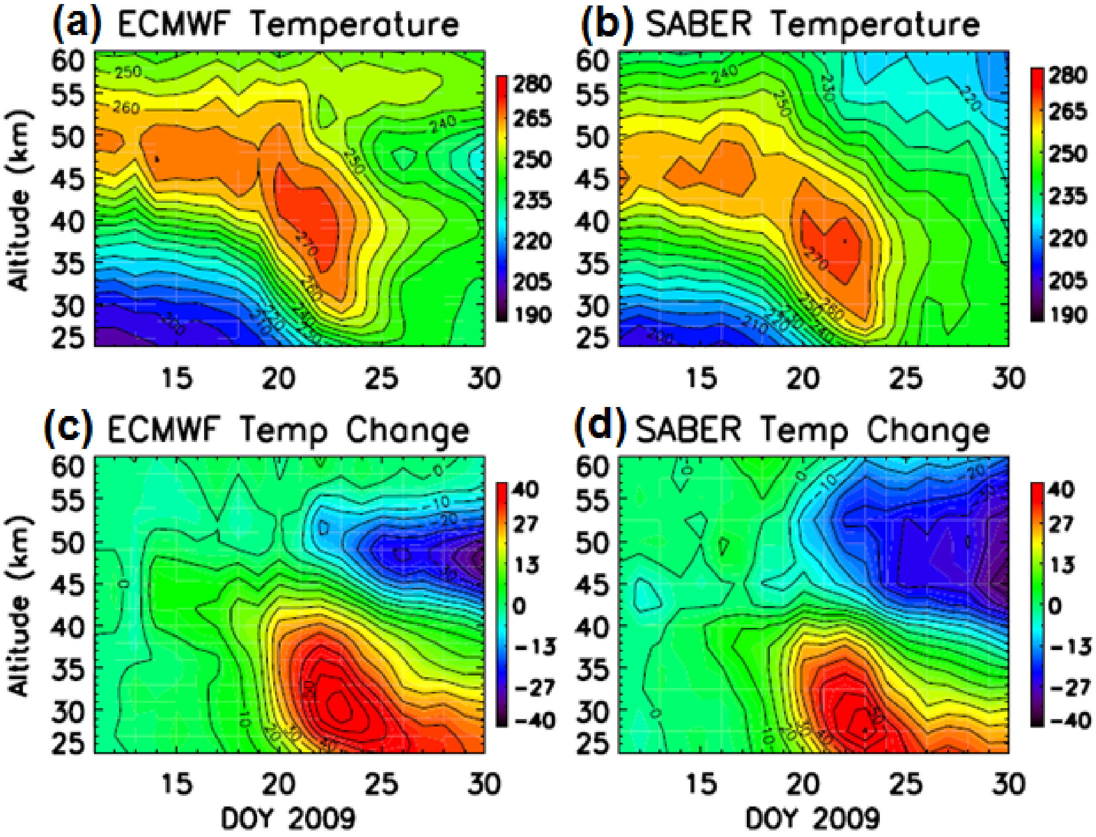

Figure 3.2: Zonal mean temperature averaged over 70–80°N from (a) ECMWF-T799 and (b) SABER. Zonal mean temperature changes (changes from January 10) averaged over 70–80°N from (c) ECMWF-T799 and (d) SABER.

grow on January 16, and the gravity wave enhancements appear in two distinct locations 180°–225°E and 300°–360°E and correspond to the PW2 signature. By January 21, the polar vortex breaks down and gravity waves generally become weaker compared to Figures 3.3a–c. As the polar vortex gradually recovers in February, gravity wave presence nearly disappears and becomes significantly weaker than those on December 20 (before the SSW). ECMWF-T799 results show that the episodes of gravity wave enhancements on January 5 and January 16 correspond to regions of the strong background wind at the polar vortex edge which undergoes strong planetary wave perturbations. As such, Figure 3.3 suggests that lidar observations would detect gravity wave enhancement or reduction during SSW, depending on the location of the lidar site relative to the locations of strong background wind at the polar vortex edge. This may explain the discrepancy of gravity waves reported previously by ground-based observations: the reductions [Whiteway and Carswell, 1994] and the enhancements [Duck et al., 1998] of gravity waves observed at the same location but in different years. Furthermore, as shown in Figures 3.4a–3.4d, the overall zonal-mean GW-Ep is enhanced during the SSW onset, consistent with satellite observations reported by Vankat Ratnam et al. [2004].

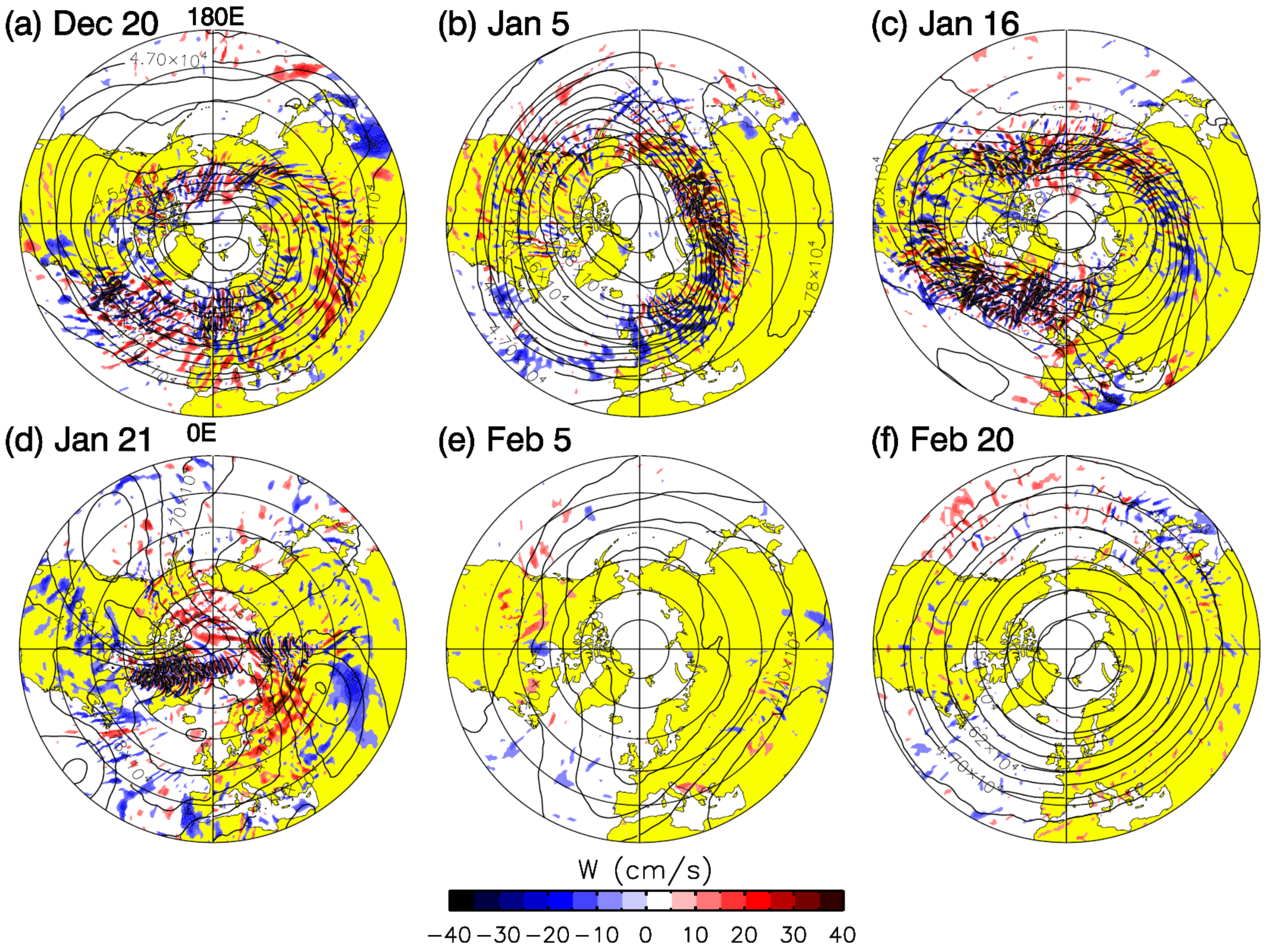

Figure 3.3: Filled and line contours represent the vertical wind (cm/s) and geopotential height (m), respectively, at 1 hPa on (a) Dec. 20, (b) Jan. 5, (c) Jan. 16, (d) Jan. 21, (e) Feb. 5, and (f) Feb. 20. Geopotential height line contour interval is 400 m. Only vertical winds larger than 8 cm/s are plotted. Continents are filled with yellow color.

To illustrate the altitude dependence of gravity waves, Figures 3.4a and 3.4b show the variations of daily-zonal mean GW-Ep in ECMWF-T799 between 20–60 km at 65°–70°N and 70°–75°N, respectively. The zero zonal-mean zonal wind line is overlaid on Figures 3.4a and 3.4b to indicate the wind reversal from eastward (on the left) to westward (on the right) and then recovery to eastward (at the far right). At 65°–70°N, GW-Ep peaks on both January 5–7 and January 15–22. At 70°–75°N, GW-Ep in Figure 3.4b shows one peak only on January 15–22. In both latitude regions, the enhancement on January 15–22 first appears in the lower mesosphere on January 15 and then progresses down to the stratosphere. This downward progression seems to follow the wind reversal, and the GW-Ep enhancements occur well before the wind reversal at all altitudes. No significant gravity waves are observed after the wind reversal, which is consistent with HIRDLE observation [Wright et al., 2010].

Overall gravity wave enhancements appear to correspond to planetary wave growth in Figure 3.3. In order to further examine the correspondence between gravity wave enhancement and planetary wave growth, Figures 3.4c and 3.4d show PW1 and PW2 amplitudes at 65°–70°N, respectively. Prior to the peak SSW, PW1 reaches a maximum around January 5, and GW-Ep increases at the same time. PW2 maximum occurs around January 20 shortly before the breakdown of the polar vortex and the wind reversal. The January 15-22 enhancement of GW-Ep corresponds to this episode of PW2. The planetary wave disturbances in ECMWF-T799 are most significant in the lower mesosphere in the early stage of the 2009 SSW, and then progress to lower altitudes from January 5 to January 22, which is consistent with the study by Liu and Roble [2005]. The height differences of the maximum GW-Ep between January 5 and 20 seem to indicate the downward progression of gravity wave enhancements corresponding to the downward progression of planetary waves.

In contrast to GW-Ep at 65°–70°N, GW-Ep at 70°–75°N does not show a clear peak on January 5. This is likely because PW1 growth on January 5 is not strong enough and 70°–75°N still lies within the polar vortex (where the wind is weak), resulting in the insignificant changes in GW-Ep at higher latitudes. On the other hand, PW2 growth displaces the polar vortex edge

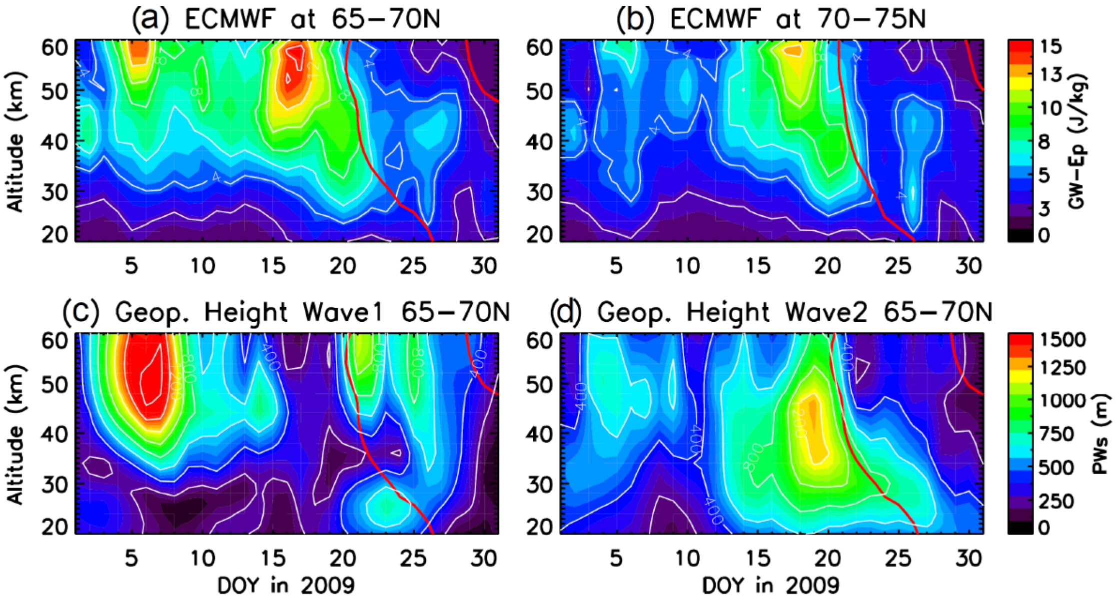

Figure 3.4: The daily-zonal mean total GW-Ep obtained by ECMWF-T799 at (a) 65°–70°N and (b) 70°–75°N between 20–60 km. The red lines are the zero zonal mean zonal wind line. The daily mean geopotential height amplitudes of (c) PW1 and (d) PW2 are plotted.

towards the pole and breaks the vortex on January 15-22. These results indicate the time lag of the GW-Ep enhancement between different latitudes depending on the movement of the polar vortex edge, which can also be seen in the polar plots of gravity waves in Figure 3.3. It should be pointed out that the application of Rayleigh friction above 9.9 hPa in ECMWF-T799 may cause some damping of gravity waves and weaken gravity waves. Nevertheless, the relative changes of gravity waves during the 2009 SSW are still meaningful.

To investigate the spectral dependence of gravity wave responses to the 2009 SSW, GW-Ep is separated into the horizontal wavelength bands of 100–400 km, 400–800 km, and 800–1600 km, as shown in Figure 3.5. Two peaks on January 5 and January 15–22 exist in both 100–400 km and 400–800 km bands, and the magnitudes of GW-Ep in the 400–800 km band are two times larger than those in the 100–400 km band. GW-Ep in 800–1600 km shows a significant peak on January 16–18 but not on January 5. Two peaks on January 5 (the large PW1 event) and 15–22 (the large PW2 event) are dominated by 100–800 km band and 400–1600 km band, respectively. The dominant horizontal wavelength is between 400-800 km that are consistent with the COSMIC/GPS observations showing dominant horizontal wavelength of 400 km for the 2008 SSW [Wang and Alexander, 2009]. These results indicate the spectral dependence of GW-Ep enhancements and that gravity waves may respond differently to the different planetary wave activities.

According to Plougonven and Teitelbaum [2003], gravity waves resolved by ECMWF-T511 have different characteristics than these obtained from radiosonde observations at the same location and time. Although both horizontal and vertical resolutions have been improved from T511 (0.5° and 61 vertical level) to T799 (0.25° and 91 vertical level), ECMWF-T799 could still have bias in resolving wave characteristics. In order to examine the impacts of horizontal resolutions of ECMWF gravity wave simulation, gravity waves simulated by ECMWF-T799 and ECMWF-T1279 are compared. ECMWF-T1279 has a horizontal resolution of 0.15° (∼15 km) with the same vertical resolutions as ECMWF-T799. There are also some upgrades of model setup, and the main change for gravity waves is the change in the sub-grid gravity wave parameterization scheme. The Rayleigh friction used in T799 is replaced by a non-orographic gravity wave parameterization scheme for T1279 while the same orographic gravity wave parameterization scheme is used for both T1279 and T799.

Figures 3.6a–b show the comparisons between T799 and T1279 version of ECMWF on January 15, 2009. Two distinct regions of strong gravity wave activities in longitudinal sectors of 300–360°E and 180–250°E are captured by both versions. As expected, T1279 version resolves finer wave structures than T799 version. However, the general features of wave enhancements and structures are comparable between T799 and T1279. Figures 3.6c–d show the spectra of vertical winds shown in Figure 3.6a–b obtained by 2D FFT. It is clear that the distributions of vertical wind spectrum are comparable between two versions with a peak around ∼400 km horizontal wavelength, though magnitudes of power spectral density is larger in T1279 than in T799 in particular for the smaller scale gravity waves. These comparisons indicate that timing, locations, altitudes, and spectra are not heavily limited by the horizontal resolution of ECMWF model. However, it can still be biased by the vertical resolution.

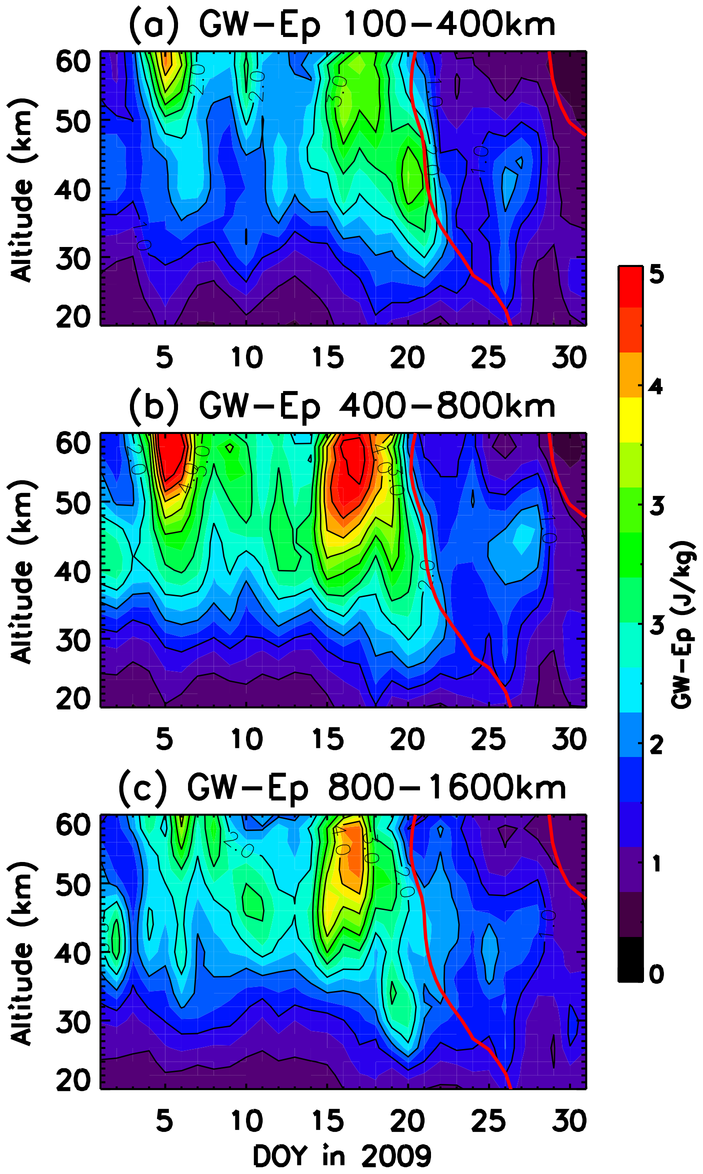

Figure 3.5: The daily-zonal mean ECMWF GW-Ep at 65°–70°N in horizontal wavelength ranges of (a) 100–400 km, (b) 400–800 km, and (c) 800–1600 km. Red lines are the zero zonal mean zonal wind line.

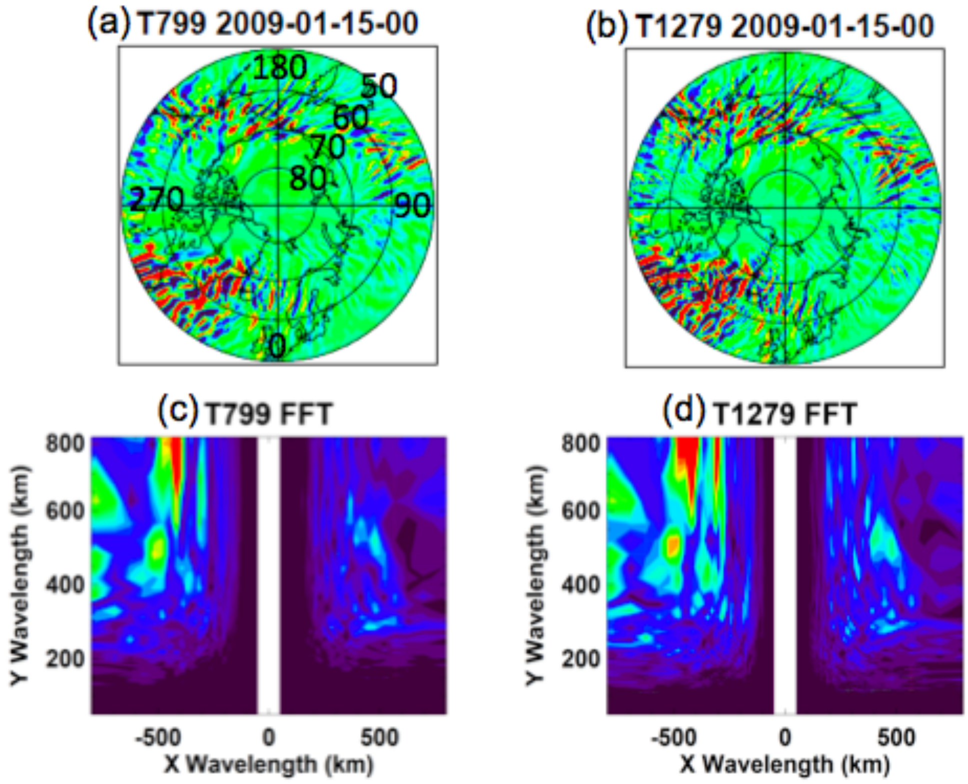

Figure 3.6: Vertical Wind at 1 hPa from (a) T799 and (b) T1279 and spectrum of vertical winds from (c) T799 and (d) T1279.

3.4 Conclusions

The ECMWF-T799 data are used to characterize gravity wave variations during the 2009 SSW. The ECMWF-T799 analysis shows that most gravity waves occur at the edge of the polar vortex, and the magnitude and occurrence of gravity waves correlate with the location and strength of the polar vortex that is strongly distorted by planetary wave growth. During the development and the onset of the SSW, the daily-zonal mean GW-Ep first increases on January 5 in coincidence with PW1 growth. Then, GW-Ep enhances again on January 15–22 as the PW2 magnifies. As the significant planetary wave disturbances (initially at the lower mesosphere) migrate down to the stratosphere, strong gravity waves (also initially enhanced at higher altitudes on January 5) gradually progress downward to the stratosphere around January 22. The downward progression of GW-Ep and planetary wave enhancement on January 15-22 seems to follow the zero-wind line. The two gravity wave peaks on January 5 and 15–22 are dominated by 100–800 km band and 400–1600 km band, respectively, indicating the spectral dependence of gravity wave enhancements. All of gravity wave enhancements occur before the wind reversal, and gravity waves become significantly weak after the 2009 SSW. The overall GW-Ep variations in ECMWF are confirmed by COSMIC/GPS observations in Chapter 2. The combination of ECMWF-T799 and COSMIC/GPS reveals the dependence of gravity wave variations on location, altitude, time, and spectrum associated with SSWs.

As pointed out by Dunkerton [1984], gravity waves show preferential propagation in regions with strong wind, and it may partially explain the ECMWF GW-Ep variations associated with SSWs. In addition, the dominant horizontal wavelength of 400–800 km from ECMWF-T799 is consistent with the sub-synoptic scales of gravity waves generated from flow adjustment (∼600 km) [O'Sullivan and Dunkerton, 1995]. Mesoscale GWs are usually associated with topography, but can also be generated by flow adjustment [Zhang, 2004]. The spectral dependence may reflect the gravity wave source influences on GW-Ep variations.

Chapter 4

Physical Mechanisms of Gravity Wave Variations during the 2009 SSW

Gravity wave variations during the 2009 SSW exhibit two peaks of GW-Ep prior to the wind reversal and a minimum after the wind reversal. The gravity wave enhancements correspond to the growths of planetary wave 1 and 2 and occur at the edge of the polar vortex. In this chapter, the physical mechanisms causing these gravity wave variations are investigated, focusing on the in-situ gravity wave excitations by the polar night jet.

4.1 Introduction

Gravity waves are a key element in defining the large-scale circulation in the stratosphere, the mesosphere, and the thermosphere through momentum and energy deposition. Although such gravity wave effects are implemented in most GCMs using gravity wave parameterizations, temporal and spatial variations of gravity wave sources and the source spectrum are poorly represented in these parameterization schemes. This fact has been identified as the leading sources of model uncertainties [McLandress and Scinocca, 2005]. In particular, the knowledge of the in-situ gravity wave excitations by the unbalanced flow related to the jet structures is limited because it is difficult to separate the in-situ generated gravity waves from gravity waves originating in the troposphere. However, both observations and simulations in both troposphere and the stratosphere have shown the importance of the in-situ gravity wave sources related to the jet stream [O'sullivan and Dunkerton, 1995; Uccellini and Koch, 1987; Plougonven and Snyder, 2005]. Uccellini and Koch [1987] summarized observational results of gravity waves generated by geostrophic adjustment associated with the tropospheric jet. Their observed gravity waves were found in the exit region of the jet streak with the horizontal wavelength of 50–500 km and wave periods of 1–4 hours. Following their research, O'sullivan and Dunkerton [1995] simulated gravity waves generated by geostrophic adjustments with a 3D nonlinear numerical model with the model resolution of 50 km. As the tropospheric jet stream is distorted, the inertia gravity waves were generated spontaneously in the jet stream exit region. The horizontal wavelengths and wave periods of the gravity waves were simulated as 600–1000 km and 12–24 hours, respectively. Using a high-resolution 3D nonlinear model, Zhang [2004] simulated gravity wave generation associated with the tropospheric jet stream in the exit region of jet streak. The characteristics of the dominant wave from the simulation were the horizontal wavelength of ∼150 km, the vertical wavelength of ∼2.5 km, and the period of ∼5 hours. Their model also generated the large-scale inertia waves with the horizontal wavelength of ∼600-1000 km, similar to the results by O'sullivan and Dunkerton [1995], but the mid- to high-frequency and small-scale gravity waves dominated in results by Zhang [2004]. These results imply that the in-situ gravity wave sources related to the jets generate not only inertia gravity waves but also meso-scale high frequency gravity waves.

In the stratosphere, the general structures of the gravity wave enhancements observed by CHAMP/GPS correlate well with the stratospheric jet structure rather than the topographical feature in the Antarctic and Arctic [Hei et al., 2008]. Hei et al. [2008] argued that orographic gravity waves are locally important but the jet-related gravity wave sources are likely more important for understanding the gravity wave distributions. The downward propagating gravity waves were observed by radiosonde in the lower stratosphere at Syowa station in Antarctica [Yoshiki and Sato, 2000], which indicated gravity wave sources above their observational heights. Similar downward propagation of gravity waves has been observed in the stratosphere in both the Antarctic and the Arctic [Sato and Yoshiki, 2008; Yamashita et al., 2009; Gerrard et al., 2011]. Considering these observational results, the jet-related gravity wave sources can be as important as the orographic gravity waves in the polar troposphere and stratosphere.

The in-situ gravity wave excitations due to the unbalanced flow can be more prominent during SSWs when the stratospheric polar vortex is extremely disturbed. Nevertheless, gravity wave variations during SSWs have not been inspected in terms of the changes of gravity wave sources but mainly by the changes of gravity wave propagations through the modulations of the background flow [e.g., Whiteway and Carswell, 1994; Wang and Alexander, 2009]. Whiteway and Carswell [1994] explained the reduction of GW-Ep in the altitude range of 25–55 km by the changes of gravity wave vertical wavelength. The gravity wave vertical wavelength was shortened due to the weakening of the background wind in the lower stratosphere. Gravity waves with shorter vertical wavelength tend to break in the lower altitudes, resulting in the weaker GW-Ep in the upper stratosphere. Wang and Alexander [2009] reported the enhancement of gravity wave temperature variance during the 2008 SSW in the altitude range of 20–30 km observed by CHAMP/GPS and COSMIC/GPS. The gravity wave enhancements was likely cased by the increases of the vertical wavelength based on the ray-tracing study. Thurairajah et al. [2010] compared GW-Ep at Chatanika, Alaska (65°N, 147°W) from 2002 to 2005. Based on the high correlation between GW-Ep and background wind speed, they speculated that the filtering of gravity waves due to wind reversal might play a key role in determining their observed gravity wave variations during the 2003 and 2004 SSWs. The falling sphere observed the reductions of gravity wave activity above ∼50 km and a secondary peak of gravity waves at ∼60 km after the peak 2003 SSW in the NH [Wang et al, 2006]. Because of the existence of a critical layer for orographic gravity waves below 60 km, the reductions of gravity waves were likely associated with the filtering of orographic gravity waves.

In contrast to the studies of gravity wave propagation, discussions of gravity wave source variations during SSWs are not comprehensive. Fairlie et al. [1990] showed generations of inertia gravity waves associated with the polar vortex distortion during a SSW using ECMWF data with 5° × 5° resolution. They showed a case of upward and downward phase progressions of gravity waves starting ∼30 km, indicating the in-situ gravity wave source and also the capability of ECMWF in resolving in-situ wave generation at ∼30 km. Wang et al. [2006] speculated that the secondary peak of gravity waves above 60 km during the 2003 SSW was probably due to the secondary gravity wave generation by orographic gravity wave breaking. Wang and Alexander [2009] tried to tie the unbalanced flow in the troposphere to the stratospheric gravity waves. The residual of nonlinear balance equation (ΔNBE) at 350 hPa was used as the indicator of the unbalanced flow. The very weak correlations between ΔNBE at 350 hPa and gravity wave temperature variances were reported, indicating that atmospheric disturbances in the troposphere were less likely to contribute to the enhancement of gravity waves during the 2008 SSW. Although Wang and Alexander [2009] examined the possibility of in-situ gravity wave source variations, their focus was the tropospheric jet at 350 hPa (∼9–10 km) rather than the stratospheric jet. Limpasuvan et al. [2010] used the University of Oklahoma's Advanced Regional Prediction Systems (ARPS) with the horizontal resolution of 10 km and the vertical resolution of 400 m. The ARPS has the upper boundary of 65 km and is capable of resolving gravity waves in the stratosphere. They showed that the gravity waves seen in the stratosphere prior to the 2009 SSW on January 10 were mainly orographic waves. During the peak and after the 2009 SSW, the in-situ gravity wave generations by adjustments of unbalanced flow and the secondary generations by breaking of orographic gravity waves occurred due to the highly disturbed background flow. However, their modeling study was limited to the four key dates (January 10, 20, 25, 30) during the 2009 SSW. The time-series of gravity wave variations and detailed studies using high-resolution models like ECMWF are essential to gain a comprehensive understanding of the roles played by gravity wave source and propagation in SSWs.

The highly disturbed polar vortex can create conditions favorable for the in-situ gravity wave excitation by the unbalanced flow. The current study aims to investigate the physical mechanisms that cause gravity wave variations during the 2009 SSW, focusing on the in-situ gravity wave excitation using ECMWF-T799.

4.2 Gravity Wave Propagation and Source

The physical mechanisms causing the observed gravity wave variations (two peaks of GW-Ep prior to the peak SSW and sudden decay of GW-Ep after the wind reversal) are either changes in the gravity wave propagation or source variations. In this section, the following mechanisms are examined: (1) orographic gravity wave propagation, (2) non-orographic gravity wave propagation,

(3) convectively generated gravity wave propagation from the tropics to the polar region, (4) shear instability, and (5) in-situ wave generations related to unbalanced flow. Gravity wave analysis mainly follows the method introduced in Chapter 2. In this chapter, gravity waves are extracted by two dimensional (2-D) fast Fourier transform (FFT) with a band pass filter to keep gravity waves with horizontal wavelength of 300–600 km.

4.2.1 Orographic Gravity Waves

The Gravity-wave Regional Or Global Ray Tracer (GROGRAT) ray-tracing model is used for gravity wave propagation study. The GROGRAT model is a 4D global ray-tracing model and the detailed descriptions of GROGRAT model can be found in Marks and Eckermann [1995] and Eckermann and Marks [1996]. The GROGRAT model has been intensively used to study gravity wave propagations for various purposes [Gerrard et al., 2004; Li et al, 2009; Lin and Zhang, 2008; Pressue et al., 2009; Wang et al., 2009] and also used for a SSW study [Wang and Alexander, 2009]. The 6-hourly ECMWF outputs of temperature, zonal wind, meridional wind, and vertical wind are used as the background conditions for input to the GROGRAT model.

For orographic gravity waves, gravity wave parameters used for the GROGRAT ray-tracing are the horizontal wavelengths of 200 km and 400 km and the ground-based horizontal phase speed of 0 m/s (stationary relative to ground). It is assumed that these orographic gravity waves propagate against the mean flow at the source level. Orographic gravity waves are launched every 5° latitudes and 10° longitudes at 6 km. Gravity waves are only launched on the land from 30°–80°N. The choice of the horizontal wavelengths of 200 km and 400 km is because the dominant horizontal wavelength during the 2009 SSW is ∼400 km [Yamashita et al., 2010] and mountain waves tend to have shorter horizontal wavelengths. The total numbers of 380 gravity waves with the same characteristics are launched daily from December 20 to January 31. Probabilities are calculated by the numbers of waves reaching 40 km divided by the total number of waves.

Figure 4.1 shows polar plots of the normalized amplitudes of gravity waves reaching 40 km on January 1, 5, 16, and 28. These four dates are chosen to understand gravity wave changes associated with the evolution of planetary waves: typical winter case (before the 2009 SSW) on January 1, PW1 growth and the 1st GW-Ep amplification on January 5, PW2 growth and the 2nd GW-Ep amplification on January 16, and after the wind reversal on January 28. Amplitudes are normalized by the maximum amplitudes to show relative changes of gravity wave amplitudes. Figure 4.2 shows the maximum magnitudes of wind rotation that is defined by the changes of background wind directions through 5–40 km as shown below [Whiteway et al., 1997; Yamashita et al., 2009].

$$\text{Wind Rotation (z)} = |\text{Wind Direction (z) - Wind Direction (at 5km) }|$$

For example, if wind direction at 5 km is 30°E and at 10 km is 130°E, then wind rotation is a change of wind direction, 100°. Larger wind rotation indicates larger changes of wind directions and thus higher probabilities of filtering orographic gravity waves. In Figure 4.1 on January 1, gravity wave amplitudes are larger in the longitudinal range of 45°–180°E and in the latitude range of 60°–70°N. In this region, wind rotations are small (blue color) as shown in Figure 4.2 indicating that this region is a favorable region for orographic gravity wave propagation, which is consistent with the GROGRAT ray-tracing results. Wind rotations on January 28 are smaller around 35°–180°E and 60°–70°N, and gravity wave amplitudes are larger in the same region. Comparing Figure 4.1 to 4.2, the locations of large gravity wave amplitudes generally anti-correlate with wind rotations. Some discrepancies between wind rotations and GROGRAT results are likely due to the horizontal propagation considered in the GROGRAT but not in wind rotation. Overall GROGRAT results appear to be reasonable when compared with wind rotation results.

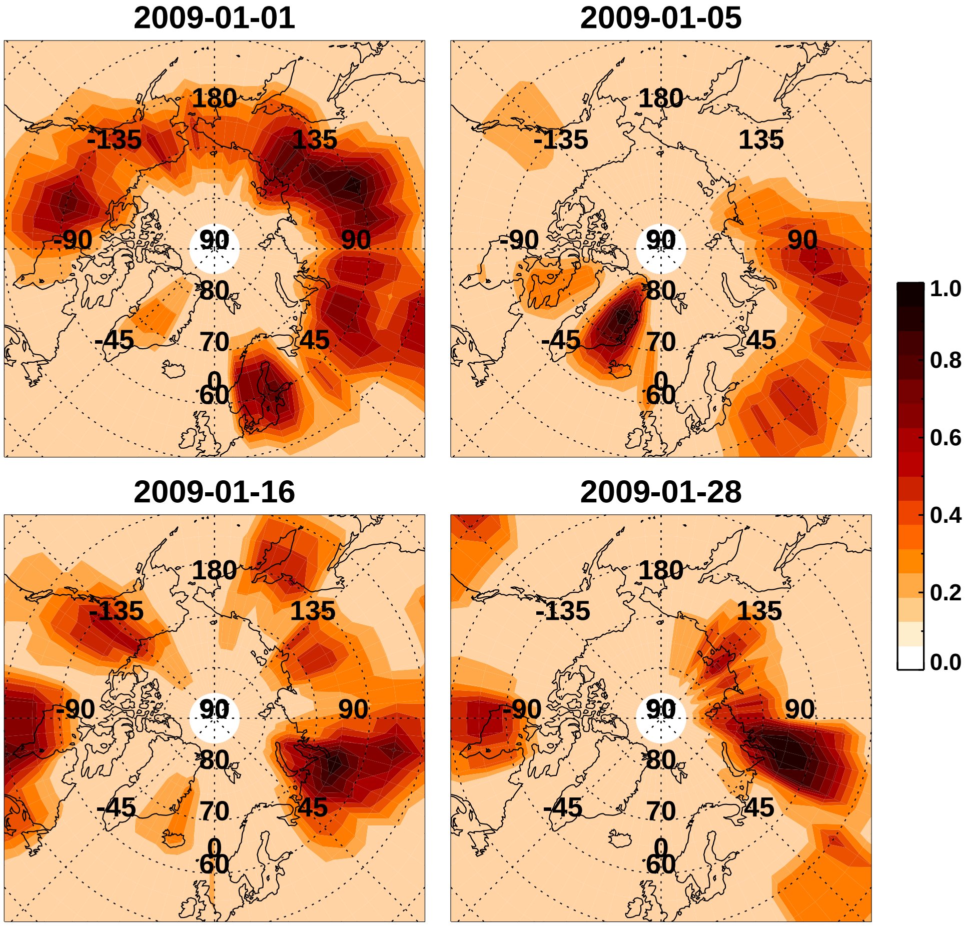

Figure 4.1: Normalized gravity wave amplitudes reaching 40 km calculated by the GROGRAT ray-tracing model with ECMWF background temperatures and winds

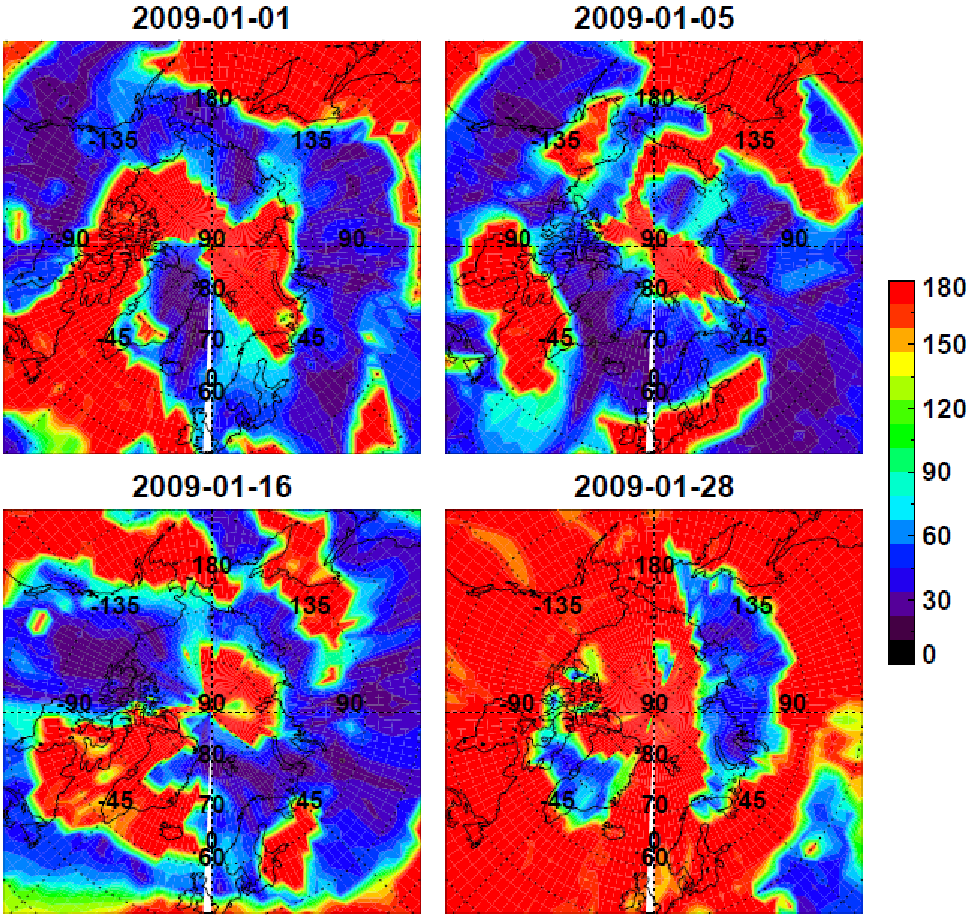

Figure 4.2: Polar map of wind rotation between 5 km and 40 km using zonal and meridional winds from ECMWF-T799

Figure 4.3a displays the time-series of normalized probability of orographic gravity waves reaching 40 km computed from the GROGRAT model. Probabilities are normalized by the maximum probabilities of gravity waves reaching 40 km between January 1 and January 31. The zonal mean GW-Ep calculated by ECMWF-T799 averaged over the altitude range of 35–60 km in the latitude range of 65°-70°N are overlaid on Figure 4.3. The GW-Ep shows two peaks on January 5 and 16 and decay after ∼January 21. The normalized probabilities of orographic gravity wave propagation in Figure 4.3a show a periodicity of roughly 5 days. This 5-day periodicity probably results from the modulations of the background flow by 5-day planetary waves. The 5-day oscillations in the normalized probability do not correlate with the two peaks of GW-Ep variations. However, the decay of GW-Ep after January 20 corresponds well with the decrease of probability in gravity wave propagations. To quantify the relationship between GW-Ep and the normalized probability of orographic wave propagation, the linear correlation coefficients (LCC) between the normalized probability and GW-Ep variations for different periods are calculated. The LCC for the overall period from January 1 to January 28 is 0.39 with over 95% significance level. It increases to 0.67 (over 95% significance level) for the period from January 18 to 28 considering only after wind reversal but significantly decreases for the period from January 1 to 18 before wind reversal without any statistically significant correlations. These statistical results indicate that the changes in orographic gravity wave propagation are important for the reduction of GW-Ep during and after the wind reversal (January 18–28). However, such propagation changes do not likely contribute to the two peaks of GW-Ep before the wind reversal on January 5 and 16.

4.2.2 Nonorographic Gravity Waves

Gravity waves excited by nonorographic wave sources (e.g., convection, frontal system, and geostrophic adjustment) are considered as nonorographic gravity waves. In this section, the changes in the propagation of nonorographic gravity waves excited in the troposphere are examined using GROGRAT model. Gravity waves are launched at 12 km considering gravity wave generation by the tropospheric jet [Zhang, 2004; Osullivan and Dunkerton, 1995]. Gravity waves are launched

(a) Orographic waves

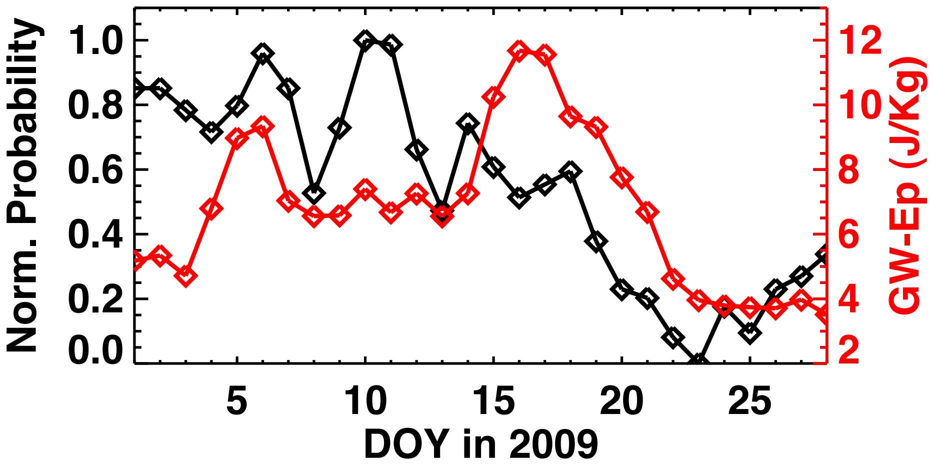

(b) Non-orographic waves

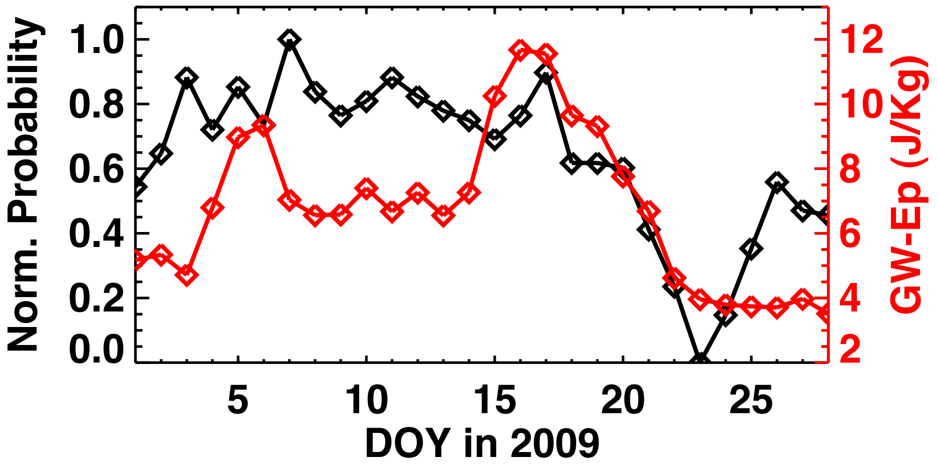

Figure 4.3: (Black) Normalized probabilities of (a) orographic and (b) non-orographic gravity wave reaching 40 km from the GROGRAT ray-tracing model. (Red) zonal-daily mean GW-Ep in the latitude range of 65–70°N and in the altitude range of 35–60 km.

every 10° latitudinal and 25° longitudinal grids from the latitude range of 5°–75°. The horizontal wavelength is 400 km, and the ground-based horizontal phase speeds are 15 m/s and 30 m/s. Gravity wave propagation directions are homogeneously distributed between 0° and 360° for every 60° assuming equal possibility for gravity waves to propagate in any direction. Figure 4.3b shows the normalized probabilities of gravity waves that reach 40 km. The probabilities of non-orographic wave propagations also exhibit some modulations before January 20; however, they do not match the two peaks of GW-Ep. The LCC between the normalized probability and GW-Ep from January 1 to 28 is 0.56 with over 95% significance level. Before the wind reversal from January 1 to 18, the LCC is 0.05, and after the wind reversal from January 18 to 28, the LCC is 0.61. These statistical results also indicate that the changes in nonorographic gravity wave propagation contribute to the reduction of GW-Ep after wind reversal but not to the two peaks of GW-Ep before the wind reversal.

4.2.3 Propagation of Convective Gravity Waves from the Tropics to Polar Region

Besides gravity waves generated in the polar region, it is possible that the GW-Ep enhancements observed in the stratosphere and the mesosphere are caused by waves propagating from the tropics [Sato, 2000]. The enhancements of the tropical convection during SSWs are reported by Eguchi and Kodera [2007] due to the changes of the Brewer-Dobson circulations by planetary wave amplifications. It is thus possible that these enhanced tropical convections stimulate additional gravity wave generation, and the meridional propagations of the amplified tropical gravity waves cause the gravity wave enhancements in the polar stratospheric and mesosphere.

In order to examine such a possibility, Figure 4.4 displays the time-series of convective precipitation obtained from the output of ECMWF-T799. Here, the convective precipitation is used as an indicator of the strength of convective gravity wave sources in the tropics. The convective precipitation in the tropics increases after January 16 probably related to the 2009 SSW as suggested by Eguchi and Kodera [2007]. Further examining the changes in meridional propagation of gravity waves, Figure 4.5 illustrates the time variations of energy flux and the vertical fluxes of zonal and meridional momentum. These fluxes are computed by using the method introduced in Chapter 2. When energy flux ($\overline{p'w'}$) is positive (negative), the positive (negative) meridional momentum fluxes represent the northward gravity wave propagation. In Figure 4.5, the upward gravity wave energy flux dominates, and the positive meridional momentum fluxes indicate the northward propagation. The magnitudes of meridional momentum flux decrease after January 15. This result indicates that the meridional propagation of gravity waves from the tropics to the polar region is weaker during the period with the GW-Ep enhancements around January 16 than that during the normal winter conditions. Hence, gravity wave propagation from the tropics may not contribute to two peaks of GW-Ep in the polar stratosphere and the lower mesosphere. It is worth to point out that the propagation time for the tropical gravity waves to reach the polar region needs to be considered if a thorough analysis on this subject is to be conducted. Since this thesis focuses more on the wave sources, it will not be addressed further in the current work.

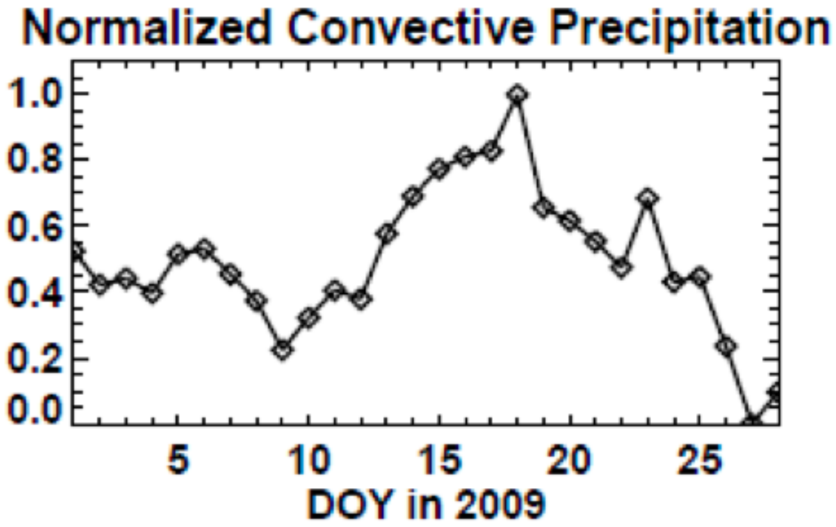

Figure 4.4: ECMWF tropical convective precipitation averaged over the tropics, 15°S–15°N.

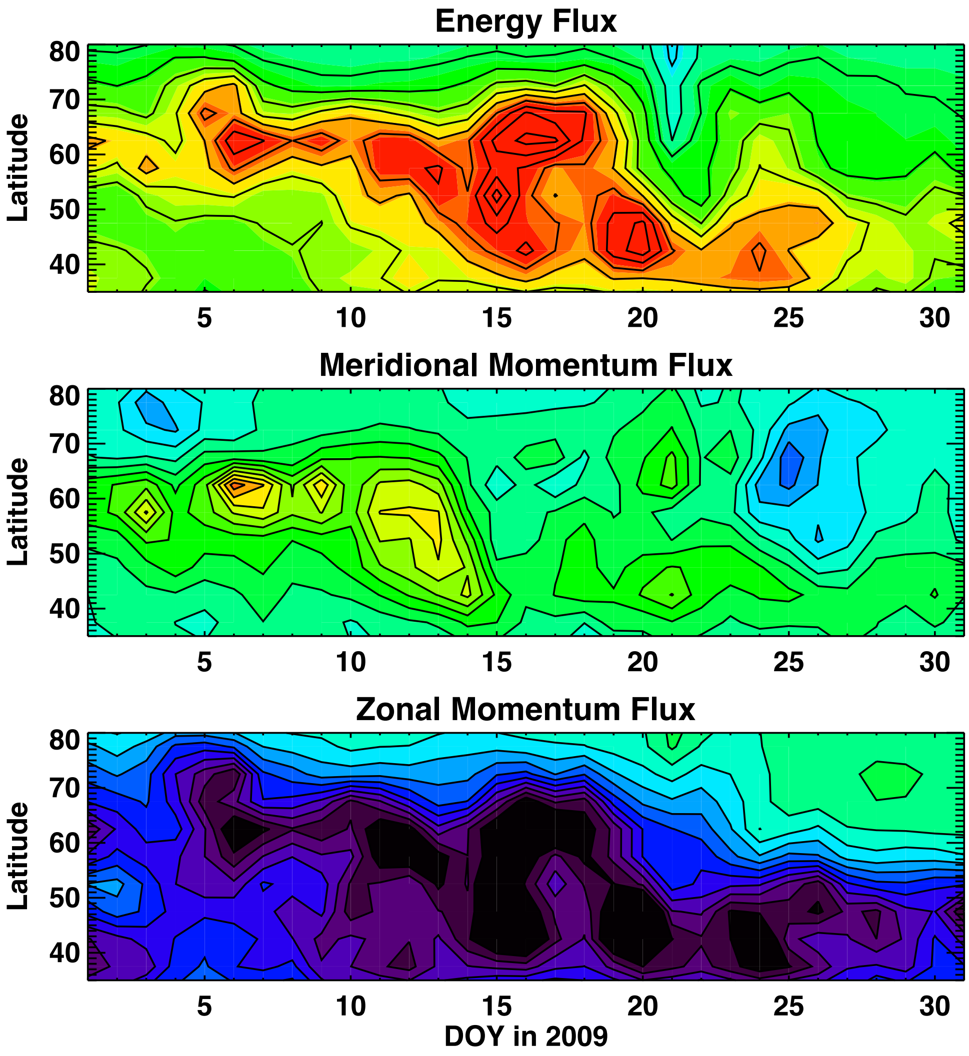

Figure 4.5: (Top) Energy flux, $\overline{p'w'}$, vertical fluxes of (middle) meridional momentum and (bottom) zonal momentum integrated over longitude range of 0–360° and altitude range of 10–40 km.

4.2.4 In-situ Gravity Wave Sources

In addition to the changes in gravity wave propagation, it is possible that planetary wave amplifications alter the in-situ gravity wave generations during the 2009 SSW. In order to study the source and sink of gravity waves, the total perturbation energy flux, F_E, is used here [Hines and Reddy, 1967; Lindzen, 1990]. F_E is defined as:

$$F_E = \overline{p'w'} + U\rho\overline{u'w'} + V\rho\overline{v'w'}. \tag{4.1}$$

F_E is conserved if no dissipation of gravity wave occurs. The decrease and increase of F_E with altitude indicate the sink and source of gravity waves, respectively.

Figure 4.6 shows the line plots of zonal-daily mean of F_E in the different latitude bands. In Figure 4.6, January 1, 5, 16, and 28 can be considered as the typical winter condition, time with PW1 growth, time with PW2 growth, and after the SSW, respectively. On January 1, F_E is the largest in the lower stratosphere and decaying above 20 km for all latitude regions except latitude band of 60°–70°N. Decaying of F_E indicates the strong gravity wave dissipation above 20 km. The slight increases of F_E above ∼25-30 km in the latitude range of 60°–70°N represent the existence of in-situ energy source under the normal winter conditions. On January 5, F_E in 30°–50°N decays above 20 km, but F_E in 60°–75°N increases above ∼25 km. On January 16, F_E in 30°–45°N decays above 17 km, and F_E in 45°–60°N increases by two-fold in the altitude range of 20–30 km and 37–45 km. F_E in 60°–70°N keeps increasing above ∼25 km but F_E in 70°–90°N stays constant from ∼15 km to 45 km with very weak gravity wave amplitudes. In contrast to F_E on January 5 and 16, F_E in all latitude bands on January 28 decays or stays constant above 20 km. Note that, F_E on January 1 above 30 km is larger than that on January 28. F_E on January 1 (normal winter conditions) exhibits some in-situ energy increase in between the altitude range of 20–45 km but not on January 28. These results suggest that in-situ energy source is weaker after the 2009 SSW than under normal winter conditions.

To examine the locations of in-situ energy source, the vertical gradient of F_E between 20 and

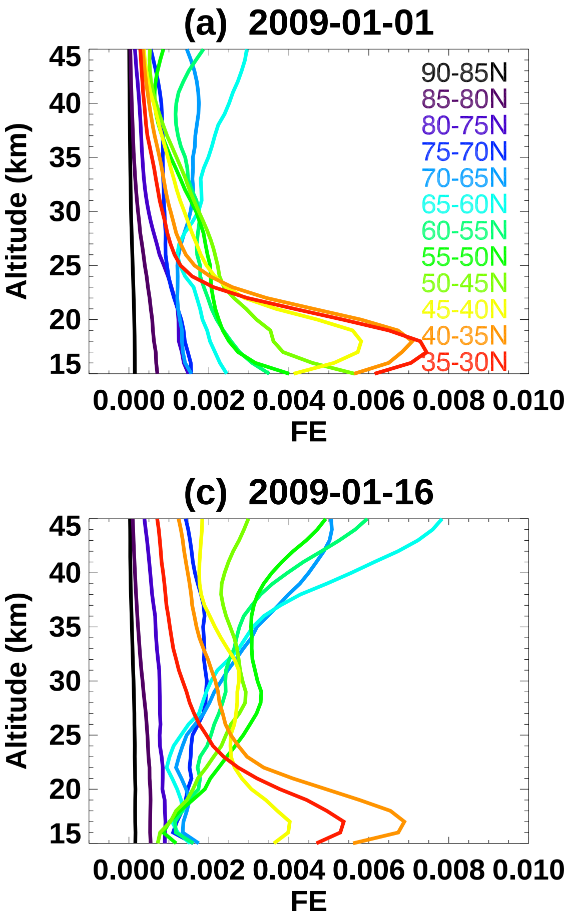

Figure 4.6: Daily mean total energy flux of gravity waves with horizontal wavelength of 300–600 km on (a) January 1, (b) January 5, (c) January 16, and (d) January 28. Each color represents different latitudes.

45 km are shown as polar plots in Figure 4.7. The vertical gradient is simply obtained from the following equation:

$$Vertical\ \ Gradient\ \ of\ \ F_E = \frac{F_E(45\ km)\ \ -\ \ F_E(20\ km)}{25\ \ km} \tag{4.2}$$

As indicated by Hines and Reddy [1967] and Lindzen [1990], the positive and negative gradients of F_E indicate the source and sink of gravity waves, respectively. There are slight increase of F_E in the longitudinal range of 45°–130°E at 60°–70°N on January 1. On January 5, the large enhancement of F_E occurs in the longitudinal range of 70°–130°E at 60°–70°N. On January 16, the positive gradients of F_E peak in the longitudinal range of 170°–225°E at 60–70°N and in the longitudinal range of 280°–360°E at 60°–70°N when PW2 growth starts. On January 28 after the peak SSW, there is no obvious in-situ energy increase. A peak on January 5 and two peaks on January 16 are well correlated with the locations of strong gravity wave signature in Figure 3.3 in Chapter 3.

Illustrated in Figure 4.8 are the time-series of vertical gradients of F_E along with GW-Ep. The two peaks of GW-Ep on January 5 and 16 correlate well with the vertical gradient of F_E. The LCC between GW-Ep and the vertical gradient of F_E is 0.63 from January 1 to 28 but increases to 0.82 (over 95% of confidence level) with data only from January 1 to January 20 excluding the decay of GW-Ep and a sharp peak on January 21. The sharp peak on January 21 is likely be related to ducted gravity waves. The altitude range of 20–45 km only covers some portion of the ducted gravity waves, resulting in the sharp peak on January 21. This ducted wave is interesting feature but is beyond our scope in this study. The high correlations between the in-situ energy source and GW-Ep variations indicate that the gravity wave enhancements prior to the peak SSW are most likely related to the in-situ energy sources. The vertical gradients of F_E also exhibit decay after January 22, so the suppression of in-situ energy sources may have contributed to the reduction of GW-Ep after the wind reversal.

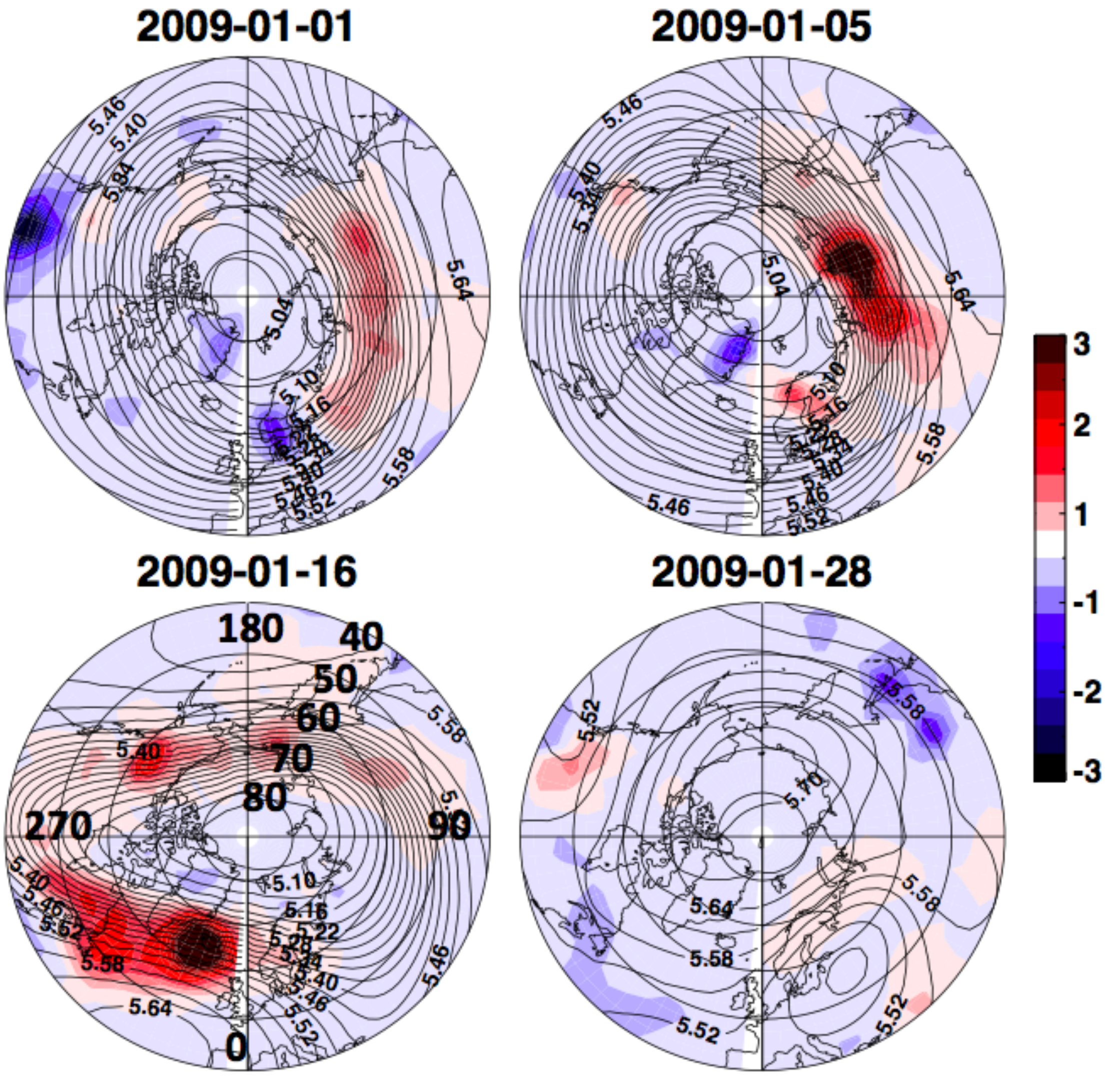

Figure 4.7: Polar plots of the daily mean vertical gradient of total energy flux between 20 km and 45 km on (a) January 1, (b) January 5, (c) January 16, and (d) January 28. Black line contours represent constant pressure levels

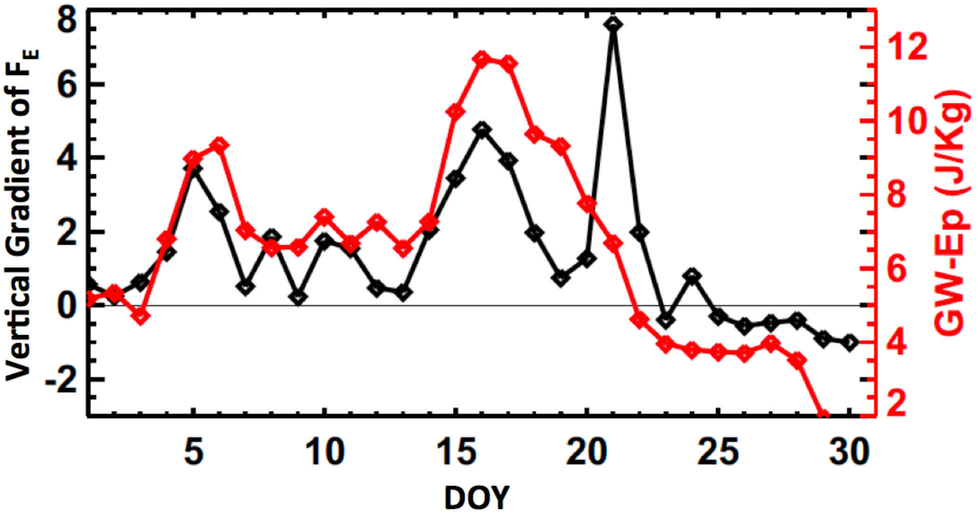

Figure 4.8: Time variations of the vertical gradient of total energy flux between 20 and 45 km in the latitude range of 65–70°N. (Red line) GW-Ep is averaged over the altitude range of 35–60 km and the latitude range of 65–70°N.

4.3 In-situ Gravity Wave Generations

4.3.1 Temporal and Spatial Variations of Residual Tendencies

The in-situ gravity wave generations by unbalanced flow related to the jet structures are usually indicated by the intensity of unbalanced flow. The Lagrangian Rossby number [Koch and Dorian, 1988; Zhang et al., 2000; Liu and Meriwether, 2004], the residual of nonlinear balance (ΔNBE) [Zhang et al., 2000; Zhang, 2004], and the residual tendencies [Snyder et al., 2007; 2009] have been used as indicators of the in-situ gravity wave source. In this study, the residual tendencies introduced by Snyder et al. [2007, 2009] are employed to study the in-situ gravity wave generation. Following Snyder et al. [2009], the momentum equations for zonal and meridional directions are written as:

$$\frac{\partial u}{\partial t} = -u\frac{\partial u}{\partial x} - v\frac{\partial u}{\partial y} + fv - \frac{\partial \Phi}{\partial x} \tag{4.3}$$

$$\frac{\partial v}{\partial t} = -u\frac{\partial v}{\partial x} - v\frac{\partial v}{\partial y} - fu - \frac{\partial \Phi}{\partial y} \tag{4.4}$$

where Φ is the total geopotential, u is the total zonal wind, v is the total meridional wind, and f is the Coriolis parameter. Total flow (u , v , Φ) can be separated into the large scale part (denoted by overbars) and the unbalanced or perturbation part (denoted by primes):

$$(u, v, \Phi) = \left(\overline{u}, \overline{v}, \overline{\Phi}\right) + (u', v', \Phi') \tag{4.5}$$

Substituting Equation 4.5 into primitive Equations 4.3 and 4.4, then the following equations are obtained:

$$\frac{\partial \overline{u}}{\partial t} + \overline{\mathbf{U}} \cdot \nabla \overline{u} + f\overline{v} + \frac{\partial \overline{\Phi}}{\partial x} = -\frac{\partial u'}{\partial t} - \mathbf{U}' \cdot \nabla u' - \mathbf{U}' \cdot \nabla \overline{u} - \overline{\mathbf{U}} \cdot \nabla u' + fv' - \frac{\partial \Phi'}{\partial x} \tag{4.6}$$

$$\frac{\partial \overline{v}}{\partial t} + \overline{\mathbf{U}} \cdot \nabla \overline{v} - f\overline{u} + \frac{\partial \overline{\Phi}}{\partial y} = -\frac{\partial v'}{\partial t} - \mathbf{U}' \cdot \nabla v' - \mathbf{U}' \cdot \nabla \overline{v} - \overline{\mathbf{U}} \cdot \nabla v' - fu' - \frac{\partial \Phi'}{\partial y} \tag{4.7}$$

Right hand side of above equations describes the fluid flow of perturbed flow, and the left hand side can be regarded as the residual tendencies acting as forcing terms of the perturbed flow:

$$F_u = -\frac{\partial u'}{\partial t} - \mathbf{U}' \cdot \nabla u' - \mathbf{U}' \cdot \nabla \overline{u} - \overline{\mathbf{U}} \cdot \nabla u' + fv' - \frac{\partial \Phi'}{\partial x} \tag{4.8}$$

$$F_v = -\frac{\partial v'}{\partial t} - \mathbf{U}' \cdot \nabla v' - \mathbf{U}' \cdot \nabla \overline{v} - \overline{\mathbf{U}} \cdot \nabla v' - fu' - \frac{\partial \Phi'}{\partial y} \tag{4.9}$$

where:

$$F_u = \frac{\partial \overline{u}}{\partial t} + \overline{\mathbf{U}} \cdot \nabla \overline{u} - f\overline{v} + \frac{\partial \overline{\Phi}}{\partial x} \tag{4.10}$$

$$F_v = \frac{\partial \overline{v}}{\partial t} + \overline{\mathbf{U}} \cdot \nabla \overline{v} + f\overline{u} + \frac{\partial \overline{\Phi}}{\partial y} \tag{4.11}$$

In spherical coordinates, they become

$$F_u = \frac{\partial \overline{u}}{\partial t} + \frac{\overline{u}}{acos\phi}\frac{\partial \overline{u}}{\partial \lambda} + \frac{\overline{v}}{a}\frac{\partial \overline{u}}{\partial \phi} - f\overline{v} + \frac{1}{acos\phi}\frac{\partial \overline{\Phi}}{\partial \lambda} - \frac{\overline{u}\overline{v}tan\phi}{a} \tag{4.12}$$

$$F_v = \frac{\partial \overline{v}}{\partial t} + \frac{\overline{u}}{acos\phi}\frac{\partial \overline{v}}{\partial \lambda} - \frac{\overline{v}}{a}\frac{\partial \overline{v}}{\partial \phi} + f\overline{u} + \frac{1}{a}\frac{\partial \overline{\Phi}}{\partial \phi} + \frac{\overline{u}^2 tan\phi}{a} \tag{4.13}$$

where ϕ is latitude, λ is longitude, and a is the mean radius of the earth.

These equations indicate that the residual tendency terms, Fu and Fv, are zero if the flow is fully balanced. The generation mechanism is schematically illustrated in Figure 4.9. When an air parcel moves through the flow field, it is subject to these residual tendencies and experiences displacements. The residual tendencies are associated with the large-scale flow, which is quasi-stationary prior to warming. Therefore, the spatial scale of the residual tendencies and the velocity of the parcel determine the time of the air parcel moving through the forcings and thus the frequencies of gravity waves excited. This is somewhat analogous to the excitation of an orographic wave. This Lagrangian view of gravity wave excitations by jet is discussed by Snyder et al. [2009].

In this study, the large-scale flow ($\overline{u}$, $\overline{v}$,$\overline{\Phi}$) is defined as the sum of zonal wavenumber 0–4 components of zonal wind and meridional wind. In order to exclude the contributions of the higher-order terms in nonlinear terms, Fu and Fv are calculated using the following equations for this study.

$$F_u = \frac{\partial \overline{u}}{\partial t} + \overline{\frac{u}{acos\phi}\frac{\partial u}{\partial \lambda}}^{(0-4)} + \overline{\frac{v}{a}\frac{\partial u}{\partial \phi}}^{(0-4)} - f\overline{v} + \frac{1}{acos\phi}\frac{\partial \overline{\Phi}}{\partial \lambda} - \overline{\frac{uvtan\phi}{a}}^{(0-4)} \tag{4.14}$$

$$F_v = \frac{\partial \overline{v}}{\partial t} + \overline{\frac{u}{acos\phi}\frac{\partial v}{\partial \lambda}}^{(0-4)} - \overline{\frac{v}{a}\frac{\partial v}{\partial \phi}}^{(0-4)} + f\overline{u} + \frac{1}{a}\frac{\partial \overline{\Phi}}{\partial \phi} + \overline{\frac{u^2tan\phi}{a}}^{(0-4)} \tag{4.15}$$

where nonlinear terms are denoted by the long overbars with (0-4) that are advection terms and curvature terms, and the rests (time tendency, pressure gradient force, and Coriolis forces) are liner terms. Linear terms are calculated using the large-scale flow ($\overline{u}$, $\overline{v}$,$\overline{\Phi}$) that are zonal wavenumber 0-4 components of zonal wind and meridonal wind. The overbars with (0-4) represent that terms are calculated using the total flow of zonal wind and meridonal wind (u, v), and then the wavenumber 0-4 components of nonlinear terms calculated with the total winds (u, v) are extracted as nonlinear terms to calculate Fu and Fv using Equations 4.14–4.15.

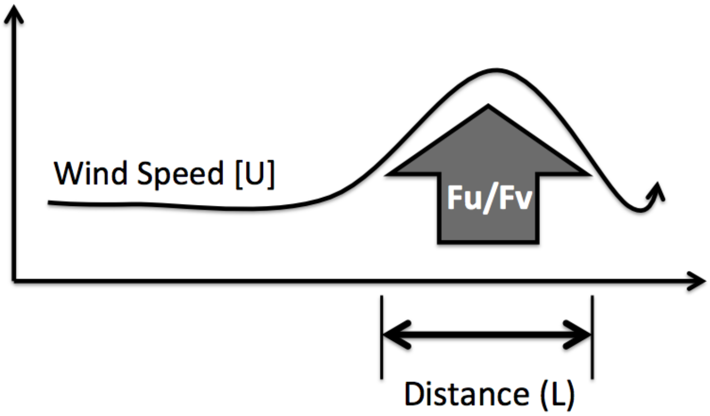

Figure 4.9: Schematics of gravity wave generations by the residual tendencies, Fu and Fv. Gray arrow indicates forcings of Fu and Fv, and black arrow indicates the trajectory of an air parcel.

The residual tendencies, Fu and Fv, calculated using Equations 4.12–4.13 are shown in Figures 4.10–4.11 at 1 hPa on January 5, 11, 16, and 28. On January 5 at 1 hPa, the large Fu and Fv exist in the longitudinal region of 45°–180° as shown by the black circles, which is consistent with the large gravity wave activity region in Figure 3.3. On January 16, Fu and Fv become large in the longitudinal regions of 110°–220° and 270°–360° as indicated by black circles. The distributions of Fu and Fv on January 16 also match well with the large gravity wave activity region in Figure 3.3. In contrast to Fu and Fv at 1 hPa on January 5 and 16, Fu and Fv on January 11 and 28 are weaker, and the gravity wave excitation is also weaker.

To study the temporal variations of the magnitudes of residual tendencies, the daily-zonal mean Fu and Fv are shown in Figure 4.12. Both Fu and Fv show two peaks on January 5 and 16 and are weak after January 25. These variations are well correlated with the GW-Ep variations in Figure 3.4 and also the vertical gradient of F_E variations in Figure 4.8. The large Fu and Fv are extended to lower altitudes on January 16 than those on January 5, and these downward progressions of Fu and Fv are also consistent with the downward progressions of peak GW-Ep discussed in Chapter 3. These results strongly indicate that in-situ gravity wave excitations by spontaneous responses to the residual tendencies are most likely the key mechanisms responsible for the gravity wave variations associated with the 2009 SSW.

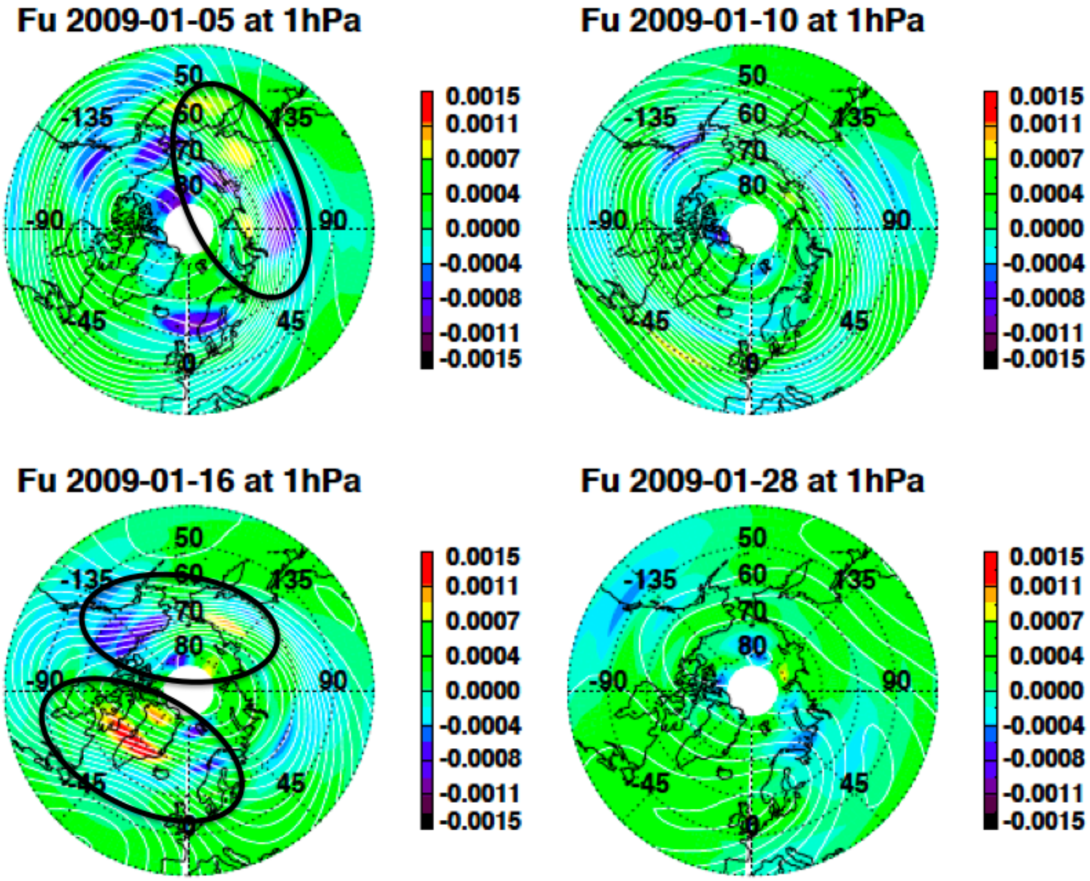

Figure 4.10: Polar plots of Fu on January 5, 11, 16, and 28 at 1 hPa. White line contours indicate geopotential height.

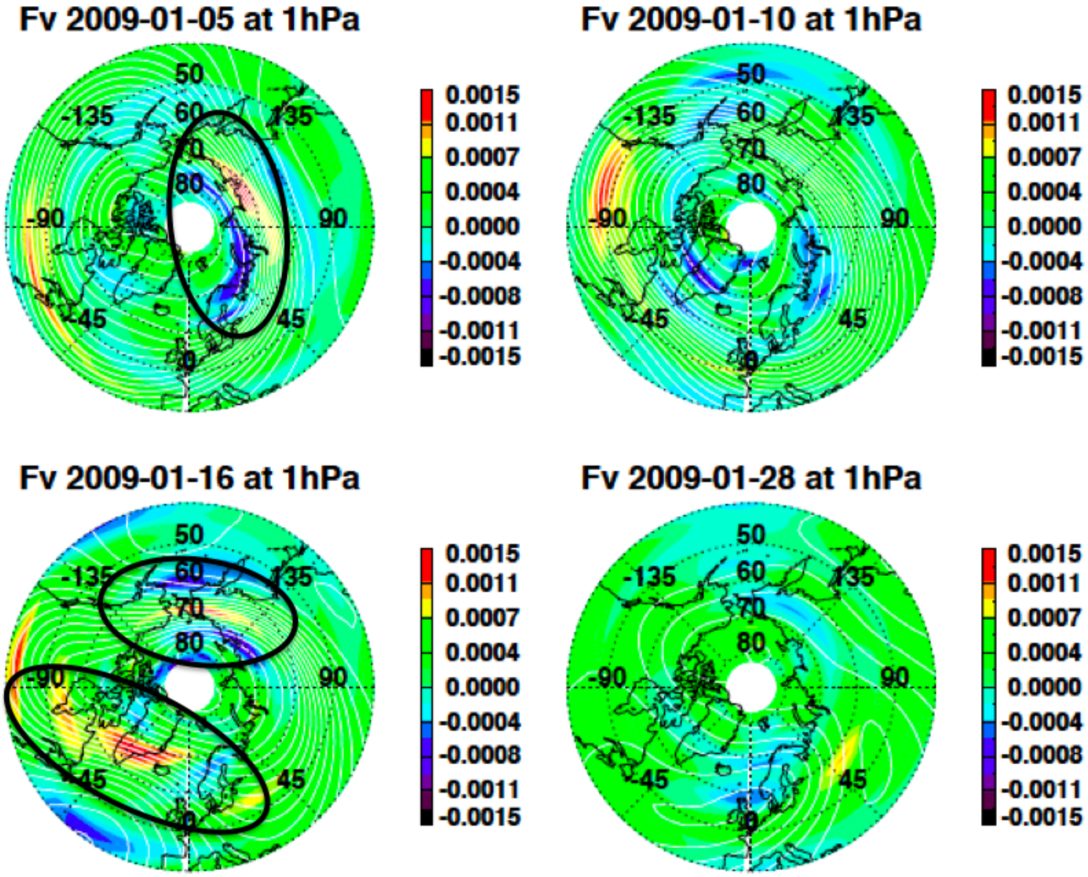

Fv 2009-01-05 at 1hPa

Fv 2009-01-10 at 1hPa

Fv 2009-01-16 at 1hPa

Fv 2009-01-28 at 1hPa

Figure 4.11: Polar plots of Fv on January 5, 11, 16, and 28 at 1 hPa. White line contours indicate geopotential height.

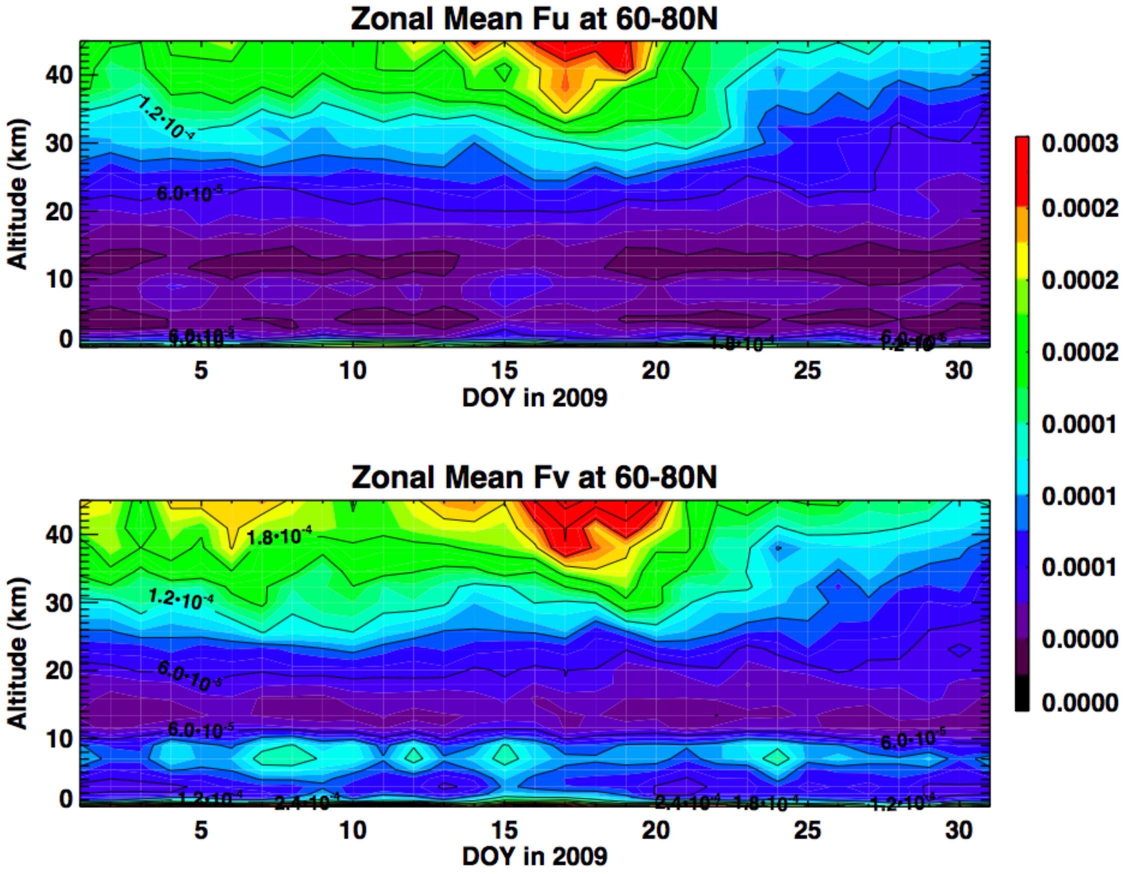

Figure 4.12: Zonal-daily mean of (top) Fu and (bottom) Fv in the latitude range of 60°–70°N.

4.3.2 Case Study of In-situ Wave Generations

The total perturbation energy fluxes, residual tendencies, and GW-Ep indicate that the in-situ gravity wave excitations by spontaneous responses to the residual tendencies are likely responsible for two peaks of GW-Ep. In this section, the wave generation on January 16 is further examined in details at a particular location. Note that, ECMWF-T799 data used here is a hourly forecast data that is a spacial version of ECMWF-T799, allowing us to examine the in-situ gravity wave excitation.

Background Structure

Figures 4.13 and 4.14 show polar plots of gravity waves and the background flow with hourly ECMWF forecast data at 1 hPa and 10 hPa, respectively. There are two distinct locations of jet distortions and strong gravity wave activities in the longitudinal regions of 135–225°E (top side of polar plots) and 280–360°E (bottom side of polar plots) around 60–70°N both at 1 hPa and 10 hPa, even though some detailed wave structures and locations are somewhat different between the two layers. The clear polar vortex signatures exist in the zonal wind field at both 1 hPa and 10 hpa. Zonal wind at 1 hPa is generally stronger than that at 10 hPa. The maximum zonal winds exceed 80 m/s in 180–225°E and 325–360°E at 10 hPa and 120 m/s in 165–195°E and 330–360°E at 1 hPa. Amplitudes of wavenumber 2 components of meridional wind perturbations are larger at 1 hPa than those at 10 hPa. The temperature in the polar region is still colder than that outside of the polar vortex at 10 hPa. At 1 hPa, the temperature in the polar region begins to warm up and shows significant longitudinal variations. This case study focuses on gravity wave generation in the region of the black boxes shown in Figure 4.13 and 4.14. The region of the black box is between Alaska and Russia and has relatively less topographical feature compared to the regions of 280–360°E where Greenland is a probable location for orographic gravity waves. The chosen region contains the jet exit region that creates conditions favorable for the in-situ spontaneous gravity wave generation [Uccellini and Koch, 1987].

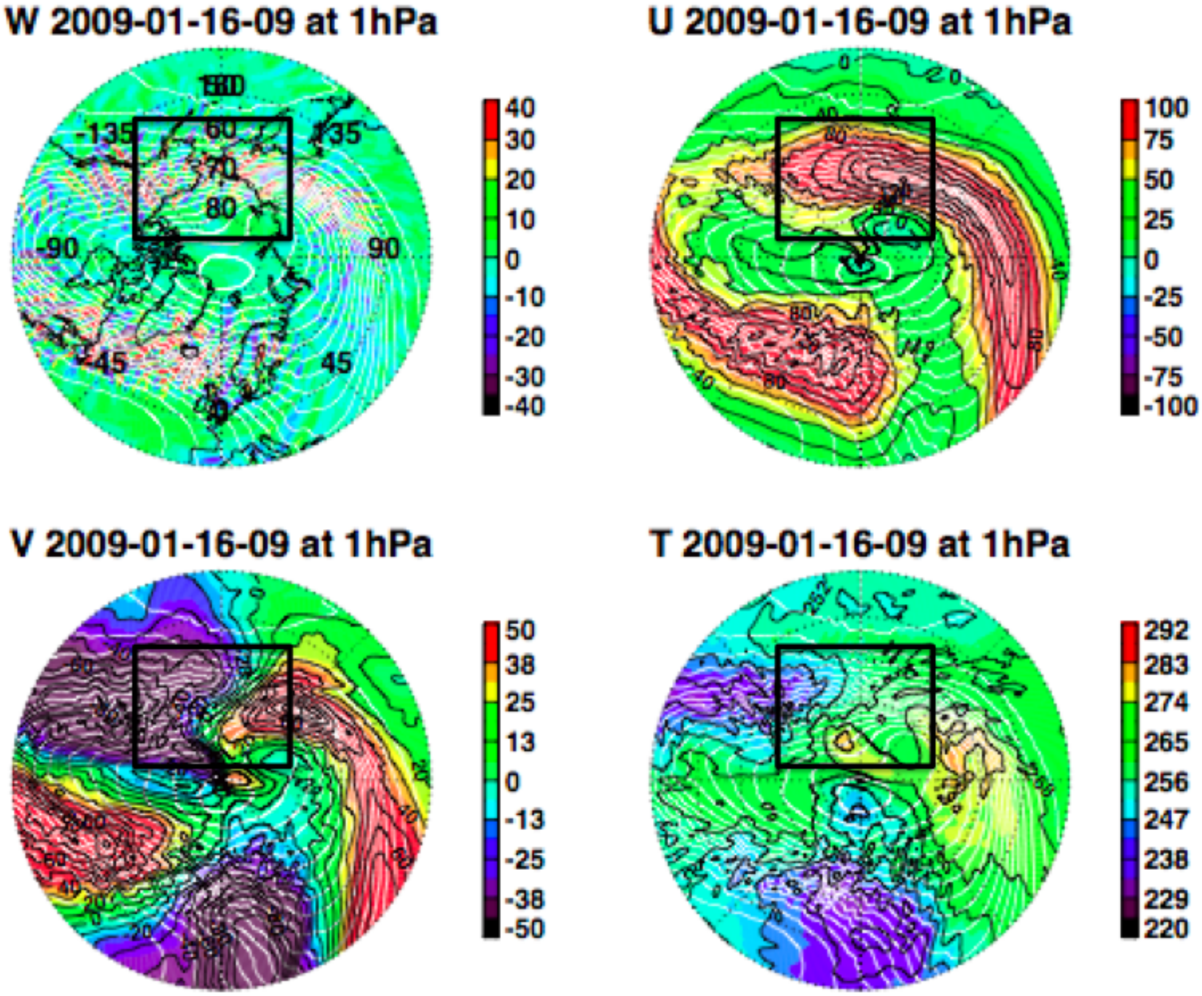

W 2009-01-16-09 at 1hPa

U 2009-01-16-09 at 1hPa

V 2009-01-16-09 at 1hPa

T 2009-01-16-09 at 1hPa

Figure 4.13: Polar plots of vertical wind (w), zonal wind (U), meridional wind (V), and temperature (T) at 1 hPa on January 16, 2009 at 0 UT. Blackbox indicates a region of case study shown in the following sections. White line contours represent geopotential height. Thick black lines indicate continents.

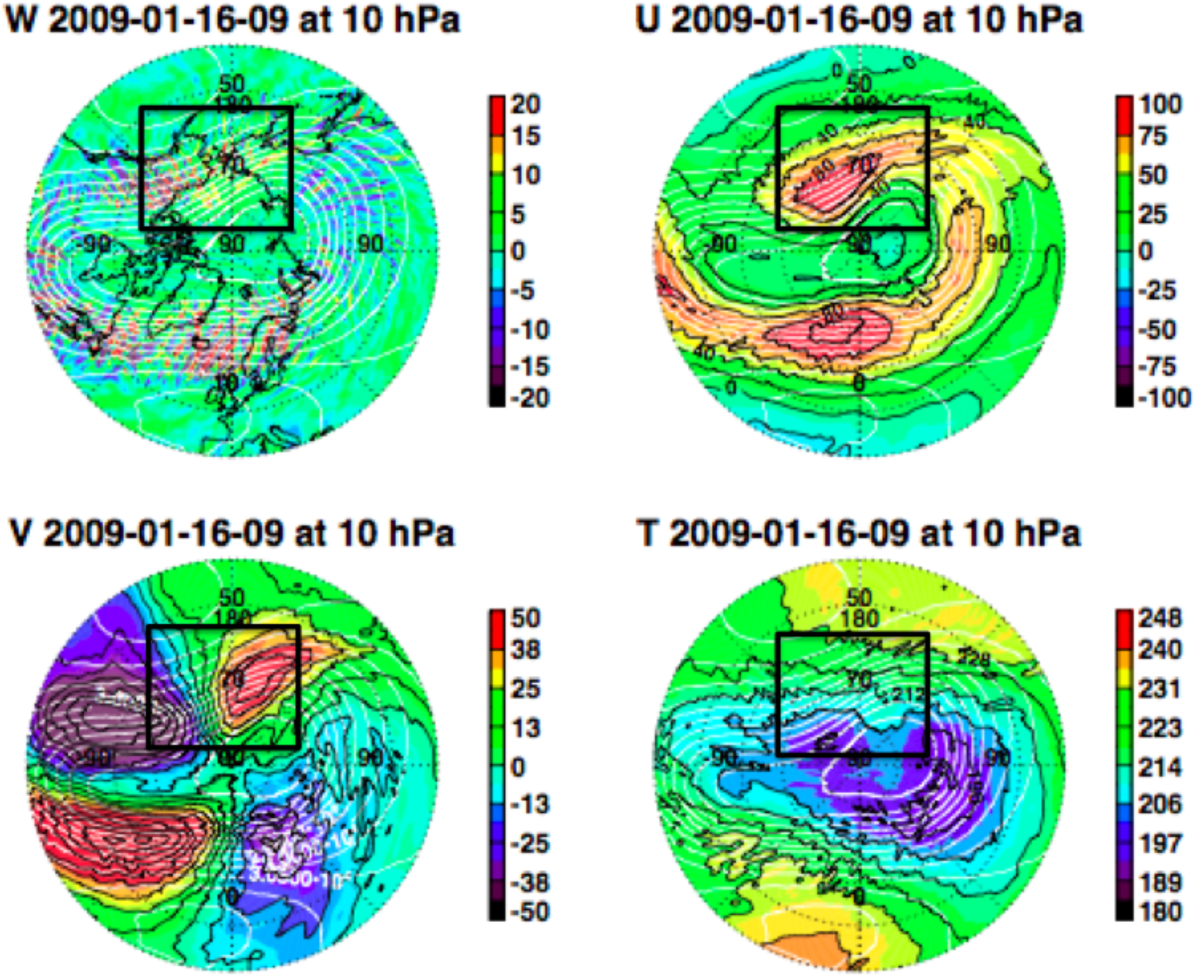

W 2009-01-16-09 at 10 hPa

U 2009-01-16-09 at 10 hPa

V 2009-01-16-09 at 10 hPa

T 2009-01-16-09 at 10 hPa

Figure 4.14: Same as Figure 4.13 but at 10 hPa.

Evolutions of Gravity Waves

Plotted in Figure 4.15 is the time variation of vertical wind gravity wave variances that are integrated in the region of 50–85°N and 150–200°E shown by the black boxs in Figures 4.13–4.14. The sharp increase of gravity wave variances occurs on January 16 from 8 UT to 13 UT, and this case study examines the period from 8 UT to 18 UT in this region.

Figures 4.16–4.17 show the evolutions of gravity waves and geopotential height fields from the hourly ECMWF-T799 forecast data. The hourly ECMWF-T799 forecast data is initialized at 12 UT every day and runs 36 hours without any assimilation process. The period of 8–18 UT used in this case study does not include any assimilation process. Gravity waves in Figures 4.16–4.17 are normalized by the square root of atmospheric density to compensate the exponential growth of gravity wave amplitudes. If gravity waves propagate from below without any dissipation, the same amplitudes of gravity waves should show up at both 1 hPa and 50 hPa. In both Figures 4.16 and 4.17, strong gravity wave activities occur over Alaska (right top corner of each plot) at 1 hPa and 50 hPa. Normalized amplitudes of gravity waves are stronger at 50 hPa than those at 1 hPa over Alaska, indicating that these gravity waves originate in the lower atmosphere and some of the gravity waves are dissipated between the troposphere and the stratosphere. On the other hand, the gravity waves between Russia and Alaska at 1 hPa specified by black boxes do not have obvious connections with the lower atmosphere at 50 hPa. These gravity waves in black boxes likely originate between 50 hPa and 1 hPa.

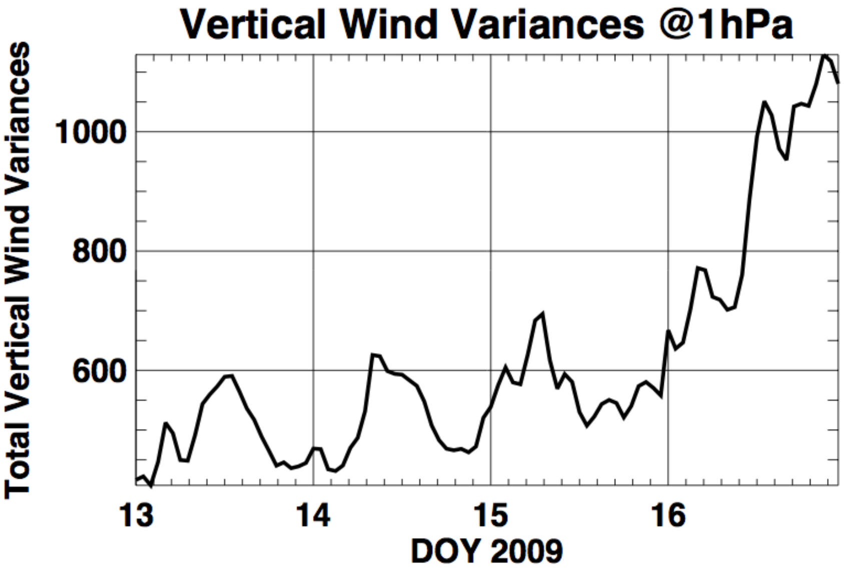

Figure 4.15: Time-series of vertical wind variances integrated over 50–85°N and 150–200°E at 1 hPa

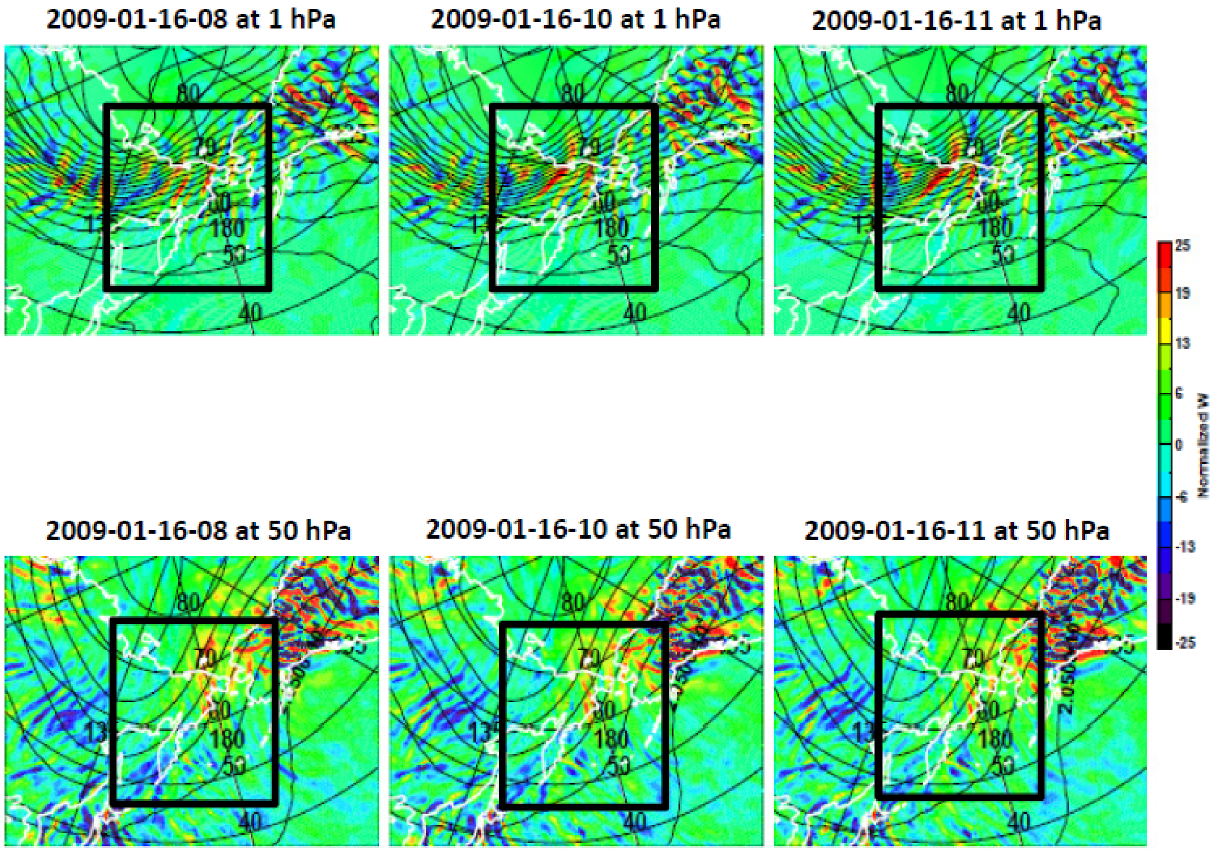

Figure 4.16: Time variations of vertical winds at (top) 1 hPa and (bottom) 50 hPa on January 16 at 8, 10, and 11 UT. Black line contours indicate geopotential height. White line represents continents. Black boxs identify gravity waves that are studied in this case study.

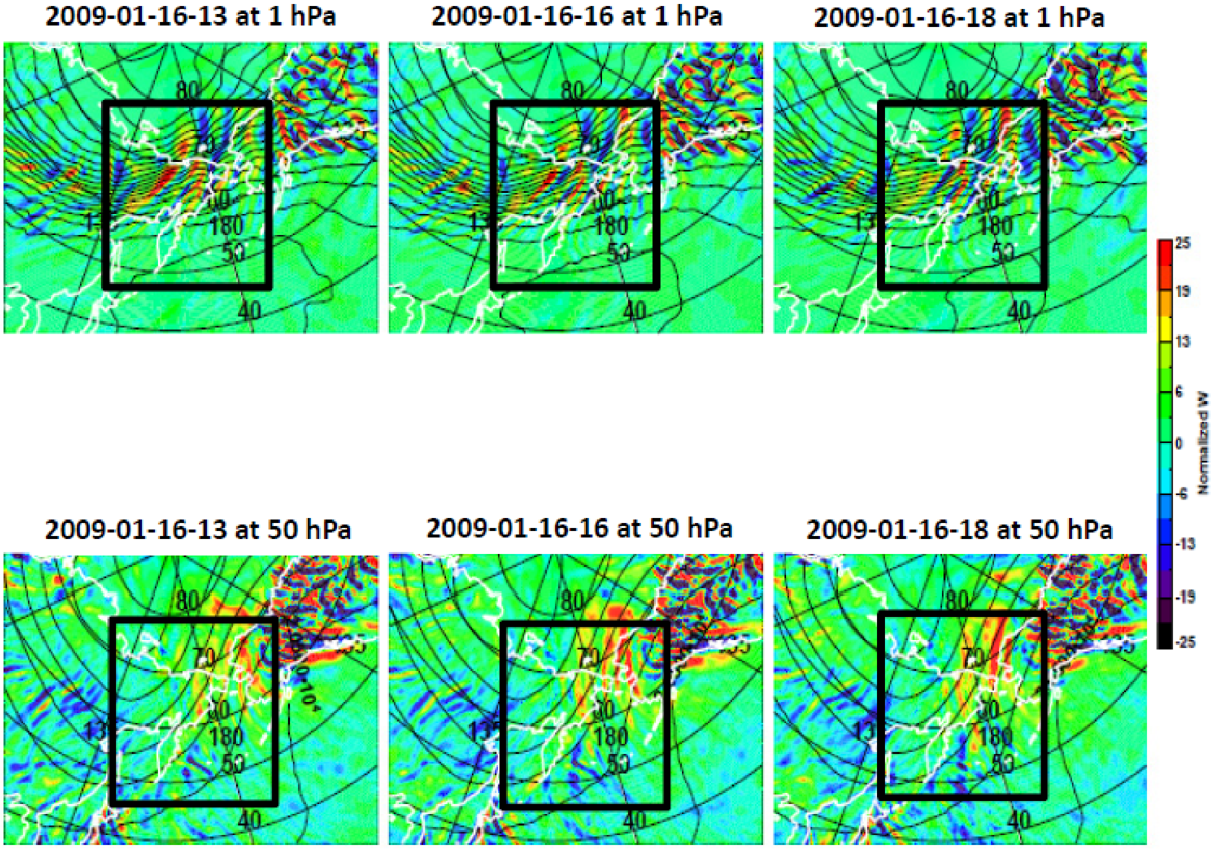

Figure 4.17: Same as Figure 4.16 on January 16 at 13, 16, and 18 UT.

Figure 4.18 illustrates the horizontal and vertical slices of gravity waves on January 16 at 14 UT and 18 UT. Gravity waves are again normalized by atmospheric density. Figures 4.18c–d display the vertical slices along the black lines in the horizontal plots in Figures 4.18a-b. In Figures 4.18c–d, gravity wave signatures appear in the middle of domain in the altitude range of 25–50 km, and there is no clear connection with the troposphere. Amplitudes are obviously larger in the upper stratosphere between 30 km and 50 km than amplitudes between 10 km and 25 km. In Figures 4.18e–h, the total energy fluxes and vertical fluxes of zonal momentum also display the maximums around 30–45 km and discontinuities from the troposphere. In addition to the vertical discontinuity, Figures 4.18e-h also exhibit horizontal discontinuities. The maximum momentum fluxes and total energy fluxes locate in the middle of each plot and suggest that these gravity waves are not resulting from horizontal or vertical propagation of gravity waves but in-situ generation.

Figure 4.19 shows the vertical slices of Fu and Fv along with the vertical wind perturbations at 14 and 18 UT. The locations of vertical slices in Figure 4.19 are the same as those in Figure 4.18. The large Fu and Fv are on the left side of gravity waves shown in Figure 4.19a–b. For this case, the background wind is blowing from the left side to the right side of each plot. Air parcels moving with the wind experience Fu and Fv. Hence, gravity waves are expected to be excited on the right side of Fu and Fv, as shown in top panels of Figure 4.19. The relative locations of gravity waves and large Fu and Fv strongly suggest that these gravity waves are generated by spontaneous response to the residual tendencies.

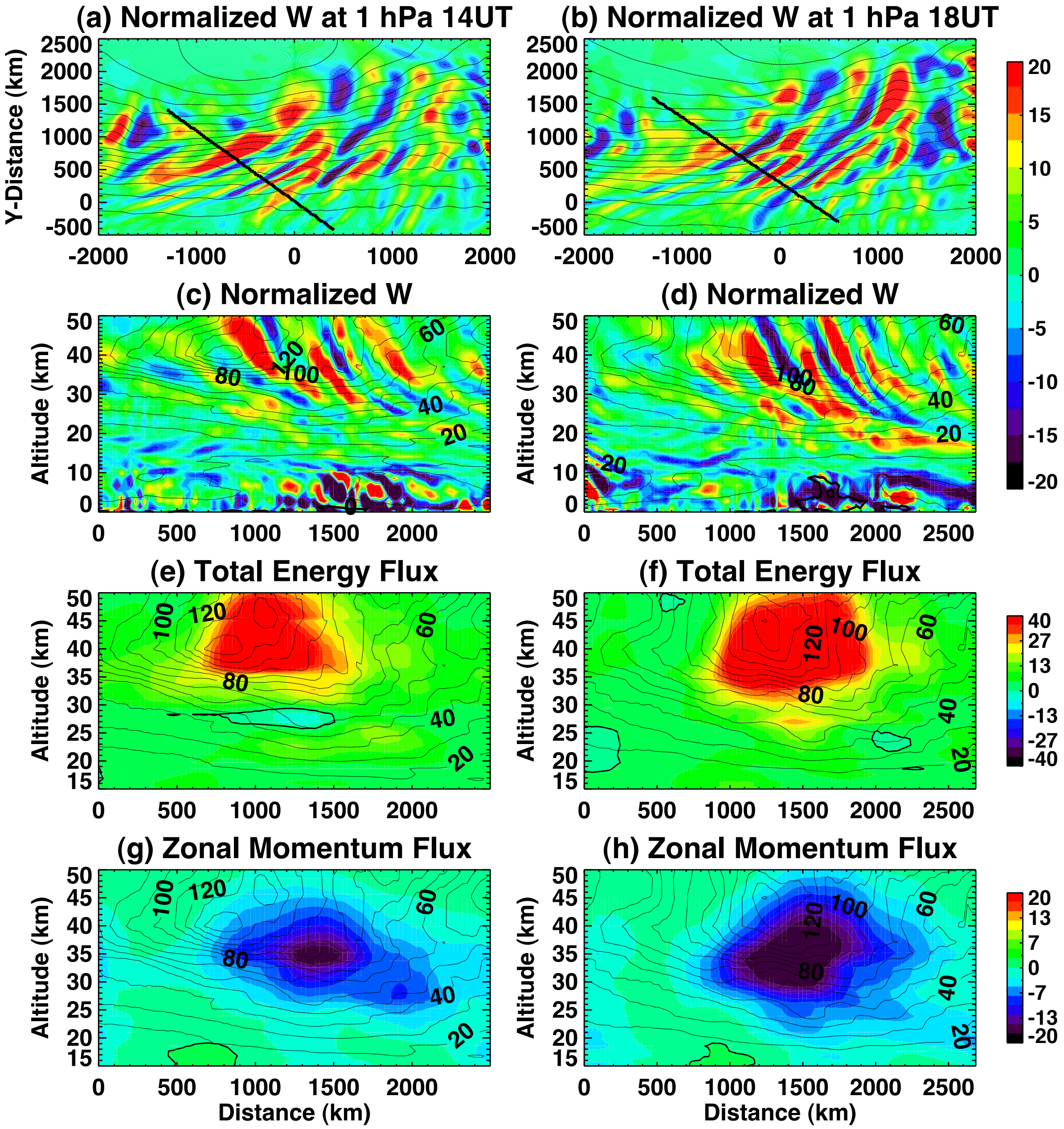

Figure 4.18: Vertical slices of gravity wave vertical wind, total energy flux, and vertical flux of zonal momentum flux on January 16 at (left) 14UT and (right) 18UT. Gravity waves are normalized by square root of atmospheric density. The momentum flux and total energy flux are multiplied by 10^3. Black line contours indicate (top) geopotential height, and (2nd, 3rd, and bottom) zonal wind.

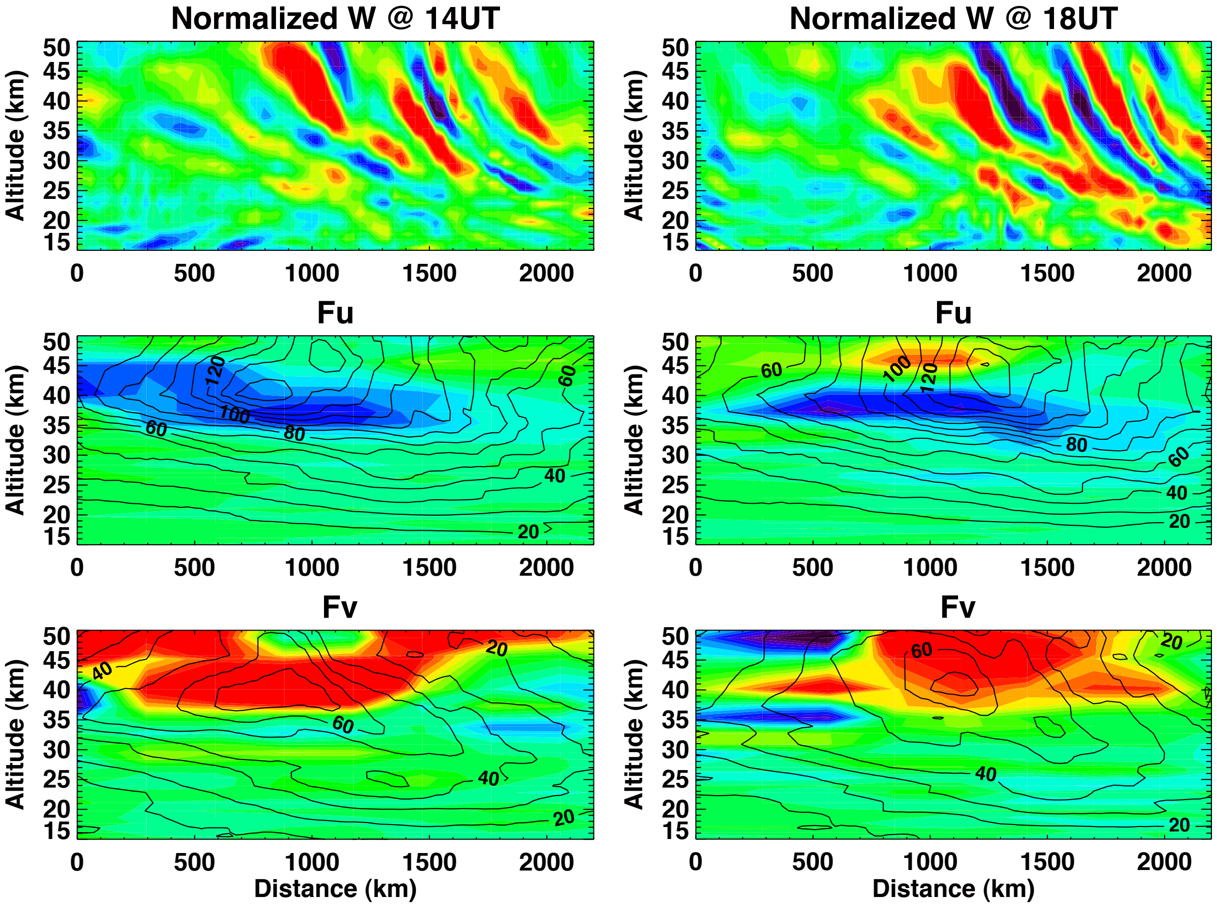

Figure 4.19: Vertical slices of (top) gravity wave vertical wind, (middle) Fu, and (bottom) Fv on January 16 at (left) 14 UT and (right) 18UT. Vertical winds are normalized by square root of atmospheric density. Black line contour represent (middle) zonal wind and (bottom) meridional wind.

Gravity Wave Characteristics

Now, the characteristics of gravity waves resolved in ECMWF shown in Figures 4.19 and 4.18 are estimated using the dispersion relation. The dispersion relation is:

$$\omega_i = \frac{N^2h^2 + f^2\left(m^2 + \frac{1}{4H^2}\right)}{h^2 + m^2 + \frac{1}{4H^2}} \tag{4.16}$$

where ω_i is intrinsic frequency, h is horizontal wavenumber, m is vertical wavenumber, H is scale height, and f is the Coriolis parameter [Fritts and Alexander, 2003].

From Figure 4.18 (one of the vertical and horizontal slices) on January 16 at 14 UT, the vertical wavelength is ∼10 km and the horizontal wavelength is ∼400 km. At this location, average N is ∼0.022 s^{-1} ($N^2 = \sim 0.00052\ s^{-2}$), and f is 1.3×10^{-4} s^{-1} at 65°N, and an average temperature is ∼218 K. Based on the dispersion relations, the intrinsic frequency is ∼5.8×10^{-4} s^{-1} and the period of ∼180 min. For the case on January 16 at 18 UT, the vertical wavelength is ∼8 km, the horizontal wavelength is ∼400 km, average N is ∼0.022 s^{-1} ($N^2 = \sim 0.00052\ s^{-2}$), and f is 1.3×10^{-4} s^{-1}, and an average temperature is ∼215 K. The estimated intrinsic frequency is ∼4.7×10^{-4} s^{-1} and the period of ∼221 min.

The ratio of intrinsic frequency, ω_i, to the Coriolis parameters, ω_i/f, is 4.4 on January 16 at 14 UT and 3.6 on January 16 at 18 UT. Previous simulations of gravity wave generation by spontaneous adjustment associated with the tropospheric jet steam showed ω_i/f of 3.7 [Zhang, 2004], 3.6 [Wang and Zhang, 2007], and 2.1 [Lin and Zhang, 2007]. Therefore, the gravity wave characteristics in this case study shown in Figure 4.18 are comparable with previous simulation results. Observed characteristics of gravity waves generated in-situ by the tropospheric jet were horizontal wavelength of 50–500 km and period of 1–4 hours (60-240 min) [Uccellini and Koch, 1987], which are well comparable with our results from ECMWF-T799.

Gravity wave characteristics are also estimated using the horizontal scale of Fu and Fv and wind speed. The period of gravity waves can be estimated by the durations of air parcel movements through Fu and Fv. The duration is estimated by the following simple equation:

$$Period \approx \frac{Distance}{Wind\ Speed} \tag{4.17}$$

The scales of Fu and Fv in Figure 4.19 are roughly 1000–1500 km. Wind speed along the vertical slices in the stratosphere is ∼80–120 m/s. Based on Equation 4.17 shown above, gravity waves excited by Fu and Fv are likely to have the following wave period:

$$Gravity\ \ Wave\ \ Period\ \ (h) = \frac{1000 - 1500\ \ km}{80 - 120\ \ m/s}\frac{1}{3600\ \ s} = 2.3 - 5.2\ \ hours \tag{4.18}$$

Gravity waves in this case study have wave period of ∼3–4 hours, consistent with gravity wave period estimated by the spatial scale of Fu and Fv and wind speed. The horizontal wavelengths of gravity waves studied here are ∼400 km from Figure 4.18. Comparing the previous simulation results, the dominated wavelengths were ∼150 km by idealized in-situ wave generation simulation by Zhang [2004], ∼70-100 km by Snyder et al. [2007,2009], and ∼300 km by Wang et al. [2009]. Our results are somewhat consistent with previous simulations.

4.3.3 Shear Instability

The shear instability is one of the possible causes of gravity wave variations. Limpasuvan et al. [2011] and Wang et al. [2006] showed the secondary generations of gravity waves by gravity wave breaking in the upper stratosphere during SSWs. In this study, the Richardson numbers calculated from the hourly ECMWF-T799 forecast output are always above 0.25 in the stratosphere where F_E increases, indicating the absence of shear instability. The non-modeled gravity wave growth from shear flow with the large Richardson numbers are discussed by Bakas and Farrell [2007], and this possibility needs to be investigated in the future.

4.4 Conclusions

The physical mechanisms causing gravity wave variations during the 2009 SSW are investigated with the ECMWF-T799 and the GROGRAT ray-tracing model. The variations of GW-Ep variations during the 2009 SSW exhibit two peaks prior to the wind reversal and a minimum after the wind reversal. Two peaks of gravity wave enhancements cannot be explained by the changes in either orographic or nonorographic gravity wave propagations from the polar troposphere or gravity wave propagation from the tropics. Instead, the two-peaks of GW-Ep correlate well with the increases of in-situ energy sources suggested by the height variations of total perturbation energy flux (F_E). In ECMWF-T799, the Richardson numbers are always above 0.25 in the stratosphere, indicating that the shear instability is not the causes of energy increase in this case. The spatial and temporal variations of in-situ energy source and also GW-Ep correspond to those of the residual tendencies introduced by Snyder et al. [2007, 2009] that can excite gravity waves in-situ in the stratosphere. Therefore, this study reveals that two peaks of gravity wave enhancements are most likely caused by the increases of the in-situ gravity wave excitations through spontaneous responses to the residual tendencies.

The sudden decay of gravity wave activities correlates well with the variations of probabilities of gravity wave propagations from the troposphere to the stratosphere obtained from the GROGRAT ray-tracing model. In addition, residual tendencies decay after January 25. These results indicate that decay of gravity waves after wind reversal is likely due to the changes of gravity wave propagations along with the reduction of in-situ gravity wave sources.

In this study, ECMWF-T799 indicates that the increases of the in-situ gravity wave excitations are responsible for the gravity wave enhancements prior to the 2009 SSW. However, it is possible that the changes in gravity wave propagation can be more important for other cases. For example, Wang and Alexander [2008] concluded that the enhancements of gravity wave temperature variances were caused by the changes in gravity wave propagation but not by in-situ gravity wave excitations for the 2008 SSW. The 2008 SSW consisted of several minor SSWs and was weaker than the 2009 SSW. The 2008 SSW is caused by the enhancements of planetary wave 1, but the 2009 SSW is due to the planetary wave 2 with the polar vortex split. These differences in types or magnitudes of SSWs might alter the physical mechanisms that are responsible for the gravity wave variations.

Chapter 5

Sensitivity Study of the MLT Temperature Responses to Gravity Wave Forcing during SSWs

In this chapter, the responses of MLT temperatures to gravity wave forcing are examined. In particular, this chapter focuses on the characteristics of temperature anomalies and their downward progression from the mesosphere to the stratosphere using TIME-GCM.

5.1 Introduction

Stratospheric sudden warmings (SSWs) have global influences on the atmospheric circulations from the troposphere to the thermosphere [e.g., Mastuno, 1971; Labitzke, 1972; Liu and Roble, 2002; Yamashita et al. 2010]. Sudden enhancement of planetary waves and their interactions with the mean flow are widely accepted as the cause of SSWs [Matsuno, 1971]. Associated with SSWs, cooling in the mesosphere and warming in the lower thermosphere have been observed [e.g., Labitzke, 1972; Siskind et al., 2005; Coy et al., 2005]. The first observation of the cooling in the mesosphere was reported by Labitzke [1971] using Satellite Infrared Spectrometer, Selective Chopper Radiometwer, and Rocketsondes data. Following observations by Labitzke [1971], Whiteway and Carswell [1994] showed the stratospheric warming and mesospheric cooling by Rayleigh lidar observations. Waltersheid et al. [2000] presented their observed cooling by OH airglow temperature measurements. Hoffmann et al. [2007] used the temperature and wind measurements from meteor radars at Resolute Bay (75°N, 95°W), Andenes (69°N, 16°E) and Khlungsborn (54°N, 12°E) to show the mesospheric cooling by ∼10K associated with SSW. In addition to the ground-based observations, the cooling and warming in the mesosphere and the lower thermosphere (MLT) were also observed by SABER satellite observations [Siskind et al., 2005].

These MLT temperature changes associated with SSWs are simulated by the TIME-GCM, the Navy-Operational Global Atmospheric Prediction System - Advanced Level Physics and High Altitude (NOGAPS-ALPHA), and the Canadian Middle Atmosphere Model Data Assimilation System (CMAM-DAS) [Liu and Roble, 2002; Coy et al., 2005; Ren et al., 2008]. Based on numerical modeling studies, the changes in filtering of gravity waves due to wind reversal are most likely responsible for the MLT temperature anomalies [Holton, 1983; Liu and Roble, 2002]. The importance of gravity wave forcing for capturing mesospheric cooling has also been examined using the NOGAPS-ALPHA model with and without the Rayleigh friction and the CMAM-DAS model with and without a non-orographic gravity wave parameterization [Coy et al., 2005; Ren et al., 2008]. In general, simulations with gravity waves considered gave more realistic results than without the parameterization in the MLT region.

TIME-GCM has been able to capture some of above SSW signatures, though discrepancies between TIME-GCM simulations and observations still exist and vary from event to event [Siskind et al., 2005; Coy et al., 2005; Liu and Roble, 2005]. Figure 5.1 shows the comparisons between the SABER (version of 1.07) observation and TIME-GCM simulation with typical gravity wave parameters for the 2008 SSW. The setup of typical gravity wave parameters is summarized in Table 1 as the base case. Minor and major warmings were observed in the NH in 2008. The episode of the minor SSW event from January 18 to January 29 is shown here. In Figure 5.1, the color contours are the zonal mean temperature changes during this SSW event. TIME-GCM captures the general features of these observed temperature changes including the stratospheric warming, the mesospheric cooling, and the thermospheric warming. However, TIME-GCM simulations do not reproduce the detailed observed features. These discrepancies lie in two major categories: (1) the characteristics of cooling and warming regions in the MLT: the lower thermospheric warming in TIME-GCM is significantly stronger than in SABER, while the height and vertical depth of the simulated mesospheric cooling are higher and narrower, respectively, than observed by SABER and (2) the downward trend of temperature anomaly from the mesosphere to the stratosphere: the downward progression of temperature from ∼60 km to ∼35 km was clearly observed by SABER but not obvious in TIME-GCM. In contrast to the 2008 SSW simulation, the mesospheric cooling region in SABER observations for the 2002 Southern Hemisphere SSW is narrower than in TIME-GCM simulations [Coy et al., 2005; Liu and Roble., 2002].

Both MLT temperature characteristics and downward progressions can be tied to gravity waves because of the crucial role of gravity wave forcing in MLT dynamics. It is thus necessary to systematically quantify the dependence of the MLT temperature responses to SSWs on the gravity wave parameters, which is the primary goal of this work. In addition, the role of planetary

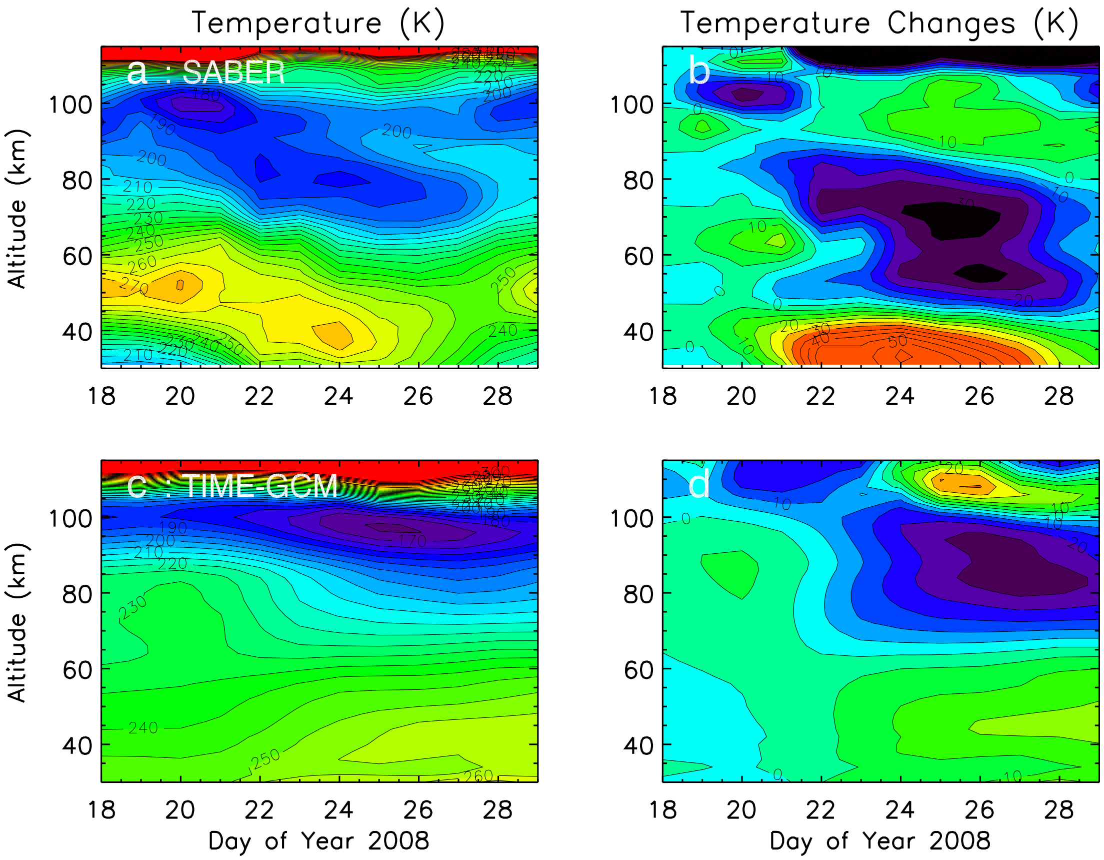

Figure 5.1: Temperature and temperature changes from day 18 during the 2008 SSW. (a,b) SABER observations (version 1.07) at 80°N 2.5° from January 18 to 29. The peak SSW is observed around day 24. (c,d) TIME-GCM simulation with typical gravity wave parameters (case 2 in Table 1) at 81.25°N.

waves generated in-situ by gravity wave forcings in the MLT is examined. The generation of these planetary waves was discussed by Smith [1996], but their roles in the MLT temperature responses to SSWs have not been fully examined. The numerical tool used for this study is the NCAR TIME-GCM, which has a unique advantage of an upper boundary at ∼500 km, thus the capability of simulating thermospheric effects. It should be noted that the main purpose of the current study is not to reproduce the exact observed features. Rather, the focus is to study how the MLT temperature responses to different gravity wave parameters in TIME-GCM during SSWs.

5.2 TIME-GCM

The TIME-GCM developed at the NCAR is used for this study. The horizontal resolution is 2.5° × 2.5° (latitude × longitude), and the vertical resolution is four grid points per scale height. The lower boundary is specified by the ECMWF data at 10 hPa every 6 hours, and the model domain is from 10 hPa to ∼500 km with 89 vertical levels. Detailed descriptions of TIME-GCM are provided in Roble and Ridley [1994] and Liu and Roble [2002] and references therein. TIME-GCM employs a gravity wave parameterization based on the liner saturation theory [Lindzen, 1981; Holton, 1982; Garcia and Solomon, 1985; Fritts, 1984]. Gravity wave parameters are typically specified at the lower boundary of model domain. Figure 5.2 shows the input gravity wave parameters and output gravity wave forcing from this parameterization scheme. As shown in the left side of Figure 5.2, a Gaussian shape of discrete spectrum is used to define the gravity wave parameters. The horizontal wavelength, spectral width, numbers of waves, spectral peak shift, and initial momentum flux can be specified in the model. Incorporating the setup of input parameters and winds and temperatures from TIME-GCM, the gravity wave parameterization scheme calculates gravity wave forcing and breaking altitude. These calculated gravity wave forcing outputs are then transferred to TIME-GCM.

For the TIME-GCM simulations used here, the gravity wave input is specified at 10 hPa with a discrete spectrum (15 m/s interval) in a Gaussian shape with a fixed horizontal wavelength. The spectral width (defined as the range of phase velocity), horizontal wavelength, and wave amplitude

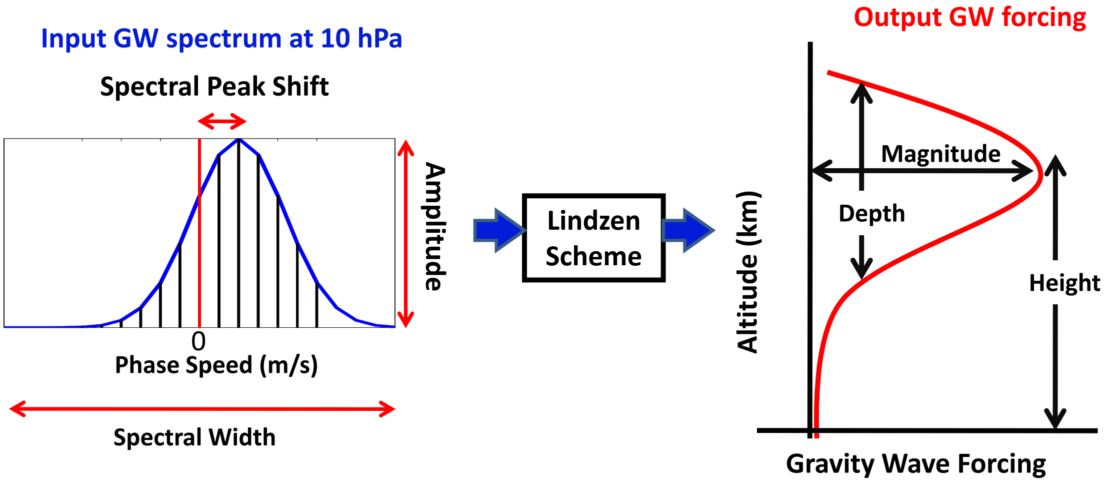

Figure 5.2: Schematics of input to and output from gravity wave parameterization scheme.

are varied in the parameterization scheme, and the parameters used in this study are summarized in Table 5.1. Here the same Gaussian function is used for describing the spectral shape, while the spectral width is adjusted between ±30 m/s and ±90 m/s. In all cases of simulations, we vary gravity wave parameters only from 0° to 90°N while keeping the base case parameters for 0° to 90°S. This study aims to investigate (1) how the magnitude, height, and depth of gravity wave forcing are controlled by the input gravity wave parameters, and (2) how the MLT temperatures respond to the changes in gravity wave forcings.

Table 5.1: Gravity wave parameters used in TIME-GCM simulations

	Range of Phase Velocities (Spectral Width)	Horizontal Wavelength	Momentum Flux
Base Case	-90 to 90 m/s	100 km	$\sim 10^{-4}$ Pa
Case 1	-30 to 30 m/s	100 km	$\sim 10^{-4}$ Pa
Case 2	-90 to 90 m/s	1000 km	$\sim 10^{-5}$ Pa
Modified Case	-60 to 60 m/s	1000 km	$\sim 10^{-4}$ Pa

5.3 Responses of the MLT Temperatures to Gravity Wave Forcing during Stratospheric Sudden Warming

5.3.1 Profile Study using Gravity Wave Parameterization Scheme

We examine how gravity wave forcings vary with different gravity wave parameters input to the parameterization scheme. Figures 5.3a and 5.3b show forcings generated by gravity waves with different spectral widths and horizontal wavelengths using the wind profile plotted in Figure 5.3c during a SSW at high latitudes. In Figure 5.3a, the gravity wave forcing region expands upward by ~15 km when the spectral width is increased from ±30 m/s to ±90 m/s with a constant horizontal wavelength of 100 km. This upward expansion is caused by faster gravity waves propagating and breaking at higher altitudes. The magnitude of total gravity wave forcing also increases with the wider spectral width as more wave components are introduced. In Figure 5.3b, the horizontal wavelength of input gravity waves is varied from 1000 km to 10 km with a constant spectral width of ±90 m/s. As the horizontal wavelength decreases, gravity wave forcing becomes stronger, the forcing region expands, and the altitude of the maximum GW forcing increases. This is because the dispersion relations dictate that for a fixed phase speed, gravity waves with shorter horizontal wavelengths have higher frequencies and longer vertical wavelengths, and these waves can propagate to higher altitudes [Holton, 1983]. No strong forcing is observed above the height of ~100 km in the 1000 km case (Figure 5.3b) as the breaking altitudes of these waves are lower than other cases.

5.3.2 Temperature Anomaly in TIME-GCM

Equipped with the understanding from section 5.3.1, we now examine how the MLT cooling and warming regions respond to gravity wave forcings in TIME-GCM. Figures 5.4a-5.4d show TIME-GCM simulations for 4 different cases: A case without gravity wave parameterization and three cases with gravity waves as listed in Table 1. Compared with the base case, case 1 uses the narrower spectral width and case 2 uses the longer horizontal wavelength and larger amplitude gravity waves. In Figure 5.4a for the case without the gravity wave parameterization, no warming

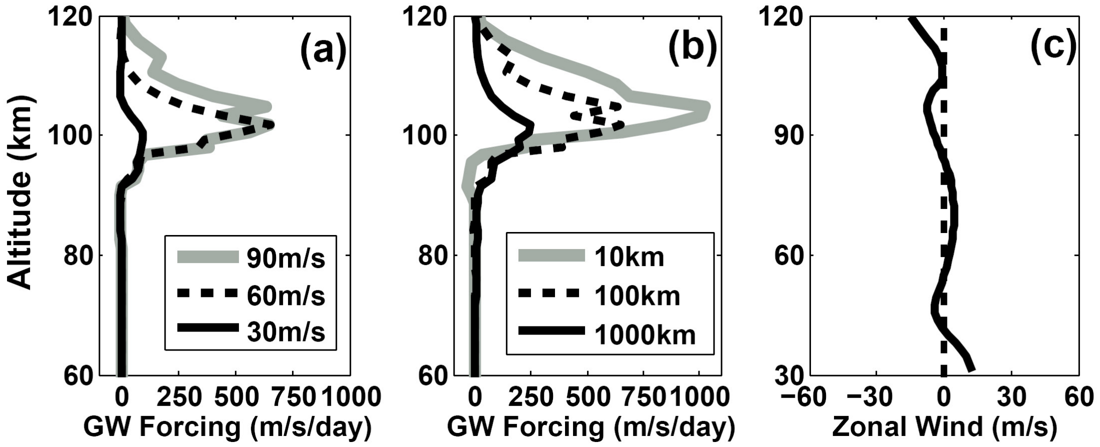

Figure 5.3: Gravity wave forcing output from the gravity wave parameterization. (a,b) gravity wave forcing calculated under the zonal wind condition shown in (c). (a) varying spectral range of ±90 m/s (thick gray), ±60 m/s (dash), and ±30 m/s (black solid) with a constant horizontal wavelength of 100 km, (b) setting the horizontal wavelength to 10 km (thick gray), 100 km (dash), and 1000 km (black solid) with a constant spectral range of ±90 m/s.

occurs in the lower thermosphere but there are ∼17 K stratospheric warming and ∼10 K mesospheric cooling. Compared to Figure 5.4a (No gravity waves), the base case (Figure 5.4b) gives a similar magnitude of stratospheric warming, but much stronger cooling (∼30 K) in the mesosphere and warming (∼29 K) in the lower thermosphere. In case 1 (Figure 5.4c), the mesospheric cooling and lower thermospheric warming are weaker by ∼4 K and ∼22 K, respectively, than the base case. Case 2 (Figure 5.4d) has the height and magnitude of the mesospheric cooling region to be ∼10 km lower and ∼9 K weaker, respectively, than the base case. In case 2, gravity waves break at lower altitudes, thereby damping planetary waves in the breaking region. This prevents the planetary waves from growing to larger amplitudes thus resulting in a weaker, lower, and narrower warming region below 70 km compared to the base case. Although gravity waves have some influence on the characteristics of warming below 70 km, the stratospheric warming below 70 km and stratospheric jet reversal (not shown) occur in all cases of TIME-GCM simulations with and without gravity wave parameterization, confirming that planetary waves are the main driver of SSWs [Matsuno,1971]. Nevertheless, the magnitude, height, and vertical depth of the cooling and warming regions in the MLT vary significantly with different gravity wave forcings.

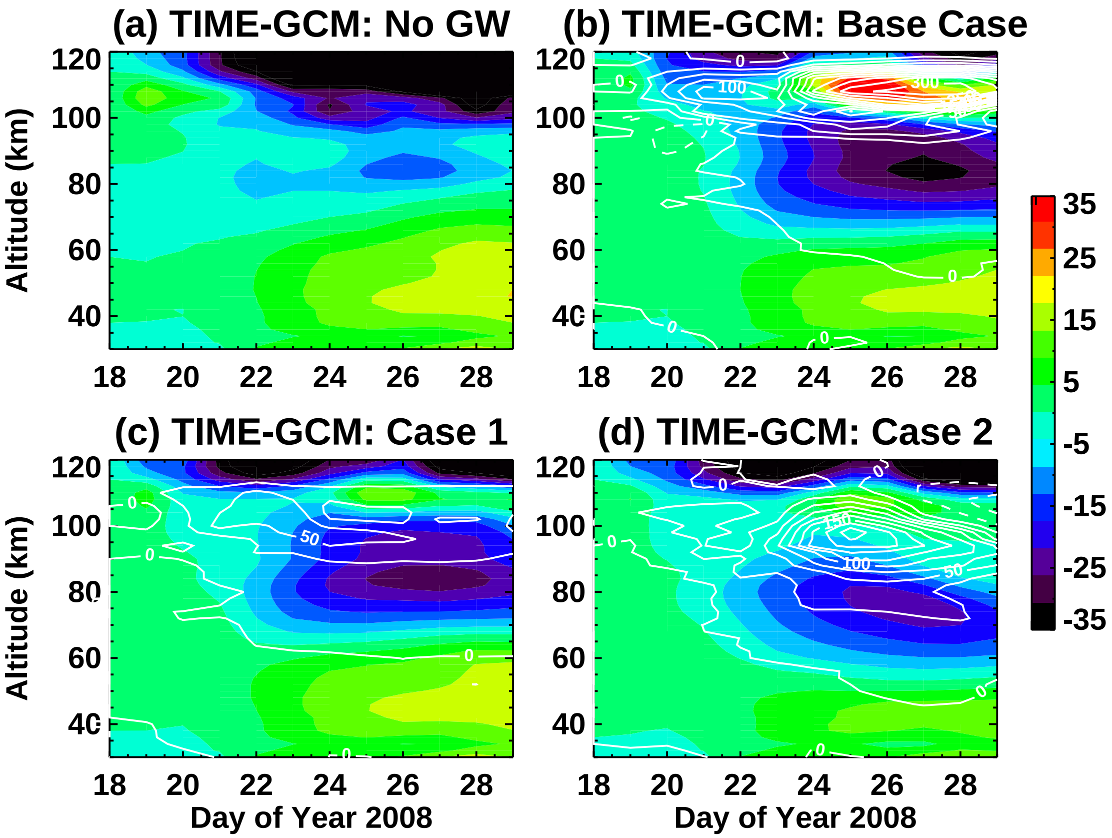

Figure 5.4: TIME-GCM simulations at 81.25°N with different gravity wave parameters (a) no gravity wave parameterization, (b) base case, (c) case 1, and (d) case 2. Color contours show the zonal mean temperature changes (K) at 12UT after day 18, 2008. Line contours show the zonal mean gravity wave forcing changes (m/s/day) at 12UT. Solid/dash line represents the eastward/westward forcing, respectively.

5.3.3 Residual Circulation Induced by Gravity Wave and Planetary Wave Forcings

The changes of gravity wave forcing during this SSW relative to January 18 are over-plotted as white line contours on Figures 5.4a-d. The vertical depth of gravity wave forcing regions is wider in the base case than in case 1, because the base case uses the wider range of gravity wave spectrum. Moreover, the height of gravity wave forcing regions is lower in case 2 than the base case due to the longer horizontal wavelength and lager amplitude gravity waves used in case 2. These results are consistent with the trend shown in section 5.3.1 and the results presented by Holton [1983].

Now we investigate the mechanisms how gravity wave forcing affects the height, vertical depth, and magnitude of the cooling and warming regions in the MLT. The lower thermospheric warming and the mesospheric cooling occur above and below the peak eastward forcing region, respectively in Figures 5.4c–d. Compared to Figure 5.4b, the heights of gravity wave forcings in Figure 5.4d are lower by ∼10 km, and the heights of the cooling and warming regions are also lower by ∼10 km. The magnitude of warming at 100–120 km and cooling at 70–100 km in the base case is much stronger than those in case 1 and case 2, because the larger changes of eastward gravity wave forcing in the base case induce stronger upward/downward circulation in the MLT than in other cases. The vertical depth of the cooling regions in case 2 is larger than in case 1 as eastward gravity wave forcing region is wider in case 2. Therefore the height, vertical depth, and magnitude of the MLT cooling and warming regions generally agree with the characteristics of gravity wave forcings regions. However, the following exceptions are noted. First, the magnitudes of gravity wave forcing changes are larger in case 2 than case 1 (Figures 5.4c and 5.4d), which should induce stronger downward/upward circulation between 60-120 km thus larger temperature response in case 2, but such response is not seen in Figures 5.4c and 5.4d. This may be partly due to the larger air density at lower breaking levels in case 2. Second, although the vertical depth of gravity wave forcing in the base case between January 24 and 28 above 80 km is wider than that in case 1 (Figures 5.4b and 5.4c), the overall vertical depths of the mesospheric cooling regions above 65 km are comparable in the two cases. These discrepancies cannot be explained by gravity wave forcing alone but by the combinations of gravity wave forcing and planetary wave forcing in the MLT.

In order to further investigate the physical mechanisms of differences among cases, the residual circulations and Eliassen-Palm (EP) flux are calculated based on the transformed Eulerian-Mean equations (TEM) [Andrews et al., 1987]. A residual mean meridional circulation ($\overline{v*}, \overline{w*}$) are defined as:

$$\overline{v*} = \overline{v} - \frac{1}{\rho_0}\left(\frac{\rho_0 \overline{v'\theta'}}{\overline{\theta}_z}\right)_z \tag{5.1}$$

$$\overline{w*} = \overline{w} + \frac{1}{acos\phi}\left(\frac{cos\phi \overline{v'\theta'}}{\overline{\theta}_z}\right)_\phi \tag{5.2}$$

EP flux, $F = (F_\phi, F_z)$, is defined as:

$$F_\phi = \rho_0 acos\phi \left(\frac{\overline{u}_z \overline{v'\theta'}}{\overline{\theta}_z} - \overline{v'u'}\right) \tag{5.3}$$

$$F_z = \rho_0 acos\phi \left\{\left[f - \frac{1}{acos\phi}\left(\overline{u}cos\phi\right)_\phi\right] \frac{\overline{v'\theta'}}{\overline{\theta}_z} - \overline{w'u'}\right\} \tag{5.4}$$

The divergence of EP flux are derived as:

$$\nabla \cdot F = \frac{1}{acos\phi}\frac{\partial F_\phi cos\phi}{\partial \phi} + \frac{\partial F_z}{\partial z} \tag{5.5}$$

where $\overline{v}$ and $\overline{w}$ are zonal-mean meridional wind and vertical wind, respectively, v', w', and θ' are deviations from the zonal mean of meridional wind, vertical wind, and potential temperature. ϕ is latitude, ρ is atmospheric density, and a is the earth radius.

Figure 5.5 shows the temperature anomalies along with vector plots of the changes of residual circulation (a–c), the changes of parameterized gravity wave forcing (d–f), the changes of resolved planetary wave forcing (the Eliassen-Palm flux divergence) (g–i), and the resolved planetary wave perturbations in the zonal wind field (j–l). Here, the changes of gravity wave and planetary wave forcing and residual circulation are the differences between January 18 (before SSW) and January 25 (during SSW). The changes of residual circulation in Figures 5.5a–c are driven by the Coriolis forces (shown as black arrows in Figures 5.5d–i) induced by the changes of gravity wave and planetary

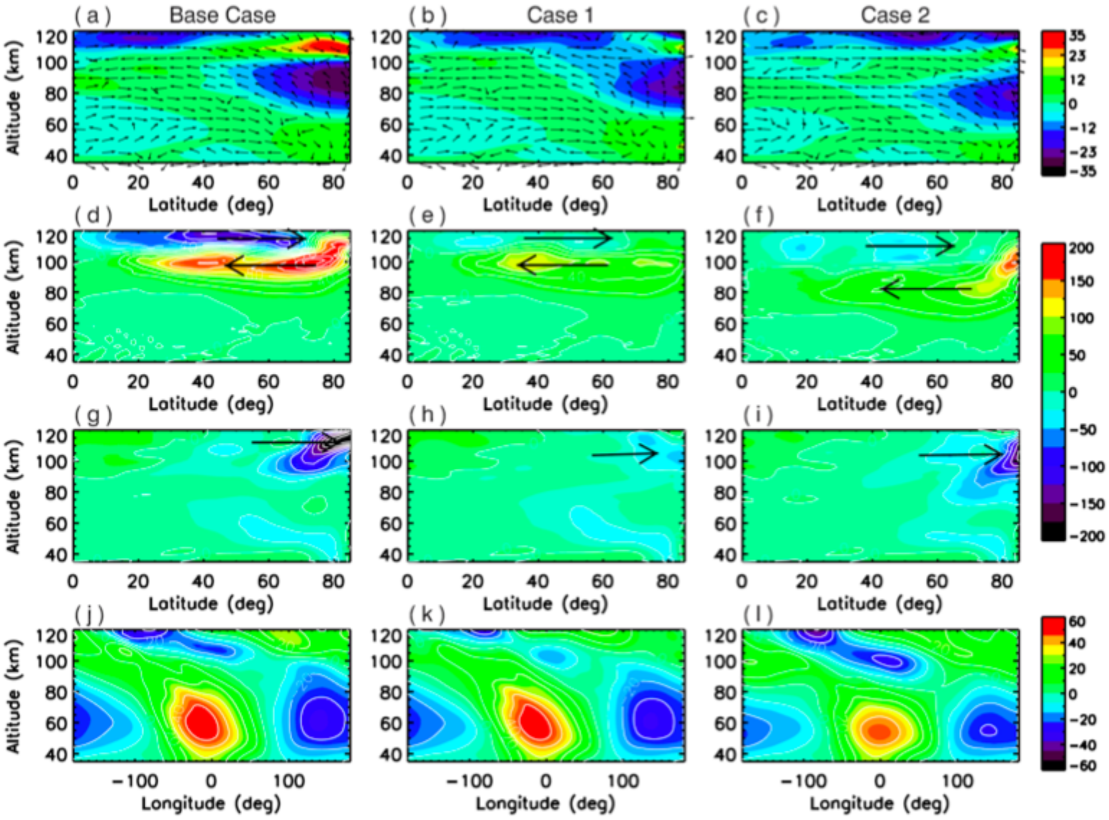

Figure 5.5: The zonal-mean (top; a,b,c) temperature changes from January 18 over-plotted with residual circulation changes, (2nd column; d,e,f) parameterized gravity wave forcing changes (m/s/day), (3rd column; g,h,i) resolved planetary wave forcing changes (m/s/day), and (bottom; j,k,l) planetary scale perturbation on zonal wind (m/s) at 64°N on January 25 for three different cases (left: base case, middle: case 1, and right: case 2). The residual circulation vectors are normalized. Black arrows (in d-i) represent Coriolis force induced by the corresponding forcing changes. Negative/positive value represents the westward/eastward forcing and zonal wind.

wave forcing. As clearly seen in Figures 5.5a-c, the locations of cooling and warming of temperature anomalies correspond well with the changes of the upward and downward circulation, respectively.

Compared with case 1, eastward gravity wave forcing in case 2 locates at lower heights at middle latitudes but at similar heights at high latitudes (Figures 5.5e and f). We also notice that the high-latitude gravity wave forcing in case 2 is much stronger than that in case 1. In the meantime, westward planetary wave forcing in case 2 is significantly larger than that in case 1 (Figures 5.5h and i). The westward planetary wave forcing in case 2 overlaps with eastward gravity wave forcing at high latitudes. Thus, the planetary wave forcing cancels the gravity wave forcing in case 2, leading to the MLT temperature anomalies at high latitudes comparable to case 1. This explains the first exception mentioned above.

The second exception, i.e., discrepancy in the vertical depth of the mesospheric cooling region in the base case and in case 1, is explained by the differences in downward flow at 100–120 km. In Figures 5.5d, e, g, and h, poleward circulation induced by combinations of westward gravity wave and westward planetary wave forcing between 100–120 km are larger in the base case than in case 1, leading to the stronger downward flow at 100–120 km in the base case. Such enhanced downward flow at 100–120 km erodes the region with upward flow induced by eastward gravity wave forcing. In other words, the region of upward flow in the base case is shrunk by the strong downward flow above it. Thus, the vertical depth of cooling at 70–100 km in the base case is similar to that in case 1, even though the vertical depths of gravity wave forcing regions are wider in the base case.

The origin of planetary wave in MLT is an interesting question. The planetary wave forcings in Figures 5.5g–i appear to be correlated with gravity wave forcings in Figures 5.5d–f. Both planetary wave and gravity wave forcing changes at high latitudes are over 150 m/s/day in the base case, but less than 50 m/s/day in case 1. Both planetary wave and gravity wave forcing regions are ∼10 km lower in case 2 than in the base case. Smith [1996] suggests that the planetary-scale disturbances are generated in-situ by longitudinal variations of gravity wave forcing in the mesosphere due to the gravity wave filtering by planetary waves in the stratosphere. According to Smith [1996], if planetary waves in Figures 5.5g–i are generated in-situ by the mesospheric gravity wave forcing, the phases of planetary waves in the stratosphere and above the mesosphere are expected to be 180 degrees out of phase. Figures 5.5j–l show the planetary scale perturbations on the zonal wind field, and the phases of planetary waves above 100 km are ∼180 degrees out of phase from those below 100 km for all the cases. Thus, our study indicates that planetary waves contributing to the simulated MLT temperature anomalies are generated in-situ by gravity wave forcing during the SSW.

5.4 Roles of Gravity Waves in Downward Progression of Temperature Anomaly

This section discusses the influences of gravity wave parameters on downward progression of temperature anomaly observed during SSWs. Shown in Figure 5.6a is a time-altitude contour of zonal mean SABER temperature in January 2008 averaged over the latitude range of 77.5° and 82.5°. Clear downward progression of warm temperature anomaly is observed from ∼60 km to ∼40 km. On the other hand, the TIME-GCM base case simulation with typical gravity wave parameters in Figure 5.6b does not show clear downward progression, though it shows some warming in the stratosphere. Figure 5.6c displays the TIME-GCM simulation with modified parameters. This modified setup of gravity wave parameters is summarized in Table 5.1 as modified case. These modified parameters are determined to simulate the temperature anomaly better compared to the SABER observations based on the knowledge obtained in the previous section. The modified parameters use longer horizontal wavelength and narrower horizontal phase speed than the base case. The reason of this modification is that the height of cooling and warming regions are too high in TIME-GCM base case than SABER as can be seen in Figure 5.1. By increasing the horizontal wavelength, gravity waves break in the lower altitudes, resulting in the lower cooling region. The magnitudes of warming in the lower thermosphere are too strong in the base case, and thus the spectral width is reduced to decrease gravity wave forcing at the higher altitudes. Comparing Figures 5.6b with 5.6c, the downward propagation of temperature anomaly becomes much clearer in the modified case. The only difference between these TIME-GCM simulations is the setup of gravity wave parameters, indicating the effects of gravity wave spectra on the downward progression of temperature anomalies from the mesosphere to the stratosphere.

The TIME-GCM simulation has been improved with the modified gravity wave parameters; however, the downward propagation and warming in the stratosphere in TIME-GCM simulations are still quite weak compared to SABER observations. Figure 5.6d shows the simulation results by the NCAR Whole Atmosphere Community Climate Model (WACCM). WACCM is the 3D self-consistent model from the ground to the thermosphere. Detailed descriptions of WACCM can be found in Garcia et al. [2007]. Because WACCM is a self-consistent model, this simulated SSW is not the same SSW event as observed by SABER and simulated by TIME-GCM. However, WACCM captures both the downward progression and the reasonable magnitude of warming in the stratosphere as observed by SABER. This WACCM simulation is thus used to diagnose the causes of downward propagations.

Comparing two TIME-GCM simulations in Figures 5.6b-c, one of the main differences is the height of the zero-wind line of zonal mean zonal wind shown as white thick line in Figures 5.6b-c. The zero-wind lines are ∼115 km in the base case and ∼90 km in the modified case on January 18 during the SSW onset. The height difference of ∼25 km between two TIME-GCM simulation is induced by the different gravity wave parameters. Furthermore, the zero-wind line in WACCM simulation is much lower than in the TIME-GCM modified case. The zero-wind line in WACCM is ∼70 km when temperature anomaly starts propagating downward, which is ∼20 km lower than that in the TIME-GCM modified case. The zero-wind line is a critical layer for stationary planetary waves. As a result, we hypothesize that planetary waves and the height of the zero-wind line may be responsible for the weaker downward progression in TIME-GCM.

To further examine this hypothesis, we plot the amplitude of the zonal wave number 1 component of the geopotential height perturbations (PW1) in Figure 5.7. Wavenumber 1 is the dominant components in the above simulations. Figure 5.7a shows PW1 with no gravity wave parameters. In this case, PW1 propagates up to the lower thermosphere. The zero-wind line for PW1 is too high to filter PW1 in the lower altitude and there is no gravity wave to damp PW1.

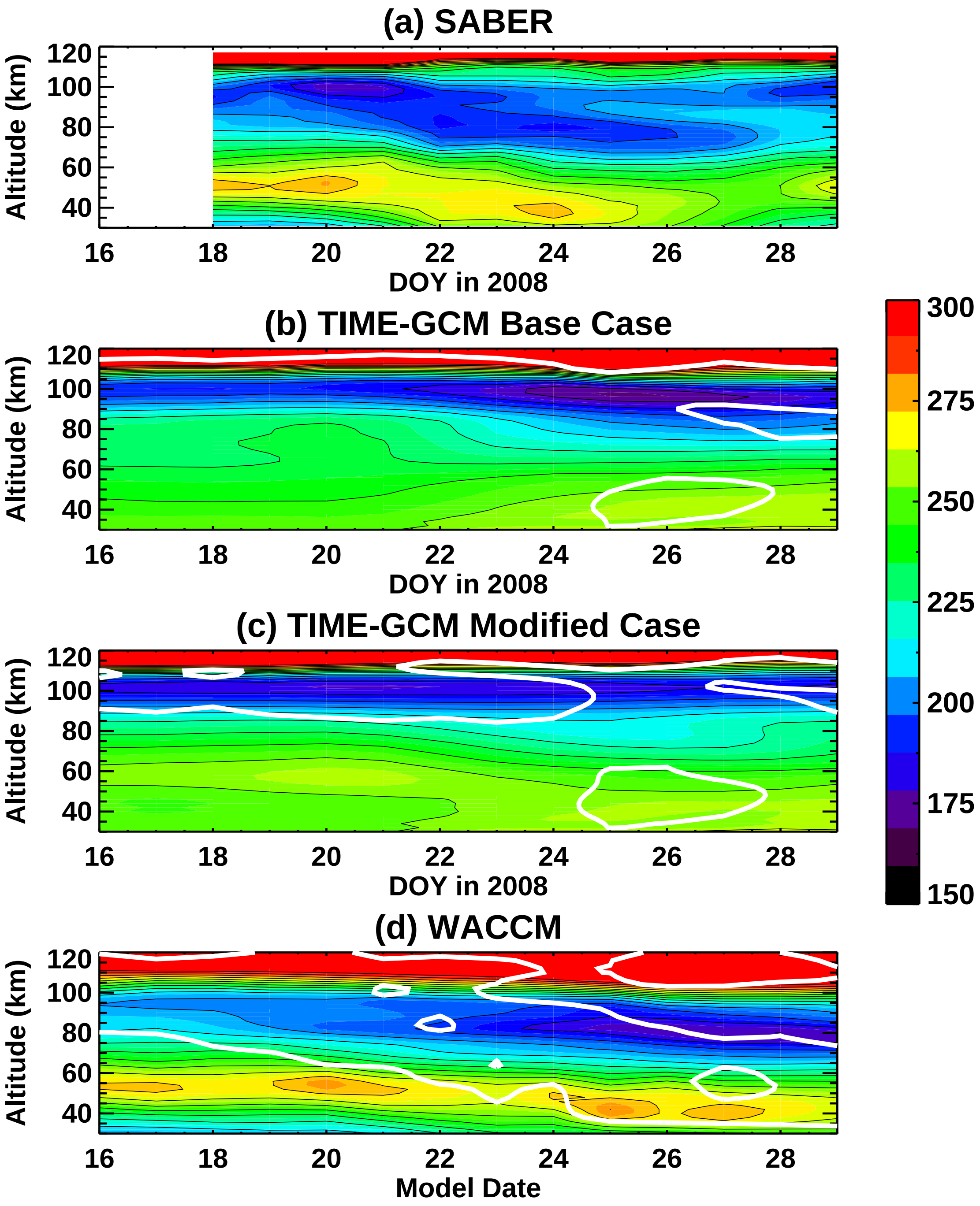

Figure 5.6: Zonal mean temperature around 80°N from (a) SABER observations, (b) TIME-GCM base case, (c) TIME-GCM modified case, (d) WACCM. White thick lines represent the zero-wind lines of zonal mean zonal wind during the 2008 SSW.

Figure 5.7b shows PW1 in the base case. Although the zero-wind line in the base case is as high as that in no gravity wave case, PW1 is weaker above ∼80 km in the base case. This probably results from damping of PW1 by gravity wave breaking in the base case. In modified case, PW1 decays above ∼55 km. The zero-wind line height is lowered down due to the lower height of gravity wave breaking than in the base case. At the same time, gravity wave forcing is increased in the lower altitude (∼50–80 km), leading to the damping of PW1 in this region. Finally, Figure 5.7d shows PW1 simulated by WACCM. In this case, PW1 shows the peak amplitude slightly below the zero-wind line, and the amplitude of PW1 is significantly decaying above the zero-wind line. PW1 in WACCM is likely controlled by the zero-wind line but not damped by gravity wave forcings. These TIME-GCM and WACCM simulations indicate that both the height of zero-wind line and gravity wave forcings control planetary waves.

Although both WACCM and TIME-GCM employ a gravity wave parameterization scheme based on the linear saturation theory [Lindzen, 1981], WACCM shows the better SSW simulation than TIME-GCM. WACCM simulation shown here does not include the physically based gravity wave source variations [Richter et al., 2010]. One of the main differences between WACCM and TIME-GCM in terms of gravity waves is the launching altitude of gravity waves. In WACCM, gravity waves are specified at ∼500 hPa, but at 10 hPa in TIME-GCM. Gravity wave filtering in the troposphere is included in WACCM but not in TIME-GCM, which may result in the better SSW simulations by WACCM. However, it should be noted that WACCM simulation is taken from one of the climate simulation and it is possible that self-consistent WACCM accidentally simulate the right height of zero-wind height.

Based on above analysis, gravity waves play an important role in setting up an adequate height of the zero-wind line and alter planetary wave structure. To further confirm the importance of the initial height of the zero-wind line, an idealized simulation study that can control the height of the zero-wind line without altering the planetary wave amplitudes is needed.

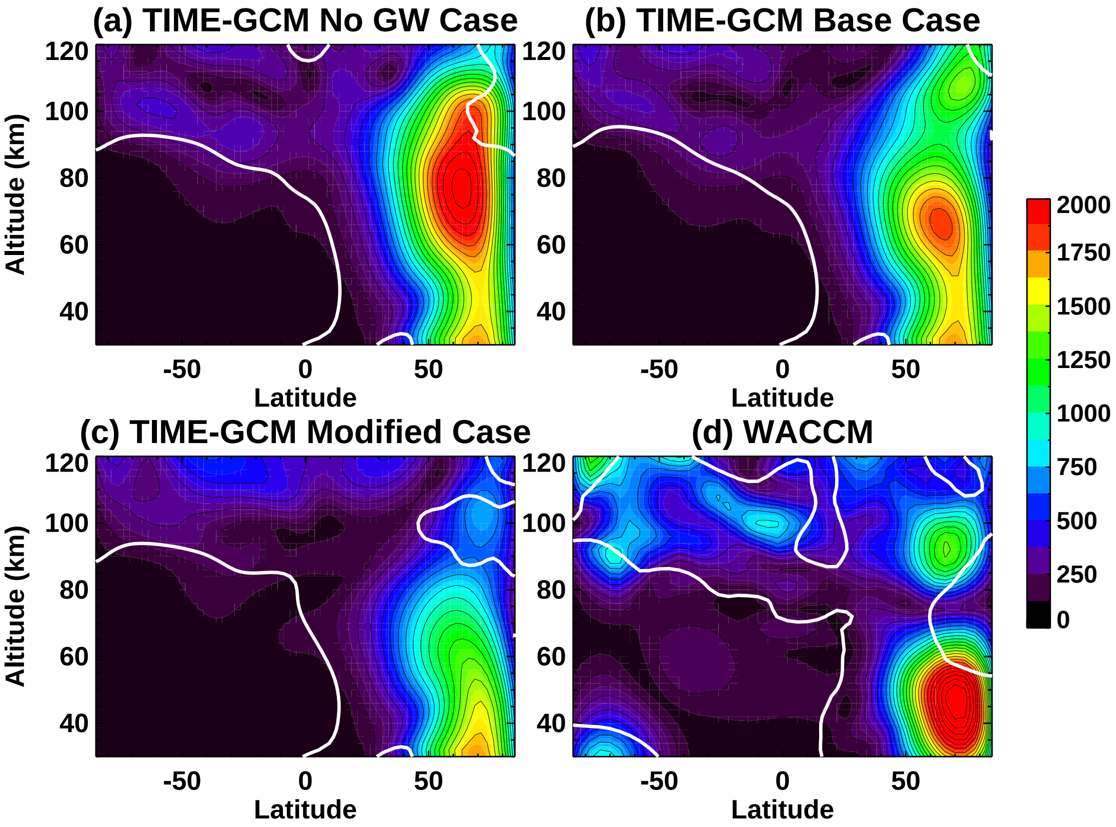

Figure 5.7: The zonal mean amplitudes of wavenumber 1 components of geopotential height perturbations (m) on January 23 for TIME-GCM simulations with (a) no gravity wave parameterization, (b) the base case, and (c) modified case gravity wave parameterization, (d) WACCM simulations. White lines represent the zero-wind line of zonal mean zonal wind.

5.5 Conclusions

This chapter examines how the height, vertical depth, and magnitude of the cooling and warming regions in the MLT vary with gravity wave parameters in TIME-GCM during a minor SSW. All of the TIME-GCM simulations with and without gravity wave parameterization show the stratospheric jet reversal, the stratospheric warming, and the mesospheric cooling. Thus, we confirm that the general features of SSWs in the stratosphere and the lower mesosphere are mainly determined by planetary waves as suggested by Matsuno [1971]. The height, vertical depth, and magnitude of the MLT cooling and warming regions, on the other hand, vary significantly with gravity wave forcing.

The characteristics of gravity wave forcing are heavily dependent on the specifications of gravity wave parameters in the model: gravity waves with wider spectral width produce the wider vertical extent of the gravity wave forcing region, and gravity waves with longer horizontal wavelengths and larger amplitudes result in the lower height of the gravity wave forcing region. The gravity wave forcings control the pattern and strength of residual circulation and thereby the characteristics of the MLT cooling and warming regions. The height of the MLT cooling and warming regions is mainly determined by the height of gravity wave breaking. The vertical depth and magnitude of the cooling and warming regions are closely tied to the vertical depth and magnitude of the gravity wave forcing. Both of these features could be modified by planetary wave forcing through influencing the residual circulation. Our simulations in the base case show that westward gravity wave forcings at middle latitudes and planetary wave forcings at high latitudes induce poleward flow in the lower thermosphere above the equatorward flow in the upper mesosphere generated by eastward gravity wave forcings at high latitudes. This circulation drives the downward flow in the lower thermosphere and the upward flow in the upper mesosphere, leading to the adiabatic warming and cooling, respectively. Furthermore, the planetary wave occurrence height can vary with gravity wave breaking height, leading to the cancellation between planetary wave and gravity wave forcings. This could further modify the circulation thus the cooling and warming characteristics in the MLT. These planetary waves occurring at high latitudes in MLT are likely generated in-situ by gravity wave forcings. Therefore, our study shows that the height, width, and magnitude of the MLT cooling and warming regions during SSWs are strongly affected by gravity waves directly through gravity wave forcing and indirectly through the in-situ generation of planetary waves.

Capturing the downward progression of temperature anomaly from the mesosphere to the stratosphere is dependent on gravity wave parameters in the model. Because the zero-wind line is the critical layer for the stationary planetary waves, the height of zero-wind line at the onset of SSWs is most likely one of the key elements of downward progression. Although planetary waves are the main driver for downward progression, gravity waves likely affect the downward progression through modifying the height of zero-wind line, altering planetary wave amplitudes, and inducing additional vertical circulation.

Therefore, this study suggests the roles of gravity waves during SSWs as the following: (1) Gravity waves set up the adequate height of the zero-wind line for planetary waves and gravity waves to interact with mean flow at the onset of SSW, (2) gravity wave forcings accelerates the meridional circulation equtorward and induces the warming in the lower thermosphere and the cooling in the mesosphere, (3) the longitudinal variations of gravity wave forcing in the MLT caused by planetary waves in the stratosphere excite secondary planetary waves in MLT that further modify the MLT circulation. Given the sensitivity of MLT response to gravity wave parameters, uncertainties in gravity wave parameters may be responsible for the discrepancy between model and observations. The variability of MLT temperature responses to different SSW events may also reflect the variability in gravity wave source and propagation. Better knowledge of the gravity wave source and propagation during SSWs is thus critical for correctly simulating the MLT impact of SSWs.

Chapter 6

Impacts of Gravity Wave Variations on the Upper Atmosphere for the 2009 Stratospheric Sudden Warming

In this chapter, the impacts of gravity wave variations on the MLT temperatures are investigated through implementing the ECMWF gravity wave variations in the TIME-GCM for the 2009 SSW simulations. Two controlled simulations are conducted with (1) the wavenumber 2 signatures of gravity wave enhancements prior to the peak SSW and (2) the suppressiona of gravity waves after the wind reversal.

6.1 Introduction

Gravity wave variations associated with the 2009 SSW are quite dynamic as shown in Figure 3.3. Impacts of these realistic gravity wave variations have never been examined despite the important roles of gravity waves in driving atmospheric circulation. In this study, gravity wave influences on two important atmospheric phenomena—the initiation of SSW anomalies in the mesosphere and the elevated stratopause—are examined.

As discussed in Chapter 5, the SSW temperature anomalies start in the mesosphere, and then progress downward to the stratosphere and further to the troposphere. The initiation of the temperature anomalies in the mesosphere is important to understand atmospheric coupling and predictions of SSWs. The elevated stratopause is often observed after the strong SSW (e.g., the 2006 NH SSW and the 2009 NH SSW) [Manney et al., 2008, 2009]. The stratopause is normally located at ∼50–60 km. However, after the strong SSWs, the stratopause seems to be elevated to

∼80–90 km. This movement of the stratopause is called the elevated stratopause [Manney et al., 2008, 2009; Siskind et al., 2007; Chandran et al., 2011]. The elevated stratopause likely results from the changes of gravity wave filtering and the vertical circulation due to the modulations of background flow associated with SSWs [Siskind et al., 2007, 2010; Chandran et al., 2011] or planetary waves [Limpasuvan et al., 2011]. Associated with the changes in atmospheric circulation, anomalies in NOx in the stratosphere have been observed [Randall et al., 2006]. The NOx can alter stratospheric ozone through catalytic cycle [Randall et al., 2006]. Hence, understanding the mechanisms of the elevated stratopause is also important to advance our knowledge of ozone depletion related to NOx transport and atmospheric circulation.

Siskind et al. [2007] proposed a mechanism of the elevated stratopause as the filtering of orographic gravity waves and tested it with the NOGAPS-ALPHA model that used an orographic gravity wave parameterization scheme. According to Siskind et al. [2007], during the recovery phase of SSWs, zonal winds are westward in the stratosphere and eastward in the mesosphere because the eastward jet recovery starts in the MLT region. Orographic gravity waves are filtered because of the wind reversal between the troposphere and the lower mesosphere, resulting in the lack of gravity waves in the MLT (if only orographic gravity waves are considered). During the normal winter condition, the westward gravity wave forcing in the mesosphere induces the warming in the mesosphere and upper stratosphere, and cooling in the lower thermosphere and mesosphere through adiabatic warming and cooling, respectively. On the other hand, during the recovery phase of SSWs, the westward gravity wave forcing disappears. As a result, temperatures in the mesosphere and upper stratosphere decrease, and temperatures in the lower thermosphere and mesosphere increase due to the lack of vertical circulation induced by the westward gravity wave forcing in the mesosphere. Based on this theory, Siskind et al. [2007] successfully simulated the elevated stratopause after the 2006 SSW; however, the magnitude of the elevated stratopause was much weaker than that observed by SABER.

Following Siskind et al. [2007], Siskind et al. [2010] re-examined the elevate stratopause by NOGAPS-ALPHA with both orographic and non-orographic gravity wave parameterizations.

The simulations of the elevated stratopause at ∼90 km with non-orographic gravity waves were improved from results only with orographic gravity waves. Elevated stratopause was also captured by WACCM climate simulations with both non-orographic and orographic gravity wave parameterization scheme [Chandran et al., 2011]. Both Siskind et al. [2010] and Chandran et al. [2011] concluded that westward gravity wave forcing in the MLT region is responsible for simulating the magnitude of the elevated stratopause reasonably.

Simulation results by Siskind et al. [2010] and Chandran et al. [2011] are somewhat conflicting with gravity wave observations. HIRDLE satellite observed the suppressions of gravity wave momentum flux after the 2006 SSW during the period of the elevated stratopause [Wright et al., 2010]. Thurairajah et al. [2010] also presented the reductions of gravity wave activity observed by lidar. In additions to observations, Yamashita et al. [2010] (also in Chapter 3 and 4 in this dissertation) showed the suppression of gravity waves with the horizontal wavelength larger than ∼150 km when the elevated stratopause occurred in the 2009 SSW using the high-resolution numerical model. These observations and modeling results seem to be supporting the theory proposed by Siskind et al. [2007] with suppressions of orographic gravity waves. Therefore, the mechanisms of the elevated stratopause remain unclear, and this study aims to explain the causes of discrepancies between GCM simulations and observations by considering the observational filtering and gravity wave spectra used in the gravity wave parameterization schemes.

For the 2009 SSW, the timing of enhancement and suppression of gravity waves seen in ECMWF-T799 corresponds to the period of the initiation of downward progressions of the 2009 SSW (precursor of the SSW) and the occurrence of the elevated stratopause, respectively. It is thus interesting to study the consequences of the coincidence of significant gravity wave variations with two atmospheric phenomena mentioned above. In this study, realistic gravity wave variations resolved by ECMWF-T799 are implemented in TIME-GCM. This chapter examines the initiations of SSWs in the MLT region and the mechanisms of the elevated stratopause. Gravity wave variations at ∼30–45 km obtained from ECMWF-T799 contain gravity wave filtering and source variations in the troposphere and in-situ gravity wave source variations in the stratosphere. The in-situ gravity wave source variations have never been included in any of the models that were used to examine the elevated stratopause (e.g., WACCM, TIME-GCM, and NOGAPS-ALPHA). Therefore, this study provides a new insight of MLT responses to realistic gravity wave source variations.

6.2 Method

The impacts of realistic gravity wave variations are examined through implementing ECMWF-resolved gravity wave variations in the gravity wave parameterization scheme in TIME-GCM. Two signatures are implemented in TIME-GCM: (Case 1) wavenumber 2 gravity wave enhancements prior to wind reversal and (Case 2) suppressions of gravity waves after the peak SSW.

(1) **Base Case**

The typical gravity wave parameters are used to simulate the 2009 SSW by TIME-GCM. The lower boundary of TIME-GCM at 10 hPa is specified by the 6-hourly ECMWF data along with the migrating diurnal and semidiurnal tides from the Global Scale Wave Model (GSWM). Detailed descriptions of gravity wave parameterization scheme and TIME-GCM can be found in Chapter 5, Liu and Roble [2002] and references therein. In this study, spectral width of -90 m/s to 90 m/s and horizontal wavelength of 400 km (based on ECMWF study) are used.

(2) **Case 1**

The wavenumber 2 signatures of gravity wave enhancements shown in Figure 6.1 are implemented in TIME-GCM during the period of January 15 to January 23. The normalized zonal mean momentum flux in Figure 6.1 is averaged over altitude range of 30–45 km. The weighting function contained wavenumber 2 signatures plotted as the thick gray line in Figure 6.1 is applied on the intermittency term (efficiency term in TIMEGCM) to simulate the longitudinal variations. The magnitudes of daily-zonal mean GW-Ep are roughly three times larger than GW-Ep during the normal winter condition, and the weighting function is multiplied by 3 to include the amplifications of gravity waves. This modification is applied to the latitude range of 30°-90°N.

(3) **Case 2a**

The amplitude of GW-Ep after the 2009 SSW is about 30% of GW-Ep before the 2009 SSW. Figure 6.1 shows the polar plots of gravity wave activity after the SSW on February 20 with extremely weak gravity wave activities. The efficiency terms used in the TIME-GCM gravity wave parameterization scheme are multiplied by 0.3 to represent the suppression of gravity waves. This modification is applied to the latitude range of 30°–90°N from January 24 to February 28.

(4) **Case 2b**

ECMWF-T799 cannot resolve gravity waves that have horizontal wavelength less than ∼150 km. Hence, the suppressions of gravity waves in ECMWF do not mean that all gravity waves disappeared, but gravity waves with horizontal wavelengths less than ∼150 km can exist. For case 2b, gravity wave horizontal wavelength is reduced from 400 km to 10 km in order to represent gravity waves that cannot be resolved in ECMWF-T799. This modification is applied to the latitude range of 30°–90°N from January 24 to February 28.

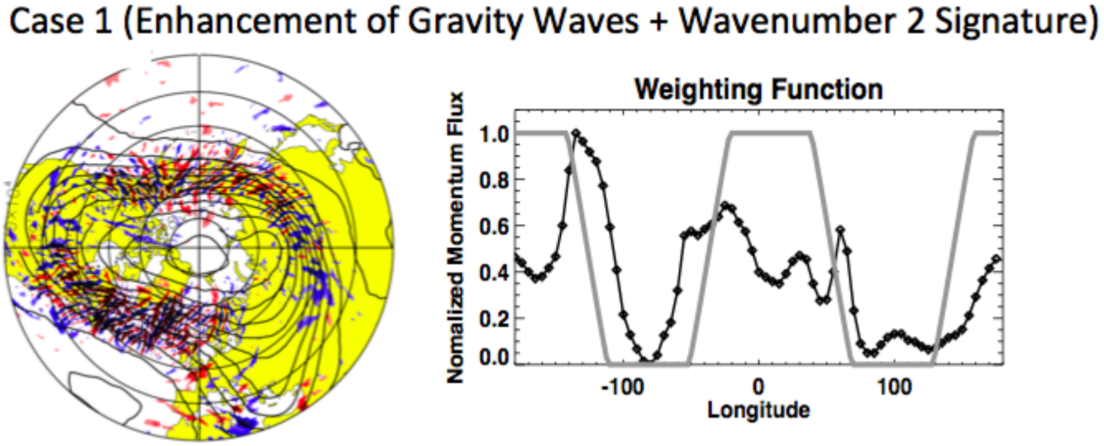

Case 1 (Enhancement of Gravity Waves + Wavenumber 2 Signature)

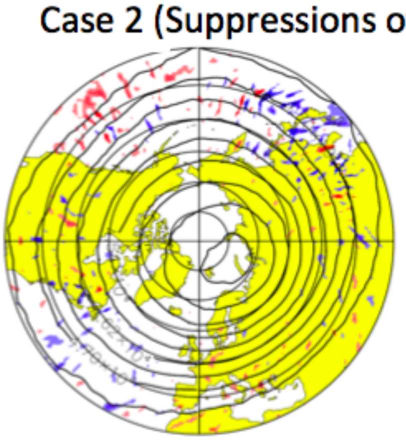

Case 2 (Suppressions of Gravity Waves)

Figure 6.1: Vertical wind from ECMWF-T799 on (top left) January 16 and (bottom left) on February 20. (Top right) longitudinal variations of normalized momentum flux averaged over altitude range of 30–45 km, the latitude range of 50°–90°N, and January 16–17, 2009 (black solid) and wavenumber 2 weighting function implemented in TIME-GCM (gray solid).

6.3 TIME-GCM: Base Case

Figure 6.2 shows zonal-daily mean temperatures in the latitude range of 70°–75°N and temperature anomalies from the TIME-GCM base case and SABER observations. Temperature anomalies are estimated by subtracting temperature on January 11 from every day temperature. January 11 is chosen because SABER observation at the northern high latitudes starts on January 11. Downward shifts of warm temperature region in the stratosphere from ∼60 km to ∼40 km in the period of day of year (DOY) 11–25 are captured in the TIME-GCM base case simulation and SABER observations. In addition, the warming regions at ∼80 km (i.e., the elevated stratopause) in the period of DOY 35–55 are simulated in the TIME-GCM base case as observed by SABER. However, the magnitudes of the downward shift of warming from 60 km to 40 km on DOY 11–25 and the elevated stratopause on DOY 35–55 are much weaker in the TIME-GCM base case than those in SABER observations.

Comparing temperature anomalies in Figure 6.2, the general structures of warming in the stratosphere, cooling in the mesosphere, and warming in the lower thermosphere are simulated by the TIME-GCM base case and observed by SABER. The characteristics of MLT temperature anomalies show discrepancies between the TIME-GCM base case and SABER observations, which can be expected from results in Chapter 5.

Zonal wind and gravity wave forcings are shown in Figure 6.3. Zonal mean zonal winds are reversed from eastward to westward on January 23 and reversed back to eastward on ∼January 28. Directions of gravity wave forcings vary according to the changes of zonal winds because of the changes in gravity wave filtering. The recovery of the stratospheric jet after the peak SSW starts at ∼60–80 km that is ∼20 km higher than the location of the stratospheric jet prior to the SSW. Owing to the changes of the stratospheric jet, the heights of westward forcings are lifted from ∼65–100 km on DOY 11–15 to ∼80–115 km on DOY 30–55.

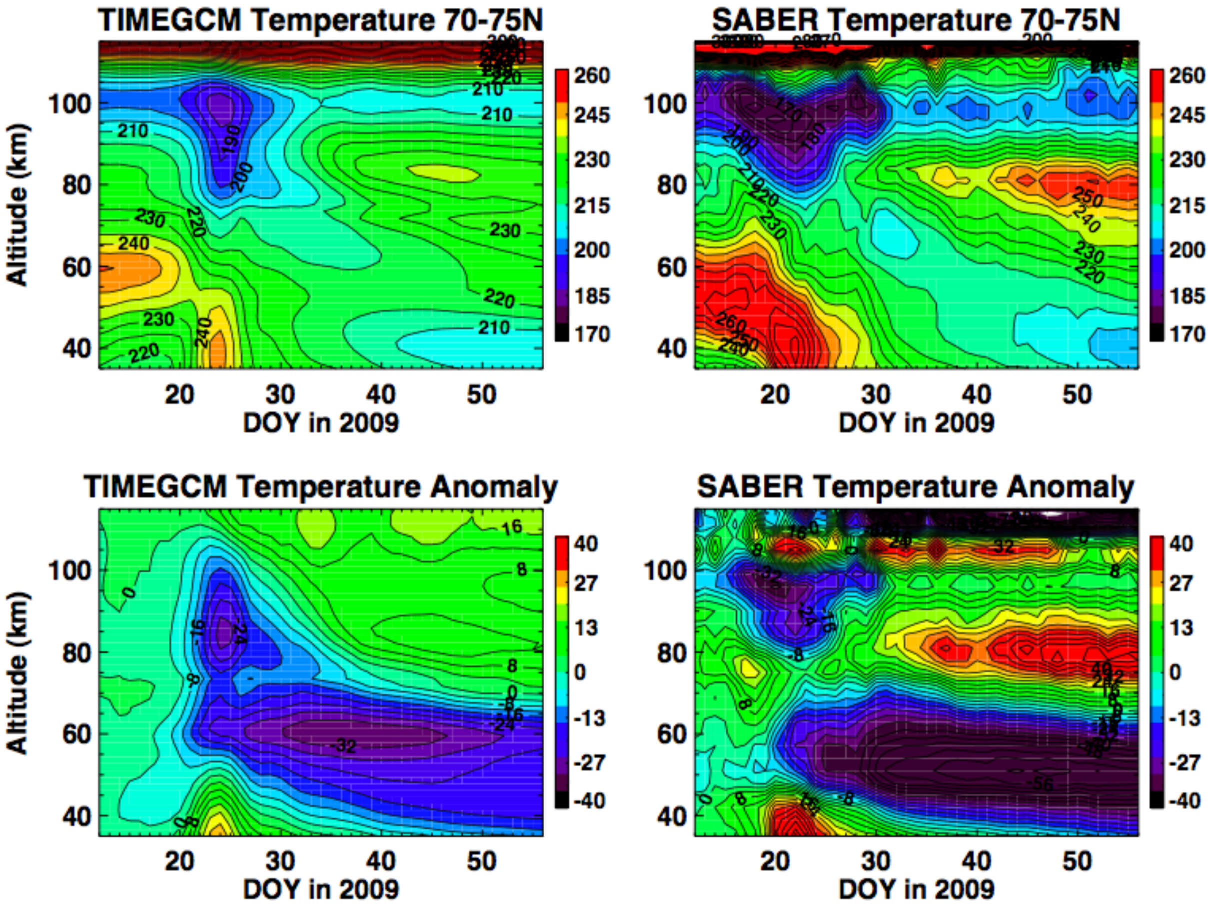

Figure 6.2: (Top) Zonal mean temperatures in the latitude range of 70°–75°N and (bottom) temperature anomaly (changes from January 11) for (left) the TIME-GCM base case and (right) SABER observations for the 2009 SSW.

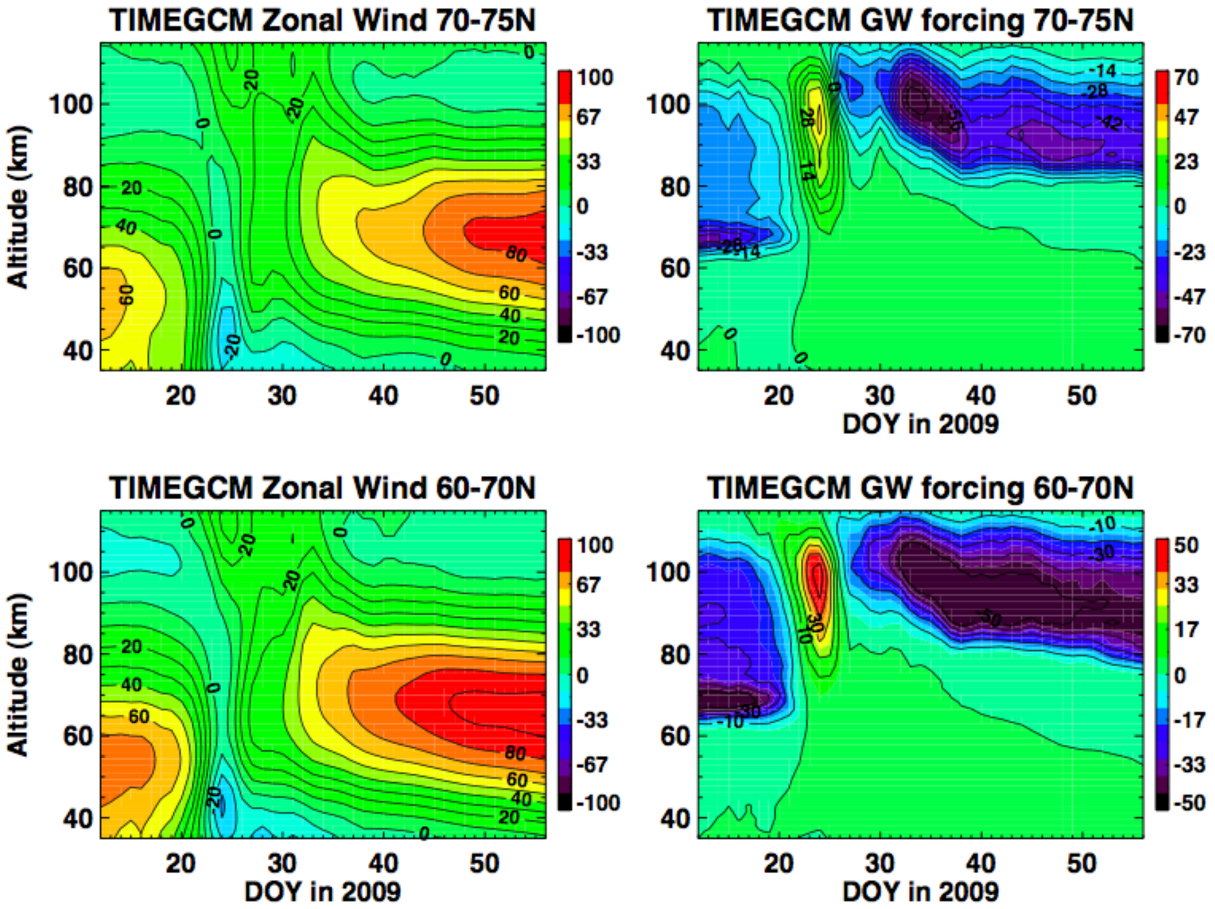

Figure 6.3: (Left) Zonal mean zonal wind and (right) gravity wave forcing in the latitude range of (top) 70°–75°N and (bottom) 60°–70°N for the 2009 SSW from the TIME-GCM base case. Positive (negative) indicates the eastward (westward).

6.4 TIME-GCM: Control Case 1

To understand the impacts of gravity wave enhancements, gravity wave parameterization is modified based on the longitudinal variations of zonal wavenumber 2 signatures and enhancements of gravity wave activity (case 1). Figure 6.4 shows the time-variations of zonal-daily mean temperatures in 70°–75°N from SABER observation and the TIME-GCM base case and case 1 simulations. The black box in Figure 6.4 indicates the period that the longitudinal variations and enhancements are implemented based on ECMWF-T799 results. The magnitudes of temperatures in the altitude range of 50–70 km in the period of DOY 15–23 are larger in case 1 than that in the base case, and temperatures in the altitude range of 80–110 km are colder in case 1 than that in the base case. Temperatures in the stratosphere and in the mesosphere are better simulated by TIME-GCM case 1 than the base case, compared to SABER observations.

Figure 6.5 shows the comparisons of temperature anomalies. Again, the black box in Figure 6.5 indicates the period of modifications of gravity wave parameterization. In the period of DOY 15–23, the cooling in the altitude range of 90–110 km and warming in the altitude range of 65–90 km in case 1 are improved compared to SABER observations. Without gravity wave variations, the initiation of temperature anomalies (the precursor of SSWs) in the MLT region is not represented in the TIME-GCM base case. To further quantify the influences of gravity wave enhancements, the magnitudes of temperature differences between the base case and case 1 are shown in Figure 6.6. The magnitudes of the cooling and warming induced by gravity wave enhancements are ~10 K in 90–110 km and ~5–10 K in 40–90 km, respectively. The cooling in the lower thermosphere and warming in the upper mesosphere observed by SABER in the period of DOY 15–20 are ~35 K and ~20 K, respectively. The modifications of gravity wave parameterization in case 1 improve the cooling simulation by ~30% and the warming simulation by ~40%.

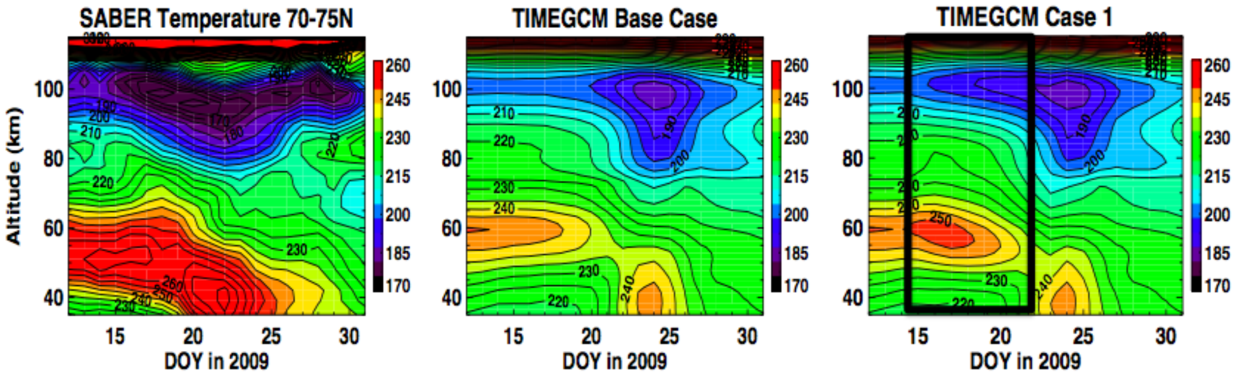
SABER Temperature 70-75N

TIMEGCM Base Case

TIMEGCM Case 1

Figure 6.4: Zonal mean temperatures from (left) SABER observations, (middle) the TIME-GCM base case, and (right) TIME-GCM case 1 in the latitude range of 70°–75°N.

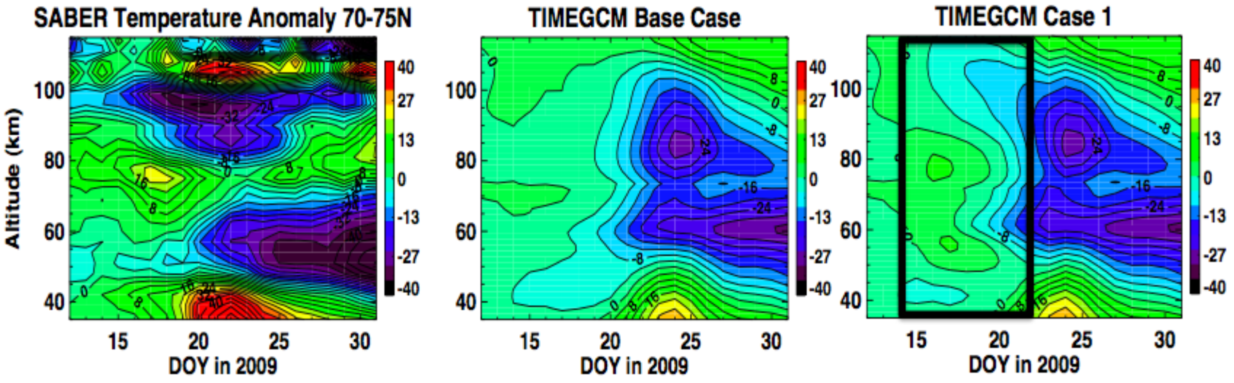
SABER Temperature Anomaly 70-75N

TIMEGCM Base Case

TIMEGCM Case 1

Figure 6.5: Zonal mean temperature anomalies from (left) SABER observations, (middle) the TIME-GCM base case, and (right) TIME-GCM case 1 in the latitude range of 70°–75°N.

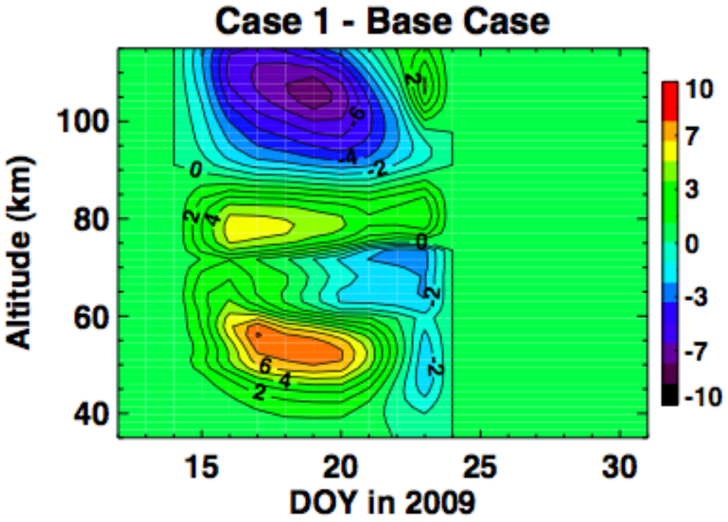

Figure 6.6: Differences between case 1 and the base case (case 1 - the base case) in the latitude range of 70°–75°N.

6.5 TIME-GCM: Control Case 2

In order to understand the impacts of suppressions of gravity waves seen in ECMWF-T799 results, TIME-GCM parameterization is modified as the control case 2a and case 2b discussed in the method section. Case 2a simply suppresses gravity wave forcing in TIME-GCM. Case 2b replaces the horizontal wavelength from 400 km to 10 km considering the existence of short-horizontal wavelength waves that cannot be resolved in ECMWF-T799.

Figure 6.7 illustrates temperatures from SABER observations, the TIME-GCM base case, case 2a, and case 2b. The black boxes shown in Figure 6.7 indicate the period of gravity wave modifications in TIME-GCM. Focusing on the elevated stratopause between January 25 (DOY 25) and February 25 (DOY 56), the temperature in the altitude range of ∼70–100 km are ∼250 K in SABER, ∼230 K in the base case, ∼225 K in case 2a, and ∼240 K in case 2b. In case 2a, the magnitudes of warming in 70–90 km and cooling in 90-110 km are weaker than the base case stimulation. Based on comparisons between SABER and TIME-GCM simulations, TIME-GCM case 2a with suppressions of gravity waves does not improve the simulation of the elevated stratopause but deteriorates the elevated stratopause simulation. TIME-GCM case 2b with gravity waves of 10 km horizontal wavelength provides the best simulation of the elevated stratopause among three TIME-GCM simulations. The magnitude of the elevated stratopause in case 2b is close to SABER observations, and the vertical depth of warming region from 60 km to 90 km around DOY 50–56 are very close to the SABER observations.

To further compare TIME-GCM simulations, the temperature anomalies are shown in Figure 6.8. The magnitudes of warming in the altitude range of 60-90 km above the cooling in the stratosphere are ∼40 K in SABER observations, ∼10 K in the base case, ∼8 K in case 2a, and ∼20 K in case 2b. Obviously, the warming in the altitude range of 60–90 km in SABER is much warmer than all of TIME-GCM simulations. However, TIME-GCM case 2b improves the warming in the altitude range of 60–90 km compared with the base case.

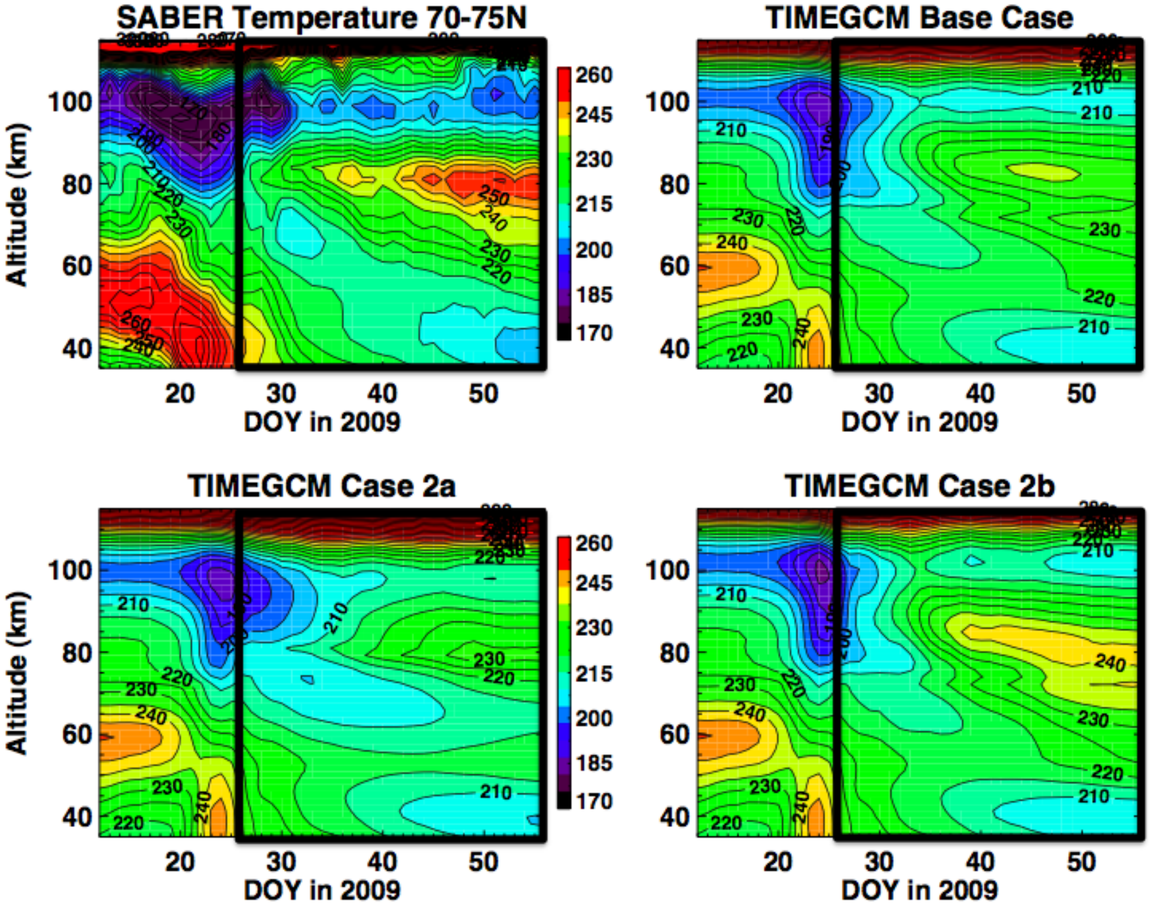

Figure 6.7: Zonal mean temperatures from (top left) SABER observations, (top right) the TIME-GCM base case, and (bottom left) TIME-GCM case 2a, and (bottom right) TIME-GCM case 2b in the latitude range of 70°–75°N.

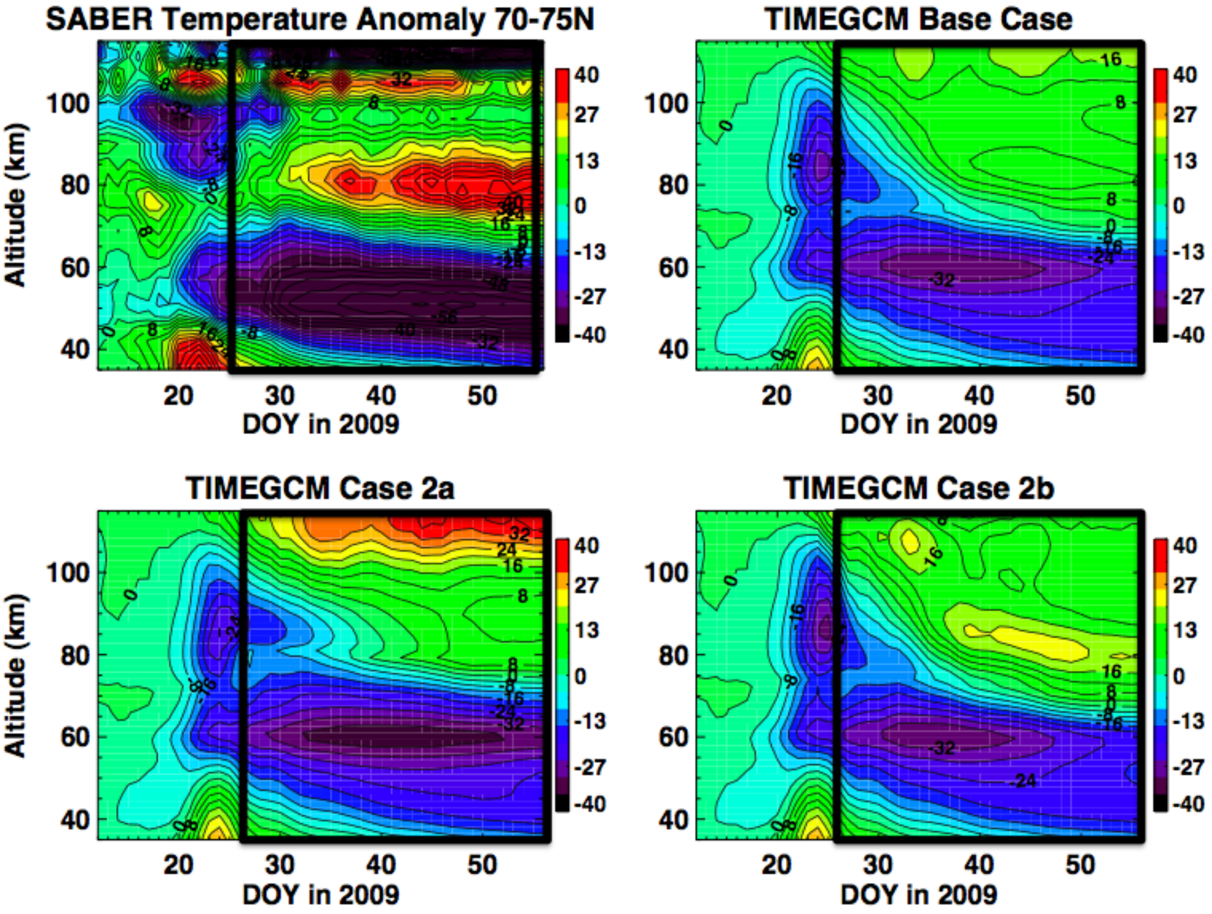

Figure 6.8: Zonal mean temperature anomalies from (top left) SABER observations, (top right) the TIME-GCM base case, and (bottom left) TIME-GCM case 2a, and (bottom right) TIME-GCM case 2b in the latitude range of 70°–75°N.

6.6 Discussion

As discussed in Chapter 5, gravity waves are likely a key to the initiations of temperature anomalies in the MLT region that leads the downward progressions of SSWs from the mesosphere to the stratosphere and sometimes further to the troposphere. In order to examine the changes of the zero-wind line height, Figure 6.9 shows zonal mean zonal wind in the latitude range of 70°–75°N. The red thick lines in Figure 6.9 represent the zero-wind line of zonal winds. The zero-wind line heights are ∼90 km in the base case and ∼75 km in case 1 from January 16–23. The zonal mean gravity wave forcings are shown in Figure 6.10. From both Figures 6.9 and 6.10, it is clear that the zero-wind line is shifted from ∼90 km (the base case) to ∼75 km (case 1) due to the enhancements of the westward gravity wave forcing from ∼60–90 km in case 1. The increases of westward gravity wave forcing in case 1 cause the additional upward and downward flow, resulting in the warming and cooling in the MLT region. The changes in gravity wave forcing and the zero-wind height also alter planetary wave structure. However, the main contributor to the cooling and warming in the MLT region is the increase of gravity wave forcing in this case. This study indicates that the precursors of temperature anomalies prior to the peak SSWs can be strongly tied to the gravity wave variations.

Suppressions of gravity waves after SSWs have been observed by lidar and HIRDLE satellite and simulated by ECMWF-T799 [e.g., Wright et al., 2010; Yamashita et al., 2010], conflicting with model results that require the strong westward gravity wave forcing in MLT region for simulations of the elevated stratopauses [Siskind et al., 2010; Chandran et al., 2011]. Based on the TIME-GCM simulations shown in this Chapter, a key of simulating the elevated stratopause is high-frequency gravity waves that cannot be observed by current satellite instruments and also ECMWF-T799. These results explain the conflicts between GCM simulations and suppressions of gravity waves captured by HIRDLE and ECMWF-T799 [Wright et al., 2010; Yamashita et al., 2010].

In TIME-GCM simulations, the elevated stratopause associated with the 2009 SSW is likely caused by westward gravity wave forcing above the occurrence height of the elevated stratopause,

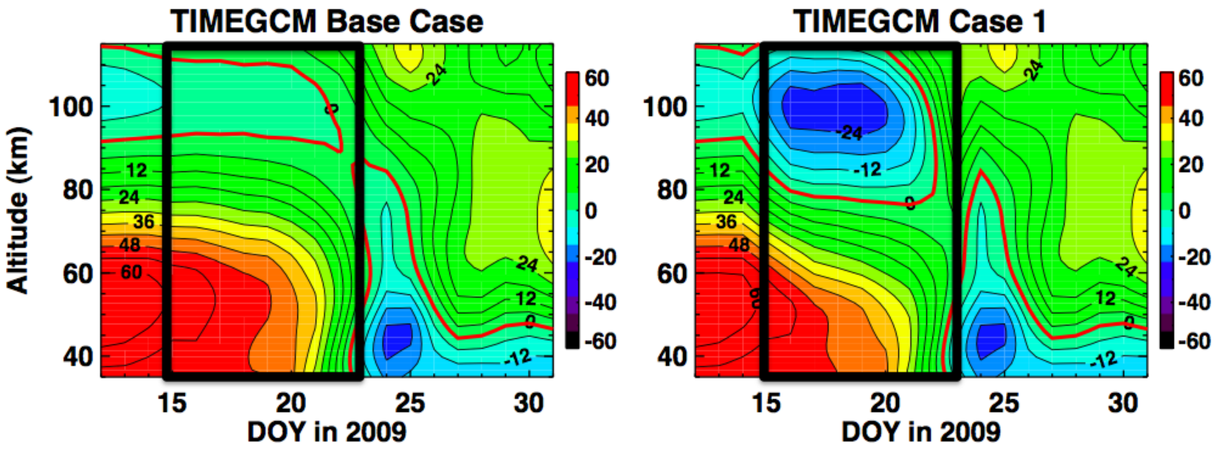

Figure 6.9: Zonal mean zonal wind from (left) the TIME-GCM base case and (right) TIME-GCM case 1 in the latitude range of 70°-75°N.

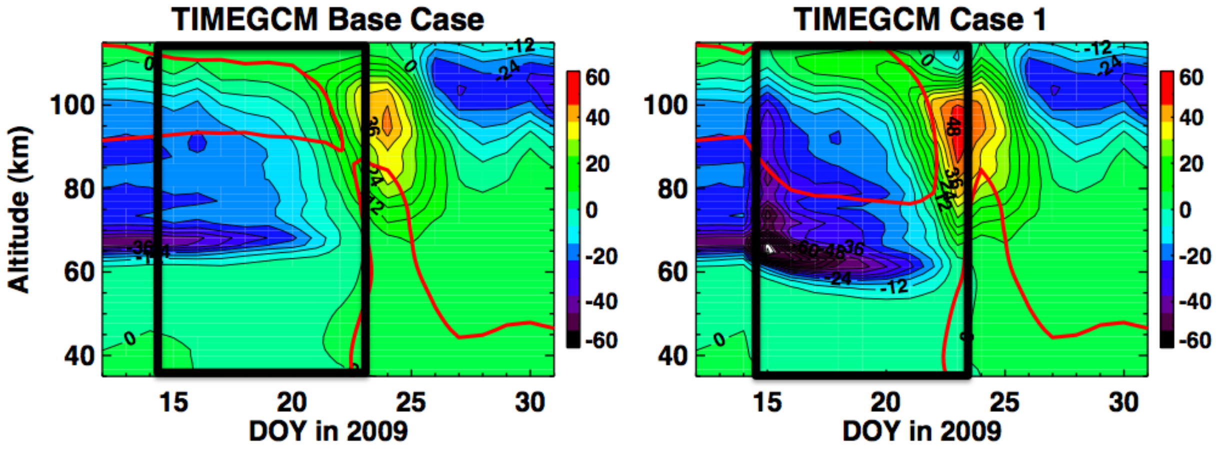

Figure 6.10: Graivity wave forcing from (left) the TIME-GCM base case and (right) TIME-GCM case 1 in the latitude range of 70°-75°N.

consistent with previous study by Siskind et al. [2010] and Chandran et al. [2011]. The region of westward gravity wave forcing during the elevated stratopause is shifted upward ∼20 km compared to the normal winter condition. This is because recovery of eastward jet stream starts at the upper mesosphere then progress downward to the stratosphere as shown in Figure 6.3. Westward gravity waves thus propagate to higher altitudes during the period of elevated stratopause. The changes of altitudes of gravity wave propagation is likely responsible for the elevated stratopause in TIME-GCM. The gravity waves with short horizontal wavelengths tend to propagate higher altitude than gravity waves with long horizontal wavelengths, which may also contribute to the "elevated stratopause generation.

6.7 Conclusions

Responses of the MLT temperature to gravity wave variations are examined by utilizing both ECMWF-T799 and TIME-GCM models. Two control simulations are conducted with (1) the enhancements of gravity wave activity prior to the 2009 SSW and (2) the suppressions of gravity wave activity after the wind reversal. The base case simulation without any gravity wave source variations captures the stratospheric warming, the cooling in the mesosphere, the warming in the lower thermosphere, and wind reversal. Gravity wave variations are thus not the main driver of SSWs as discussed by Matsuno [1971].

SABER observations indicate the cooling in the upper mesosphere and the warming in the lower mesosphere prior to the peak SSW around January 16–20, which can be considered as the precursor of the 2009 SSW. These MLT temperature responses prior to the 2009 SSW are not simulated well by the base case TIME-GCM. The case 1 with enhancements of gravity waves begins to show the temperature anomalies in the MLT region prior to the peak SSW, resulting from the enhancements of westward gravity wave forcings in the MLT. Changes in gravity wave forcing also alter the height of the zero-wind line and planetary wave structures, and the modification of planetary wave structure slightly contributes to the MLT temperature anomaly prior to the peak SSWs. However, in this case, temperature changes induced by enhancements of westward gravity wave forcing are the main causes of the precursor of SSW in the MLT.

To understand the impacts of the suppressions of gravity waves, a gravity wave parameterization is further modified to suppress the gravity waves with the horizontal wavelength longer than 150 km and to consider the short-horizontal wavelength (10 km) gravity waves. TIME-GCM simulation with 10 km horizontal gravity wave wavelength provides the best simulation of the elevated stratopause among three different TIME-GCM cases. Based on this study, a key of the elevated stratopause is most likely the high-frequency gravity waves that cannot be resolved in high-resolution models or observed by current satellites, which explains the conflict between previous simulations and observations of gravity waves during the period of the elevated stratopause.

Chapter 7

Conclusions and Outlook

7.1 Conclusions

Utilizing the high-resolution ECMWF-T799, TIME-GCM, and GROGRAT models, I have studied atmospheric coupling through gravity waves during SSW in this dissertaion. The studies include the following aspects: (1) the temporal, spatial, and spectral variations of gravity waves during SSWs, (2) the physical mechanisms behind these variations and the in-situ generation mechanisms of gravity waves during SSWs, and (3) the roles of gravity waves in atmospheric coupling. A major finding is the importance of the in-situ excitations of gravity waves by the residual tendency forcings prior to the 2009 SSW. The increase of in-situ gravity waves sources plays a key role in initiating the temperature anomalies in the MLT region that progress downward to the stratosphere and the troposphere later. Advancements made by this dissertation will greatly contribute to the future development of gravity wave parameterization schemes that include in-situ gravity wave sources related to the jets. Furthermore, the improvements of knowledge on atmospheric coupling mechanisms through gravity waves are expected. The answers to the scientific questions asked in the Introduction (Chapter 1) are in the following:

(1) **How do gravity waves vary during the 2009 SSW in the stratosphere and lower mesosphere?**

Gravity wave variations during the 2009 SSW are studied using the high-resolution ECMWF-T799. ECMWF-T799 is validated with COSMIC/GPS temperature for daily and short-term variations associated with the 2009 SSW and with lidar observations for seasonal variations. The 2009 SSW was the largest in the observational history and occurred on January 23–24. During the development and the onset of the SSW, the daily-zonal mean GW-Ep in the stratosphere and the lower mesosphere first increases on January 5 in coincidence with PW1 growth. Then GW-Ep enhances again on January 15–22 as the PW2 magnifies. Most gravity waves occur at the edge of the polar vortex, and the magnitude and occurrence of gravity waves correlate well with the location and strength of the polar vortex that is strongly distorted by planetary wave growth. As the significant planetary wave disturbances (initially at the lower mesosphere) migrate down to the stratosphere, strong gravity waves (also initially enhanced at higher altitudes on January 5) gradually progress downward to the stratosphere around January 22. Downward progression of GW-Ep and planetary wave enhancement on January 15–22 appears to follow the zero-wind line. Two gravity wave peaks on January 5 and 15–22 are dominated by 100–800 km and 400–1600 km bands, respectively, indicating the spectral dependence of the gravity wave enhancements. All of gravity wave enhancements occur before the wind reversal, and gravity waves become significantly weak after the 2009 SSW. The overall GW-Ep variations in ECMWF are confirmed by COSMIC/GPS observations. The combination of ECMWF and COSMIC/GPS reveals the dependence of gravity wave variations on location, altitude, time, and spectrum associated with SSWs.

(2) **What are the physical mechanisms causing the gravity wave variations during the 2009 SSW?**

The physical mechanisms of gravity wave variations during the 2009 SSW are investigated with the ECMWF-T799 and the GROGRAT ray-tracing model. The two peaks of gravity wave activities prior to the peak SSW do not show any significant correlations with the changes in probabilities of gravity wave propagation from the troposphere to the polar stratosphere using the GROGRAT ray-tracing model. Instead, two peaks correlate well with the increase of the total energy flux between 20 km to 45 km, indicating that in-situ energy source is responsible for the gravity wave enhancements. Because the Richardson numbers are larger than 0.25 where the in-situ energy increases occur in ECMWF-T799, the shear instability is unlikely a cause of the energy increases in the stratosphere for this study. The in-situ gravity wave excitation is examined utilizing the residual tendency introduced by Snyder et al. [2009]. The temporal and spatial variations of the residual tendencies correspond well with the large gravity wave activities. The spatial distributions of residual tendencies and the magnitude of the stratospheric jet stream suggest that the spontaneous responses to the residual tendencies can excite the high-frequency gravity waves, consistent with the wave characteristics appeared in ECMWF. Therefore, two peaks of gravity wave activity are strongly tied to the increase of in-situ gravity wave sources related to the stratospheric jet structures that is not included in most of gravity wave parameterization schemes.

The sudden decay of gravity wave activities correlates well with the variations of probabilities of gravity wave propagation from the troposphere to the stratosphere obtained from the GROGRAT ray-tracing model. In addition, residual tendencies are smaller after the wind reversal. These results indicate that decay of gravity waves after wind reversal is likely due to the changes of gravity wave propagation along with the weakening of in-situ gravity wave source.

(3) **What are the impacts of gravity waves on the MLT during SSWs?**

This dissertation examines gravity wave influences on the MLT dynamics, particularly on the characteristics of cooling and warming in the MLT region, downward progression of temperature anomalies, and the elevated stratopause through modifying gravity wave parameters in TIME-GCM associated with SSWs. This study confirms that the height of gravity wave forcing region is mainly determined by gravity wave amplitude and wavelength, and the vertical depth is closely tied to the spectral width of gravity wave phase speed. The gravity wave forcings control the pattern and strength of residual circulation and thereby the characteristics of MLT cooling and warming regions. The planetary wave forcings in the MLT also affect the vertical depth and magnitude of MLT temperature anomalies through further modifying the residual circulation. These planetary wave forcings are likely generated in-situ by the gravity wave forcings at high latitudes. Therefore, the mechanisms of gravity wave controlling the MLT temperature during a SSW are directly through gravity wave forcing and indirectly through generating planetary waves in-situ.

Capturing the downward progression of temperature anomalies from the mesosphere to the stratosphere is also dependent on gravity wave parameters in the model. The height of the zero-wind line at the onset of SSWs is most likely one of the key elements causing the downward progression of temperature anomalies through modulating the filtering of gravity waves and also planetary waves. Therefore, our studies suggest the roles of gravity waves as the following: (1) gravity waves set up the adequate height of the zero-wind line for planetary and gravity waves to interact with the mean flow at the onset of SSW, (2) gravity wave forcings accelerate the meridional circulation equatorward and induce the warming in the lower thermosphere and cooling in the mesosphere, (3) the longitudinal variations of gravity wave forcing in the MLT caused by planetary waves in the stratosphere excite secondary planetary waves in the MLT that further modify the MLT circulations. The TIME-GCM simulations of downward progression and the elevated stratopause are improved with the realistic gravity wave variations.

Given the sensitivity of MLT response to gravity wave parameters, uncertainties in gravity wave parameters may be responsible for the discrepancy between models and observations. The variability of MLT temperature responses to different SSW events may also reflect the variability in gravity wave source and propagation. Better knowledge of the gravity wave source and propagation during SSWs is thus critical for correctly simulating the impact of SSWs on the MLT.

7.2 Future Work

This dissertation reveals the importance of the in-situ gravity wave excitations and the roles of gravity waves on atmospheric coupling. The remaining research and possible applications are discussed here.

(1) The In-Situ Gravity Wave Generations

This dissertation identifies that the increases of the in-situ gravity wave sources are responsible for gravity wave enhancements prior to the 2009 SSW. However, Wang and Alexander [2009] argued that the changes in propagations of gravity waves are more important for the 2008 minor and major SSWs. The relevance of the in-situ wave sources can vary depending on the type, magnitude, and duration of SSWs. It is thus necessary to conduct further statistical studies with various SSW events. More case studies of gravity wave excitations by the residual tendencies are necessary for the development of gravity wave parameterizations with the in-situ gravity wave sources related to the jet structures.

(2) Impacts of Gravity Waves

Studies of gravity wave impacts on the stratosphere and also the behavior of planetary waves are not touched in this thesis, but they deserve investigation. This is because Limpasuvan et al. [2011] and Birner and Williams [2008] indicated the contributions of gravity waves to the generations of SSWs, and gravity wave impacts on the lower atmosphere can be important. Furthermore, it has been shown that the thermosphere and the ionosphere are affected by the strong lower atmospheric disturbances [Liu et al., 2010; Goncharenko et al., 2008, 2010; Liu et al., 2011]. The mechanisms of these atmospheric coupling are not clear, and contributions of longitudinal variations and temporal variations of gravity waves to these atmospheric coupling deserve further studies.

(3) Long Term Variations of the Impacts of Gravity Wave Variations

The long-term trend of gravity wave variations and their sources can be very important in the future. Gravity waves are strongly tied to the tropospheric variations, such as tropical convections, frontal system, and flow over topography. These sources are affected by the global climate change. Kawatani et al. [2010] examined gravity wave changes due to the double CO_2 condition with the Center for Climate System Research/National Institute for Environmental Studies/Frontier Research Center for Global Change (CCSR/NIES/FRCGC) Atmospheric General Circulation Model (AGCM) model that can resolve gravity waves (horizontal resolution of 1.125°). Their model has a capability of resolving QBO without any gravity wave parameterization scheme. Kawatani et al. [2010] showed the changes of gravity wave momentum fluxes and spectra due to the changes of atmospheric background wind and temperature related to the double CO_2. Although they did not investigate the impacts of the gravity wave changes on the MLT region, changes in gravity waves due to climate change may significantly affect the MLT and the stratosphere. Most of GCMs cannot resolve gravity waves and the feedback of long-term trends of gravity waves are unknown. Either improvement of the model resolutions or development of physically based gravity wave parameterization schemes with better representation of source spectra are necessary in the future.

(4) **Modeling**

The high-resolution ECMWF-T799 can resolve wide range of gravity waves; however, the resolutions of ECMWF-T799 still limit gravity wave study. For example, Limpasuvan et al. [2011] reported that gravity waves with the horizontal wavelength less than 100 km have the largest impacts on the generations of SSWs. Such small-scale gravity waves cannot be resolved in ECMWF-T799. In order to fully understand the impacts of gravity waves, both model resolutions and the height of upper boundary need to be improved. Furthermore, data handling methods for analyzing enormous amount of date need to be improved. In this study, I have analyzed the global data with 0.25° horizontal resolution [1440 (longitude) × 720 (latitude) × 91 (vertical) × 24 (hourly)] date. ECMWF-T1279 has already upgraded their model resolution to 0.15° (15 km), and it will be further improved in the year followed. Recent simulations with the Nonhydrostatic ICosahedral Atmospheric Model (NICAM) has horizontal resolution of 3 km, and this model output began to be used for studying gravity waves [Tsuchiya et al., 2011]. In order to make use of these rich model outputs, a better date handling process should be developed.

(5) **Observations**

Gravity wave observations are improved due to the recent advancements of gravity wave analysis methods using global satellite observations [Ern et al., 2004; Alexander et al., 2010]. However, observations of the long-term trend of gravity waves and high-frequency gravity waves are still missing. This dissertation indicates the importance of the high-frequency gravity waves in the elevated stratopause simulations. In order to confirm these mechanisms, the high-resolution observations are required, and lidar appears to be a powerful tool for these purposes. Network of ground-based lidar or spaceborne lidar observations along with wind measurements will advance our knowledge.

My master's thesis research, analyzing the lidar observations made by Dr. Chu and her team in Antarctica from 1999-2005, revealed the differences in seasonal variations of gravity waves at Rothera and the South Pole as shown in Figure 2.8 and the impacts of gravity waves on PMCs [Yamashita et al., 2009; Chu et al., 2009]. Although gravity waves in summer are important for controlling the brightness and occurrences of PMCs, sources of gravity waves in summer are still unclear. For example, orographic gravity waves are usually filtered by the wind reversal in the lower stratosphere in summer, and the in-situ gravity wave excitations by the stratospheric jet are weak because of the lack of the strong polar vortex in the summer stratosphere.

In addition, at the South Pole, the topography is relatively flat. The South Pole locates well inside the polar vortex, resulting in the weaker jet related gravity waves. Hence, gravity wave sources at the South Pole are still unknown. Li et al. [2009] presented that gravity waves at the South Pole probably originated in the tropical region and propagated to the polar region. However, clear observational evidences of such propagation have not been presented. Therefore, gravity wave sources in Antarctica deserve future studies. Combinations of high-resolution lidar observations with the high-resolution numerical models, such as ECMWF-T799, will help reveal the distributions of gravity wave sources in Antarctica and globally.

Bibliography

[1] M. J. Alexander and T. J. Dunkerton. A spectral parameterization of mean-flow forcing due to breaking gravity waves. Journal of the Atmospheric Sciences, 56(24):4167–4182, 1999.

[2] M. J. Alexander, M. Geller, C. McLandress, S. Polavarapu, P. Preusse, F. Sassi, K. Sato, S. Eckermann, M. Ern, A. Hertzog, Y. Kawatani, M. Pulido, T. A. Shaw, M. Sigmond, R. Vincent, and S. Watanabe. Recent developments in gravity-wave effects in climate models and the global distribution of gravity-wave momentum flux from observations and models. Quarterly Journal of the Royal Meteorological Society, 136(650):1103–1124, 2010.

[3] M. J. Alexander and H. Teitelbaum. Observation and analysis of a large amplitude mountain wave event over the antarctic peninsula. J.Geophys.Res., 112(D21):D21103, 2007.

[4] S. P. Alexander, A. R. Klekociuk, M. C. Pitts, A. J. McDonald, and A. Arevalo-Torres. The effect of orographic gravity waves on antarctic polar stratospheric cloud occurrence and composition. J.Geophys.Res., 116(D6):D06109, 03/23 2011.

[5] S. P. Alexander, A. R. Klekociuk, and T. Tsuda. Gravity wave and orographic wave activity observed around the antarctic and arctic stratospheric vortices by the cosmic gps-ro satellite constellation. J.Geophys.Res., 114(D17):D17103, 2009.

[6] D. G. Andrews, J. R. Holton, and C. B. Leovy. Middle Atmosphere Dynamics. Elsevier, New York, 1987.

[7] N. A. Bakas and B. F. Farrell. Gravity waves in a horizontal shear flow. part ii: Interaction between gravity waves and potential vorticity perturbations. Journal of Physical Oceanography, 39(3):497–511, 03/01; 2011 2009; 2009. doi: 10.1175/2008JPO3837.1; M3: doi: 10.1175/2008JPO3837.1.

[8] M. P. Baldwin and T. J. Dunkerton. Stratospheric harbingers of anomalous weather regimes. Science, 294(5542):581–584, 2001.

[9] A. J. G. Baumgaertner and A. J. McDonald. A gravity wave climatology for antarctica compiled from challenging minisatellite payload/global positioning system (champ/gps) radio occultations. J.Geophys.Res., 112(D5):D05103, 2007.

[10] Y. Bhattacharya, G. G. Shepherd, and S. Brown. Variability of atmospheric winds and waves in the arctic polar mesosphere during a stratospheric sudden warming. Geophysical Research Letters, 31(23):L23101, 12/01 2004.

[11] T. Birner and P. D. Williams. Sudden stratospheric warmings as noise-induced transitions. Journal of the Atmospheric Sciences, 65(10):3337–3343, 10/01; 2011 2008; 2008.

[12] A. Chandran, R. L. Collins, R. R. Garcia, and D. R. Marsh. A case study of an elevated stratopause generated in the whole atmosphere community climate model. Geophysical Research Letters, 38(8):L08804, 04/20 2011.

[13] A. J. Charlton, L. M. Polvani, J. Perlwitz, F. Sassi, E. Manzini, K. Shibata, S. Pawson, J. E. Nielsen, and D. Rind. A new look at stratospheric sudden warmings. part ii: Evaluation of numerical model simulations. Journal of Climate, 20(3):470–488, 2007.

[14] J. L. Chau, B. G. Fejer, and L. P. Goncharenko. Quiet variability of equatorial e b drifts during a sudden stratospheric warming event. Geophysical Research Letters, 36(5):L05101, 2009.

[15] X. Chu, W. Pan, G. Papen, C. S. Gardner, and J. Gelbwachs. Fe boltzman temperature lidar: Design, error analysis, and initial results at the north and south pole. Appl. Opt, 41:44004410, 2002.

[16] X. Chu, C. Yamashita, P. J. Espy, G. J. Nott, E. J. Jensen, H. L Liu, W. Huang, and J. P. Thayer. Responses of polar mesospheric cloud brightness to stratospheric gravity waves at the south pole and rothera, antarctica. Journal of Atmospheric and Solar-Terrestrial Physics, 71(3-4):434–445, 3 2009.

[17] K. Coughlin and K. K. Tung. Tropospheric wave response to decelerated stratosphere seen as downward propagation in northern annular mode. J.Geophys.Res., 110(D1):D01103, 01/07 2005.

[18] L. Coy, D. E. Siskind, S. D. Eckermann, J. P. McCormack, D. R. Allen, and T. F. Hogan. Modeling the august 2002 minor warming event. Geophysical Research Letters, 32(7):L07808, 04/07 2005.

[19] A. J. Dowdy, R. A. Vincent, D. J. Murphy, M. Tsutsumi, D. M. Riggin, and M. J. Jarvis. The large-scale dynamics of the mesospherelower thermosphere during the southern hemisphere stratospheric warming of 2002. Geophysical Research Letters, 31(14):L14102, 07/17 2004.

[20] T. J. Duck, J. A. Whiteway, and A. I. Carswell. Lidar observations of gravity wave activity and arctic stratospheric vortex core warming. Geophysical Research Letters, 25(15):2813–2816, 1998.

[21] T. J. Dunkerton. Inertia gravity waves in the stratosphere. Journal of the Atmospheric Sciences, 41(23):3396–3404, 1984.

[22] S. D. Eckermann and C. J. Marks. Grograt: A new model of the global propagation and dissipation of atmospheric gravity waves. Advances in Space Research, 20(6):1253–1256, 1997.

[23] N. Eguchi and K. Kodera. Impact of the 2002, southern hemisphere, stratospheric warming on the tropical cirrus clouds and convective activity. Geophysical Research Letters, 34(5):L05819, 2007.

[24] M. Ern, P. Preusse, M. J. Alexander, and C. D. Warner. Absolute values of gravity wave momentum flux derived from satellite data. Journal of Geophysical Research, 109(D20):D20103, 10/19 2004.

[25] T. D. A. Fairlie, M. Fisher, and A. O'Neill. The development of narrow baroclinic zones and other small-scale structure in the stratosphere during simulated major warmings. Quarterly Journal of the Royal Meteorological Society, 116(492):287–315, 1990.

[26] D. C. Fritts. Gravity wave saturation in the middle atmosphere: A review of theory and observations. Reviews of Geophysics, 22(3):275–308, 1984.

[27] D. C. Fritts and M. J. Alexander. Gravity wave dynamics and effects in the middle atmosphere. Reviews of Geophysics, 41(1):1003, 04/16 2003.

[28] S. Fritz and S. D. Soules. Large-scale temperature changes in the stratosphere observed from nimbus iii. Journal of the Atmospheric Sciences, 27(7):1091–1097, 1970.

[29] R. R. Garcia, D. R. Marsh, D. E. Kinnison, B. A. Boville, and F. Sassi. Simulation of secular trends in the middle atmosphere, 19502003. J.Geophys.Res., 112(D9):D09301, 05/03 2007.

[30] R. R. Garcia and S. Solomon. The effect of breaking gravity waves on the dynamics and chemical composition of the mesosphere and lower thermosphere. J.Geophys.Res., 90(D2):3850–3868, 1985.

[31] C. S. Gardner, M. S. Miller, and C. H. Liu. Rayleigh lidar observations of gravity wave activity in the upper stratosphere at urbana, illinois. Journal of the Atmospheric Sciences, 46(12):1838–1854, 06/01 1989.

[32] A. J. Gerrard, Y. Bhattacharya, and J. P. Thayer. Observations of in-situ generated gravity waves during a stratospheric temperature enhancement (ste) event. Atmospheric Chemistry and Physics Discussions, 11(5):14221–14232, 2011.

[33] A. J. Gerrard, T. J. Kane, S. D. Eckermann, and J. P. Thayer. Gravity waves and mesospheric clouds in the summer middle atmosphere: A comparison of lidar measurements and ray modeling of gravity waves over sondrestrom, greenland. J.Geophys.Res., 109(D10):D10103, 2004.

[34] A. J. Gerrard, T. J. Kane, and J. P. Thayer. Noctilucent clouds and wave dynamics: Observations at sondrestrom, greenland. Geophysical Research Letters, 25(15):2817–2820, 1998.

[35] A. J. Gerrard, T. J. Kane, and J. P. Thayer. Year-round temperature and wave measurements of the arctic middle atmosphere for 19951998. Geophys. Monogr., (123(22)):213219, 2000.

[36] A. J. Gerrard, T. J. Kane, J. P. Thayer, and S. D. Eckermann. Concerning the upper stratospheric gravity wave and mesospheric cloud relationship over sondrestrom, greenland. Journal of Atmospheric and Solar-Terrestrial Physics, 66(3-4):229–240, 3 2004.

[37] L. Goncharenko and S. R Zhang. Ionospheric signatures of sudden stratospheric warming: Ion temperature at middle latitude. Geophysical Research Letters, 35(21):L21103, 11/08 2008.

[38] L. P. Goncharenko, J. L. Chau, H. L Liu, and A. J. Coster. Unexpected connections between the stratosphere and ionosphere. Geophysical Research Letters, 37(10):L10101, 05/18 2010.

[39] L. J. Gray, S. Crooks, C. Pascoe, S. Sparrow, and M. Palmer. Solar and qbo influences on the timing of stratospheric sudden warmings. Journal of the Atmospheric Sciences, 61(23):2777–2796, 2004.

[40] F. M. Guest, M. J. Reeder, C. J. Marks, and D. J. Karoly. Inertia gravity waves observed in the lower stratosphere over macquarie island. Journal of the Atmospheric Sciences, 57(5):737–752, 2000.

[41] H. Hei, T. Tsuda, and T. Hirooka. Characteristics of atmospheric gravity wave activity in the polar regions revealed by gps radio occultation data with champ. J.Geophys.Res., 113(D4):D04107, 02/27 2008.

[42] A. Hertzog, G. Boccara, R. A. Vincent, F. Vial, and P. Cocquerez. Estimation of gravity wave momentum flux and phase speeds from quasi-lagrangian stratospheric balloon flights. part ii: Results from the vorcore campaign in antarctica. Journal of the Atmospheric Sciences, 65(10):3056–3070, 10/01 2008.

[43] A. Hertzog, C. Souprayen, and A. Hauchecorne. Observation and backward trajectory of an inertio-gravity wave in the lower stratosphere. Ann. Geophys., 19:1141–1155, 2001.

[44] A. Hertzog, F. Vial, A. Drnbrack, S. D. Eckermann, B. M. Knudsen, and J. P Pommereau. In situ observations of gravity waves and comparisons with numerical simulations during the solve/theseo 2000 campaign. J. Geophys. Res., 107, 2002.

[45] R. E. Hibbins, P. J. Espy, M. J. Jarvis, D. M. Riggin, and D. C. Fritts. A climatology of tides and gravity wave variance in the mlt above rothera, antarctica obtained by mf radar. Journal of Atmospheric and Solar-Terrestrial Physics, 69(4-5):578–588, 4 2007.

[46] C. Hines. The saturation of gravity waves in the middle atmosphere. part ii: Development of doppler-spread theory. Journal of Atmospheric Sciences, 48(11):pp.1361–1379, 1991.

[47] C. O. Hines and C. A. Reddy. On the propagation of atmospheric gravity waves through regions of wind shear. J.Geophys.Res., 72(3):1015–1034, 1967.

[48] M. H. Hitchman, J. C. Gille, C. D. Rodgers, and G. Brasseur. The separated polar winter stratopause: A gravity wave driven climatological feature. Journal of the Atmospheric Sciences, 46(3):410–422, 02/01; 2011 1989; 1989.

[49] P. Hoffmann, W. Singer, D. Keuer, W. K. Hocking, M. Kunze, and Y. Murayama. Latitudinal and longitudinal variability of mesospheric winds and temperatures during stratospheric warming events. Journal of Atmospheric and Solar-Terrestrial Physics, 69(17-18):2355–2366, 2007.

[50] J. R. Holton. The role of gravity wave induced drag and diffusion in the momentum budget of the mesosphere. Journal of the Atmospheric Sciences, 39(4):791–799, 1982.

[51] J. R. Holton. The influence of gravity wave breaking on the general circulation of the middle atmosphere. Journal of the Atmospheric Sciences, 40(10):2497–2507, 10/01 1983.

[52] J. R. Holton and J. Austin. The influence of the equatorial qbo on sudden stratospheric warmings. Journal of Atmospheric Sciences, 48(4):pp.607–618, 1991.

[53] J. R. Holton and H. C Tan. The influence of the equatorial quasi-biennial oscillation on the global circulation at 50 mb. Journal of the Atmospheric Sciences, 37(10):2200–2208, 1980.

[54] J. L. Innis and A. R. Klekociuk. Planetary wave and gravity wave influence on the occurrence of polar stratospheric clouds over davis station, antarctica, seen in lidar and radiosonde observations. J.Geophys.Res., 111(D22):D22102, 11/16 2006.

[55] E. J. Jensen and G. E. Thomas. Numerical simulations of the effects of gravity waves on noctilucent clouds. J.Geophys.Res., 99(D2):3421–3430, 1994.

[56] B. Karlsson, H. Krnich, and J. Gumbel. Evidence for interhemispheric stratosphere-mesosphere coupling derived from noctilucent cloud properties. Geophysical Research Letters, 34(16):L16806, 08/18 2007.

[57] B. Karlsson, C. McLandress, and T. G. Shepherd. Inter-hemispheric mesospheric coupling in a comprehensive middle atmosphere model. Journal of Atmospheric and Solar-Terrestrial Physics, 71(3-4):518–530, 2009.

[58] Y. Kawatani, K. Hamilton, and S. Watanabe. The quasi-biennial oscillation in a double co2 climate. Journal of the Atmospheric Sciences, 68(2):265–283, 2010.

[59] S. Y Kim, H. Y Chun, and D. L. Wu. A study on stratospheric gravity waves generated by typhoon ewiniar: Numerical simulations and satellite observations. J.Geophys.Res., 114(D22):D22104, 11/24 2009.

[60] Y. J. Kim, S. D. Eckermann, and H. Y. Chun. An overview of the past, present and future of gravity ?wave drag parametrization for numerical climate and weather prediction models. Atmosphere-Ocean, 41(1):65–98, 2003.

[61] S. E. Koch and P. B. Dorian. A mesoscale gravity wave event observed during ccope. part iii: Wave environment and probable source mechanisms. Monthly Weather Review, 116(12):2570–2592, 1988.

[62] Y. Kuroda. Effect of stratospheric sudden warming and vortex intensification on the tropospheric climate. J.Geophys.Res., 113(D15):D15110, 08/05 2008.

[63] K. Labitzke. Temperature changes in the mesosphere and stratosphere connected with circulation changes in winter. Journal of the Atmospheric Sciences, 29(4):756–766, 05/01 1972.

[64] K. Labitzke. Stratospheric-mesospheric midwinter disturbances: A summary of observed characteristics. J.Geophys.Res., 86(C10):9665–9678, 1981.

[65] K. Labitzke. Sunspots, the qbo, and the stratospheric temperature in the north polar region. Geophysical Research Letters, 14(5):535–537, 1987.

[66] Z. Li, W. Robinson, and A. Z. Liu. Sources of gravity waves in the lower stratosphere above south pole. J.Geophys.Res., 114(D14):D14103, 07/22 2009.

[67] V. Limpasuvan, M. J. Alexander, Y. J. Orsolini, D. L. Wu, M. Xue, J. H. Richter, and C. Yamashita. Mesoscale simulations of gravity waves during the 20082009 major stratospheric sudden warming. J.Geophys.Res., 116(D17):D17104, 09/03 2011.

[68] Y. Lin and F. Zhang. Tracking gravity waves in baroclinic jet-front systems. Journal of the Atmospheric Sciences, 65(7):2402–2415, 2008.

[69] R. S. Lindzen. Turbulence and stress owing to gravity wave and tidal breakdown. J.Geophys.Res., 86(C10):9707–9714, 1981.

[70] R. S. Lindzen. Dynamics in Atmospheric Physics. Cambridge University Press, 1990.

[71] H. Liu, E. Doornbos, M. Yamamoto, and S. Tulasi Ram. Strong thermospheric cooling during the 2009 major stratosphere warming. Geophysical Research Letters, 38(12):L12102, 06/21 2011.

[72] H. L Liu and J. W. Meriwether. Analysis of a temperature inversion event in the lower mesosphere. J.Geophys.Res., 109(D2):D02S07, 01/21 2004.

[73] H. L Liu and R. G. Roble. A study of a self-generated stratospheric sudden warming and its mesosphericlower thermospheric impacts using the coupled time-gcm/ccm3. J.Geophys.Res., 107(D23):4695, 12/07 2002.

[74] H. L Liu and R. G. Roble. Dynamical coupling of the stratosphere and mesosphere in the 2002 southern hemisphere major stratospheric sudden warming. Geophysical Research Letters, 32(13):L13804, 07/02 2005.

[75] H. L Liu, W. Wang, A. D. Richmond, and R. G. Roble. Ionospheric variability due to planetary waves and tides for solar minimum conditions. J.Geophys.Res., 115:A00G01, 06/29 2010.

[76] G. L. Manney, K. Kr?ger, S. Pawson, K. Minschwaner, M. J. Schwartz, W. H. Daffer, N. J. Livesey, M. G. Mlynczak, E. E. Remsberg, J. M. Russell III, and J. W. Waters. The evolution of the stratopause during the 2006 major warming: Satellite data and assimilated meteorological analyses. J.Geophys.Res., 113(D11):D11115, 06/12 2008.

[77] G. L. Manney, M. J. Schwartz, K. Kr?ger, M. L. Santee, S. Pawson, J. N. Lee, W. H. Daffer, R. A. Fuller, and N. J. Livesey. Aura microwave limb sounder observations of dynamics and transport during the record-breaking 2009 arctic stratospheric major warming. Geophysical Research Letters, 36(12):L12815, 2009.

[78] C. J. Marks and S. D. Eckermann. A three-dimensional nonhydrostatic ray-tracing model for gravity waves: Formulation and preliminary results for the middle atmosphere. Journal of the Atmospheric Sciences, 52(11):1959–1984, 1995.

[79] T. Matsuno. A dynamical model of the stratospheric sudden warming. Journal of the Atmospheric Sciences, 28(8):1479–1494, 1971.

[80] N. A. McFarlane. The effect of orographically excited gravity wave drag on the general circulation of the lower stratosphere and troposphere. Journal of the Atmospheric Sciences, 44(14):1775–1800, 1987.

[81] C. McLandress and J. F. Scinocca. The gcm response to current parameterizations of nonorographic gravity wave drag. Journal of the Atmospheric Sciences, 62(7):2394–2413, 2005.

[82] D. O'sullivan and T. J. Dunkerton. Generation of inertiagravity waves in a simulated life cycle of baroclinic instability. Journal of the Atmospheric Sciences, 52(21):3695–3716, 1995.

[83] R. Plougonven and C. Snyder. Gravity waves excited by jets: Propagation versus generation. Geophysical Research Letters, 32(18):L18802, 2005.

[84] R. Plougonven and H. Teitelbaum. Comparison of a large-scale inertia-gravity wave as seen in the ecmwf analyses and from radiosondes. Geophysical Research Letters, 30(18):1954, 09/25 2003.

[85] R. Plougonven and F. Zhang. On the forcing of inertiagravity waves by synoptic-scale flows. Journal of the Atmospheric Sciences, 64(5):1737–1742, 2007.

[86] R. W. Portmann, G. E. Thomas, S. Solomon, and R. R. Garcia. The importance of dynamical feedbacks on doubled co2?induced changes in the thermal structure of the mesosphere. Geophysical Research Letters, 22(13):1733–1736, 1995.

[87] P. Preusse, S. D. Eckermann, M. Ern, J. Oberheide, R. H. Picard, R. G. Roble, M. Riese, J. M. Russell III, and M. G. Mlynczak. Global ray tracing simulations of the saber gravity wave climatology. J.Geophys.Res., 114(D8):D08126, 2009.

[88] C. E. Randall, V. L. Harvey, C. S. Singleton, P. F. Bernath, C. D. Boone, and J. U. Kozyra. Enhanced nox in 2006 linked to strong upper stratospheric arctic vortex. Geophysical Research Letters, 33(18):L18811, 2006.

[89] M. Venkat Ratnam, T. Tsuda, C. Jacobi, and Y. Aoyama. Enhancement of gravity wave activity observed during a major southern hemisphere stratospheric warming by champ/gps measurements. Geophysical Research Letters, 31(16):L16101, 2004.

[90] S. Ren, S. M. Polavarapu, and T. G. Shepherd. Vertical propagation of information in a middle atmosphere data assimilation system by gravity-wave drag feedbacks. Geophysical Research Letters, 35(6):L06804, 2008.

[91] J. H. Richter, F. Sassi, and R. R. Garcia. Toward a physically based gravity wave source parameterization in a general circulation model. Journal of the Atmospheric Sciences, 67(1):136–156, 2010.

[92] R. G. Roble and E. C. Ridley. A thermosphere?ionosphere?mesosphere?electrodynamics general circulation model (time?gcm): Equinox solar cycle minimum simulations (30500 km). Geophysical Research Letters, 21(6):417–420, 1994.

[93] F. Sassi, R. R. Garcia, B. A. Boville, and H. Liu. On temperature inversions and the mesospheric surf zone. J.Geophys.Res., 107(D19):4380, 2002.

[94] K. Sato. A statistical study of the structure, saturation and sources of inertio-gravity waves in the lower stratosphere observed with the mu radar. Journal of Atmospheric and Terrestrial Physics, 56(6):755–774, 1994.

[95] K. Sato. Sources of gravity waves in the polar middle atmosphere. Advances in polar upper atmosphere research, 14:233–240, 2000-08.

[96] K. Sato, T. Kumakura, and M. Takahashi. Gravity waves appearing in a high-resolution gcm simulation. Journal of the Atmospheric Sciences, 56(8):1005–1018, 1999.

[97] K. Sato, S. Watanabe, Y. Kawatani, Y. Tomikawa, K. Miyazaki, and M. Takahashi. On the origins of mesospheric gravity waves. Geophysical Research Letters, 36(19):L19801, 2009.

[98] K. Sato and M. Yoshiki. Gravity wave generation around the polar vortex in the stratosphere revealed by 3-hourly radiosonde observations at syowa station. Journal of the Atmospheric Sciences, 65(12):3719–3735, 2008.

[99] R. Scherhag. Stratospheric temperature changes and the associated changes in pressure distribution. Journal of Meteorology, 17(6):575–583, 1960.

[100] S. Schroeder, P. Preusse, M. Ern, and M. Riese. Gravity waves resolved in ecmwf and measured by saber. Geophysical Research Letters, 36(10):L10805, 2009.

[101] D. C. Senft and C. S. Gardner. Seasonal variability of gravity wave activity and spectra in the mesopause region at urbana. J.Geophys.Res., 96(D9):17229–17264, 1991.

[102] D. E. Siskind, L. Coy, and P. Espy. Observations of stratospheric warmings and mesospheric coolings by the timed saber instrument. Geophysical Research Letters, 32(9):L09804, 2005.

[103] D. E. Siskind, S. D. Eckermann, L. Coy, J. P. McCormack, and C. E. Randall. On recent interannual variability of the arctic winter mesosphere: Implications for tracer descent. Geophysical Research Letters, 34(9):L09806, 2007.

[104] D. E. Siskind, S. D. Eckermann, J. P. McCormack, L. Coy, K. W. Hoppel, and N. L. Baker. Case studies of the mesospheric response to recent minor, major, and extended stratospheric warmings. J.Geophys.Res., 115:D00N03, 2010.

[105] A. K. Smith. Longitudinal variations in mesospheric winds: Evidence for gravity wave filtering by planetary waves. Journal of the Atmospheric Sciences, 53(8):1156–1173, 1996.

[106] C. Snyder, D. J. Muraki, R. Plougonven, and F. Zhang. Inertia gravity waves generated within a dipole vortex. Journal of the Atmospheric Sciences, 64(12):4417–4431, 2007.

[107] C. Snyder, R. Plougonven, and D. J. Muraki. Mechanisms for spontaneous gravity wave generation within a dipole vortex. Journal of the Atmospheric Sciences, 66(11):3464–3478, 2009.

[108] S. Solomon. Stratospheric ozone depletion: A review of concepts and history. Reviews of Geophysics, 37(3):275–316, 1999.

[109] L. Sun and W. A. Robinson. Downward influence of stratospheric final warming events in an idealized model. Geophysical Research Letters, 36(3):L03819, 2009.

[110] G. E. Thomas. Mesospheric clouds and the physics of the mesopause region. Reviews of Geophysics, 29(4):553–575, 1991.

[111] G. E. Thomas. Global change in the mesosphere-lower thermosphere region: has it already arrived? Journal of Atmospheric and Terrestrial Physics, 58(14):1629–1656, 1996.

[112] G. E. Thomas, J. J. Olivero, E. J. Jensen, W. Schroeder, and O. B. Toon. Relation between increasing methane and the presence of ice clouds at the mesopause, 1989.

[113] B. Thurairajah, R. L. Collins, V. L. Harvey, R. S. Lieberman, M. Gerding, K. Mizutani, and J. M. Livingston. Gravity wave activity in the arctic stratosphere and mesosphere during the 20072008 and 20082009 stratospheric sudden warming events. J.Geophys.Res., 115:D00N06, 2010.

[114] B. Thurairajah, R. L. Collins, V. L. Harvey, R. S. Lieberman, and K. Mizutani. Rayleigh lidar observations of reduced gravity wave activity during the formation of an elevated stratopause in 2004 at chatanika, alaska (65n, 147w). J.Geophys.Res., 115(D13):D13109, 2010.

[115] M. A. Tolbert and O. B. Toon. Solving the psc mystery. Science, 292(5514):61–63, 2001.

[116] C. Tsuchiya, K. Sato, T. Nasuno, A. T. Noda, and M. Satoh. Universal frequency spectra of surface meteorological fluctuations. Journal of Climate, 24(17):4718–4732, 04/04; 2011 2011; 2011.

[117] T. Tsuda, M. Nishida, C. Rocken, and R. H. Ware. A global morphology of gravity wave activity in the stratosphere revealed by the gps occultation data (gps/met). J.Geophys.Res., 105(D6):7257–7273, 2000.

[118] L. W. Uccellini and S. E. Koch. The synoptic setting and possible energy sources for mesoscale wave disturbances. Monthly Weather Review, 115(3):721–729, 1987.

[119] R. L. Walterscheid, G. G. Sivjee, and R. G. Roble. Mesospheric and lower thermospheric manifestations of a stratospheric warming event over eureka, canada (80n). Geophysical Research Letters, 27(18):2897–2900, 2000.

[120] L. Wang and M. J. Alexander. Gravity wave activity during stratospheric sudden warmings in the 20072008 northern hemisphere winter. J.Geophys.Res., 114(D18):D18108, 2009.

[121] L. Wang, D. C. Fritts, B. P. Williams, R. A. Goldberg, F. J. Schmidlin, and U. Blum. Gravity waves in the middle atmosphere during the macwave winter campaign: evidence of mountain wave critical level encounters. Annales de Geophysique, 24(4):1209–1226, 2006. J1: ANGEO.

[122] S. Wang and F. Zhang. Sensitivity of mesoscale gravity waves to the baroclinicity of jet-front systems. Monthly Weather Review, 135(2):670–688, 2007.

[123] S. Wang and F. Zhang. Source of gravity waves within a vortex-dipole jet revealed by a linear model. Journal of the Atmospheric Sciences, 67(5):1438–1455, 2010.

[124] S. Wang, F. Zhang, and C. Snyder. Generation and propagation of inertiagravity waves from vortex dipoles and jets. Journal of the Atmospheric Sciences, 66(5):1294–1314, 2009.

[125] S. Watanabe, Y. Kawatani, Y. Tomikawa, K. Miyazaki, M. Takahashi, and K. Sato. General aspects of a t213l256 middle atmosphere general circulation model. J.Geophys.Res., 113(D12):D12110, 2008.

[126] J. A. Whiteway and A. I. Carswell. Rayleigh lidar observations of thermal structure and gravity wave activity in the high arctic during a stratospheric warming. Journal of the Atmospheric Sciences, 51(21):3122–3136, 1994.

[127] J. A. Whiteway, T. J. Duck, D. P. Donovan, J. C. Bird, S. R. Pal, and A. I. Carswell. Measurements of gravity wave activity within and around the arctic stratospheric vortex. Geophysical Research Letters, 24(11):1387–1390, 1997.

[128] C. J. Wright, S. M. Osprey, J. J. Barnett, L. J. Gray, and J. C. Gille. High resolution dynamics limb sounder measurements of gravity wave activity in the 2006 arctic stratosphere. J.Geophys.Res., 115(D2):D02105, 2010.

[129] D. L. Wu and S. D. Eckermann. Global gravity wave variances from aura mls: Characteristics and interpretation. Journal of the Atmospheric Sciences, 65(12):3695–3718, 2008.

[130] D. L. Wu and J. H. Jiang. Mls observations of atmospheric gravity waves over antarctica. J.Geophys.Res., 107(D24):4773, 2002.

[131] C. Yamashita, X. Chu, H. L Liu, P. J. Espy, G. J. Nott, and W. Huang. Stratospheric gravity wave characteristics and seasonal variations observed by lidar at the south pole and rothera, antarctica. J.Geophys.Res., 114(D12):D12101, 2009.

[132] C. Yamashita, H. L Liu, and X. Chu. Gravity wave variations during the 2009 stratospheric sudden warming as revealed by ecmwf-t799 and observations. Geophysical Research Letters, 37(22):L22806, 2010.

[133] C. Yamashita, H. L Liu, and X. Chu. Responses of mesosphere and lower thermosphere temperatures to gravity wave forcing during stratospheric sudden warming. Geophysical Research Letters, 37(9):L09803, 2010.

[134] M. Yoshiki and K. Sato. A statistical study of gravity waves in the polar regions based on operational radiosonde data. J.Geophys.Res., 105(D14):17995–18011, 2000.

[135] F. Zhang. Generation of mesoscale gravity waves in upper-tropospheric jetfront systems. Journal of the Atmospheric Sciences, 61(4):440–457, 2004.

[136] F. Zhang, S. Koch, C. Davis, and M. Kaplan. A survey of unbalanced flow diagnostics and their application. Advances in Atmospheric Sciences, 17(2):165–183, 2000.

[137] F. Zhang and S. E. Koch. Numerical simulations of a gravity wave event over ccope. part ii: Waves generated by an orographic density current. Monthly Weather Review, 128(8):2777–2796, 2000.

[138] F. Zhang, S. E. Koch, and M. L. Kaplan. Numerical simulations of a large-amplitude mesoscale gravity wave event. Meteorology and Atmospheric Physics, 84(3):199–216, 2003.

Appendix A

Comparison of Gravity Wave Variations during the 2009 and the 2010 SSWs

The 2009 SSW is caused by planetary wave wavenumber 2 and the 2010 SSW is caused by planetary wavenumber 1. Here, gravity wave variations are compared between the 2009 SSW and the 2010 SSW as the preliminary result of further statistical study. Figures A.1 and A.2 show temperature, temperature anomaly, and zonal wind in 2009 and 2010, respectively. Temperature anomalies for the 2009 and 2010 SSWs are estimated by subtracting temperature on January 1, 2009 and 2010, respectively.

Wind reversal at 50 km occur on ∼January 21 and at 30 km on ∼January 23 in 2009. Temperature increases more than 50 K on January 23 around 30 km for the 2009 SSW. For the 2010 SSW, the stratospheric temperature increases ∼40K starting around January 20, but the wind reversal at 30 km occurs on January 30, 2010. The magnitudes of SSW are larger in 2009 than in 2010, but the durations of SSW are longer in 2010 than in 2009.

Figures A.3 and A.4 show the divergence of EP flux and residual circulations. The episodes of multiple EP flux divergence exist from January 15 to January 30 in 2010. In contrast to 2010, one large EP flux divergence occurs around January 20 in 2009. These results indicate the differences between the 2009 SSW and the 2010 SSW.

Figures A.5 and A.6 illustrate the time variations of GW-Ep in 2009 and 2010, respectively. In 2009, GW-Ep peaks on around January 5 and January 16 as studied in Chapters 3 and 4. The results are slightly different because of the different latitude. GW-Ep peaks on around January 23 in 2010. The peak magnitude of GW-Ep associated with the 2010 SSW is weaker than that during

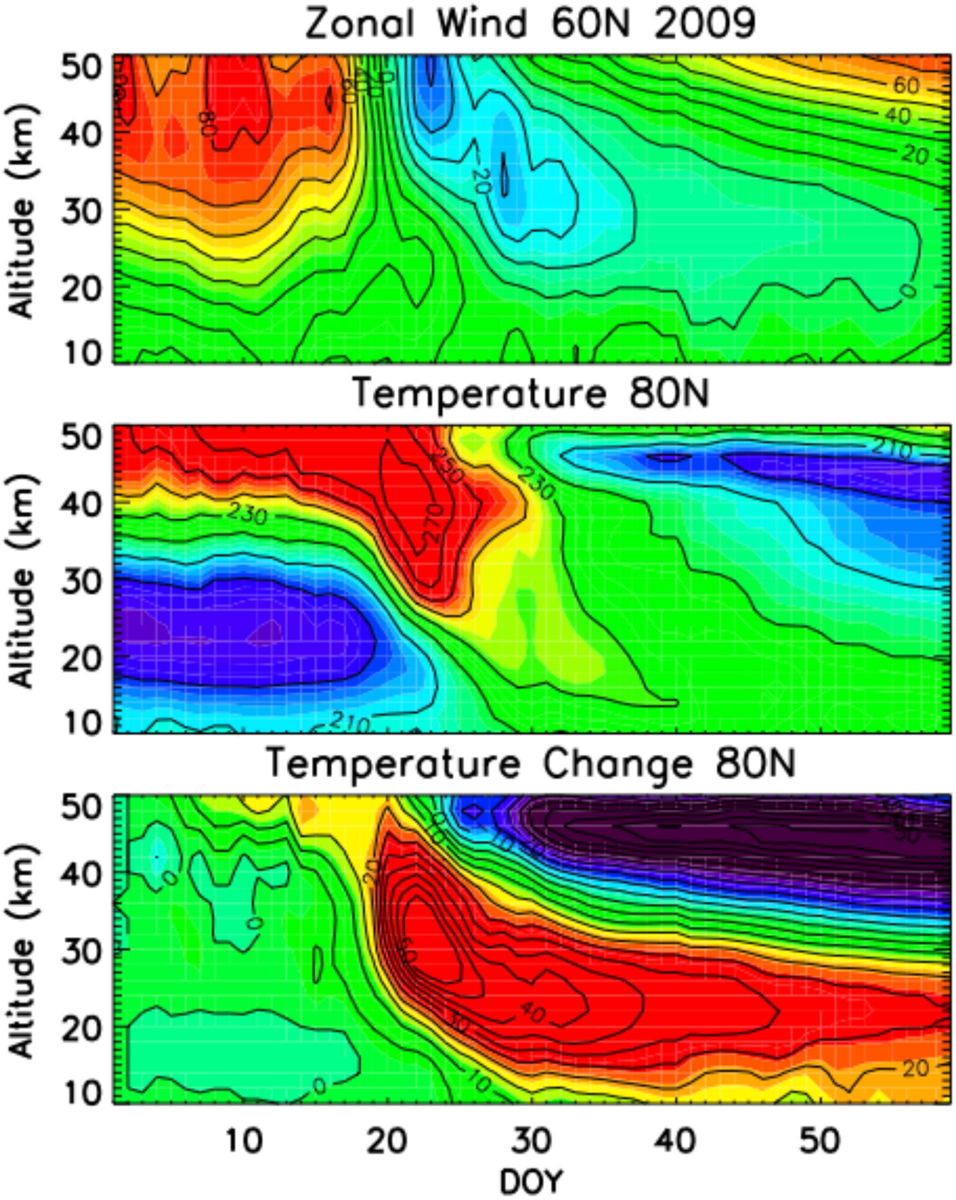
Zonal Wind 60N 2009

Temperature 80N

Temperature Change 80N

Figure A.1: Zonal mean (top) zonal wind at 60°N, (middle) temperature at 80°N, (bottom) temperature anomaly (change) at 80°N associated with the 2009 SSW.

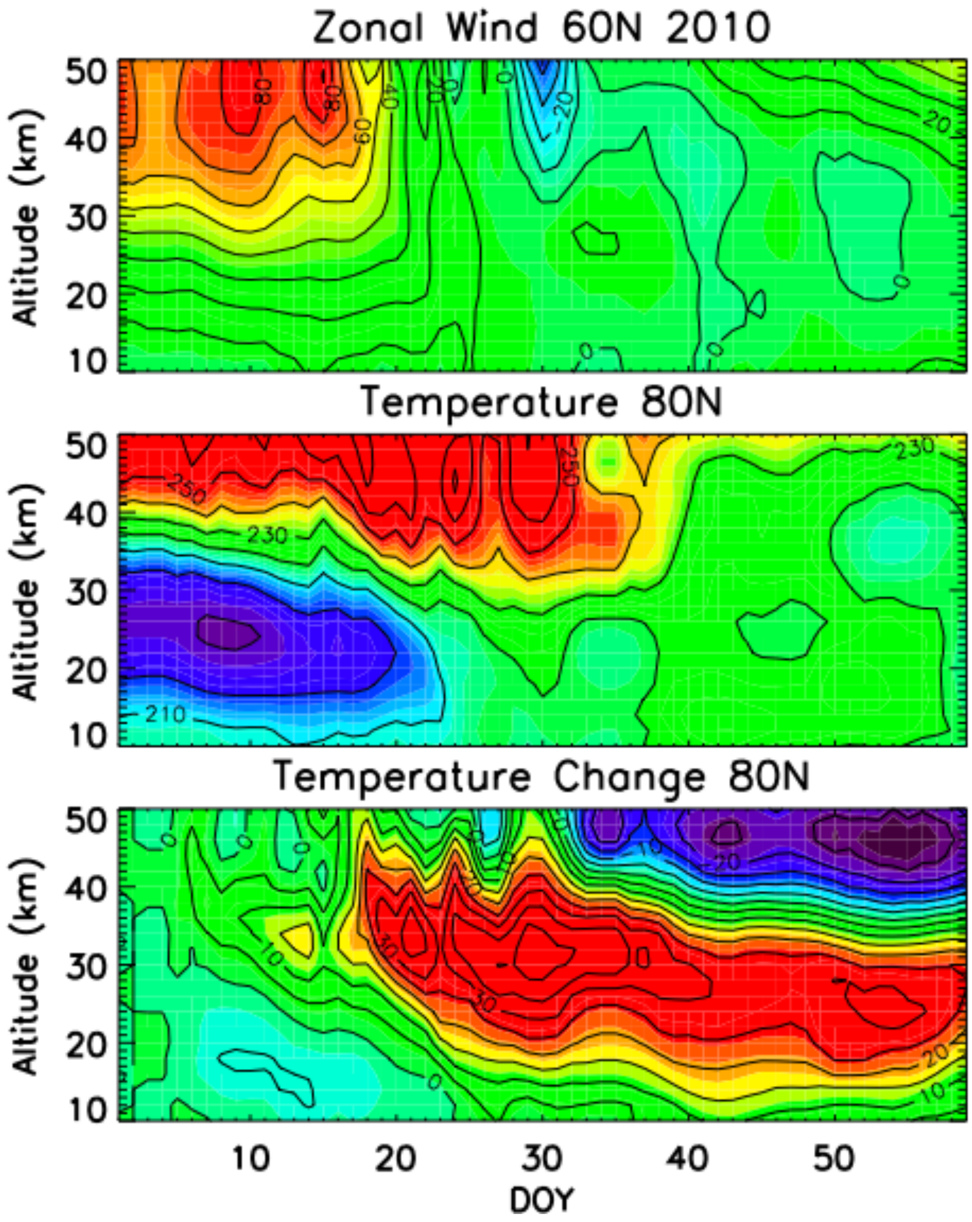

Figure A.2: Zonal mean (top) zonal wind at 60°N, (middle) temperature at 80°N, (bottom) temperature anomaly (change) at 80°N associated with the 2010 SSW.

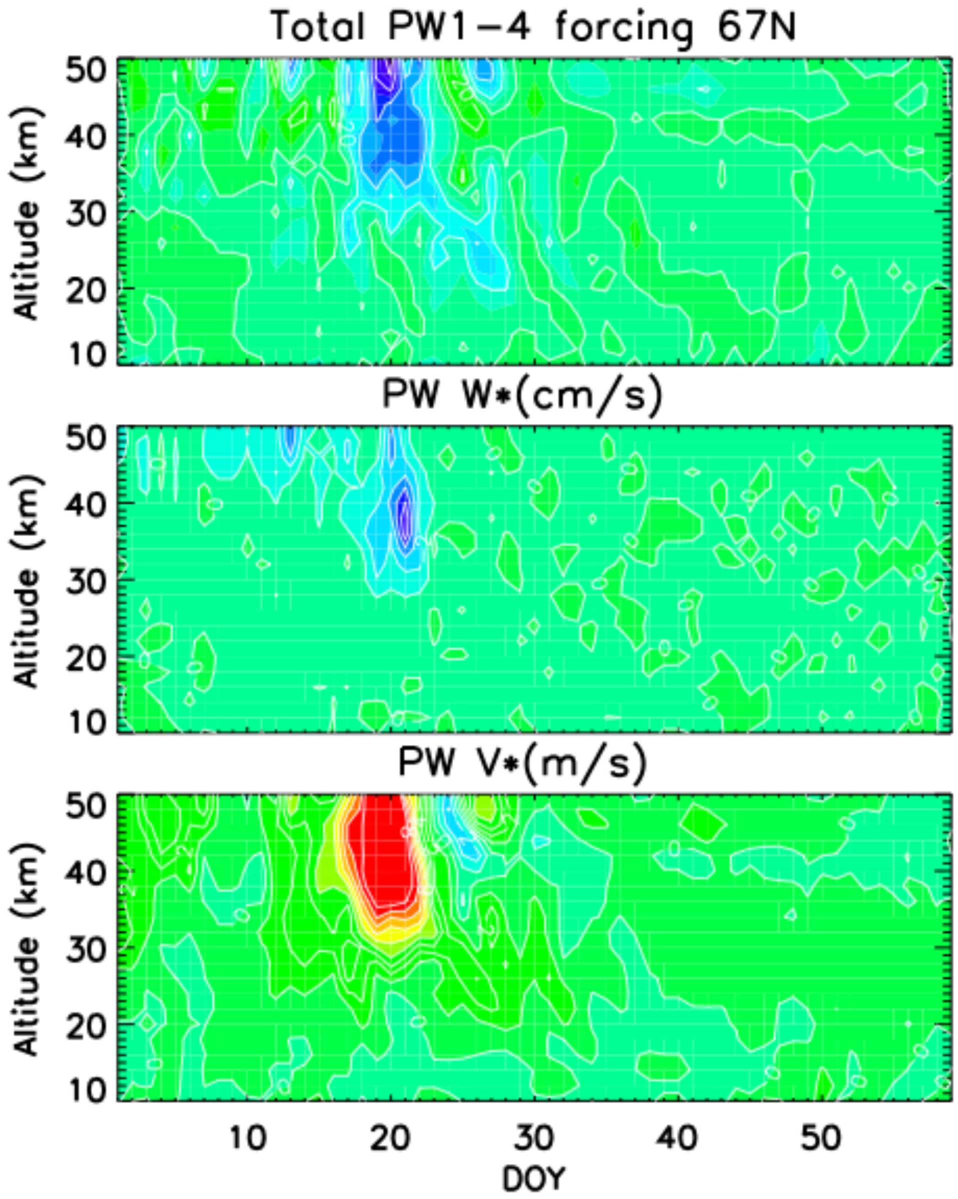

Figure A.3: (top) EP flux divergence, (middle) vertical residual circulation, and (bottom) meridional residual circulation calculated with planetary wavenumber 1-4 at 67°N during the 2009 SSW.

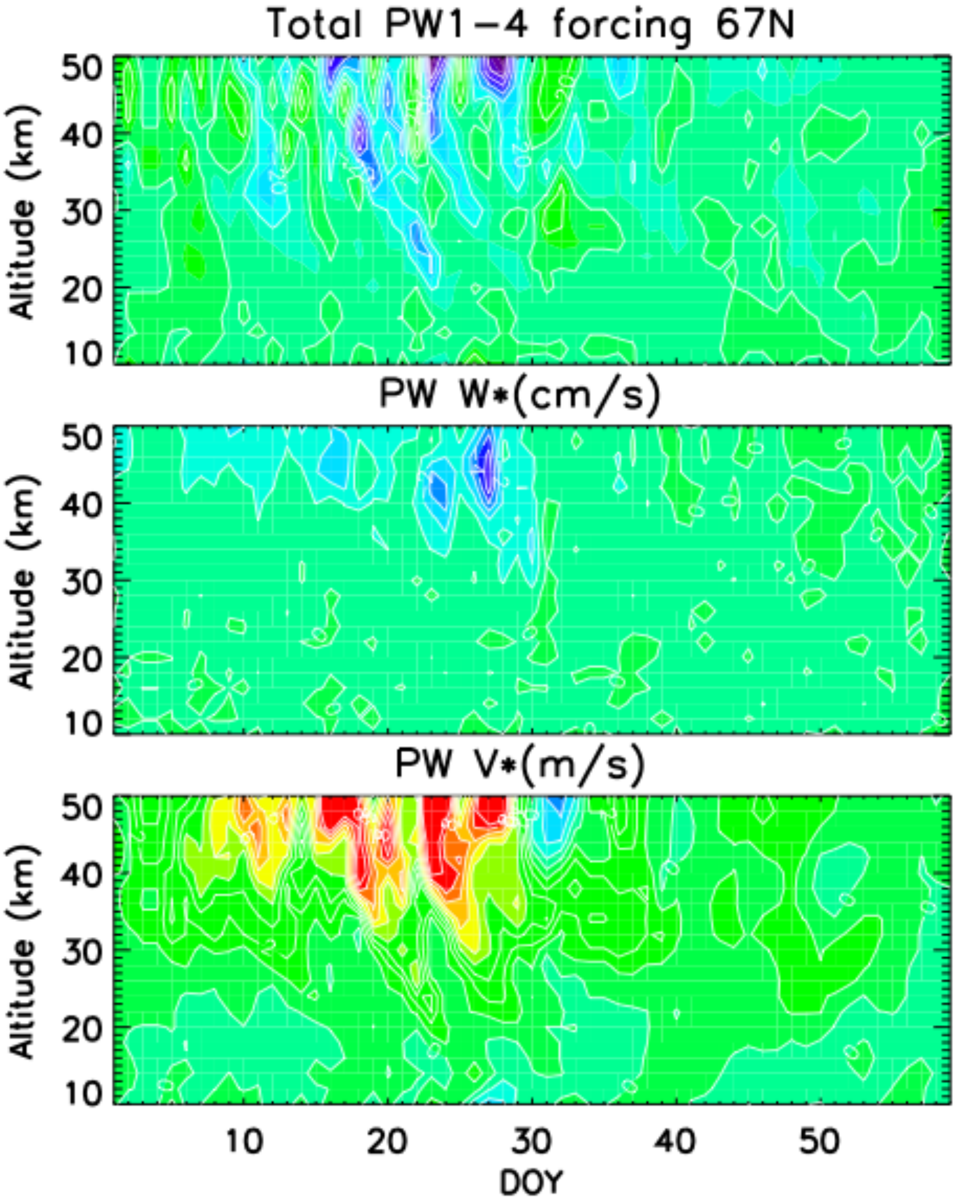

Figure A.4: (top) EP flux divergence, (middle) vertical residual circulation, and (bottom) meridional residual circulation calculated with planetary wavenumber 1-4 at 67°N during the 2010 SSW.

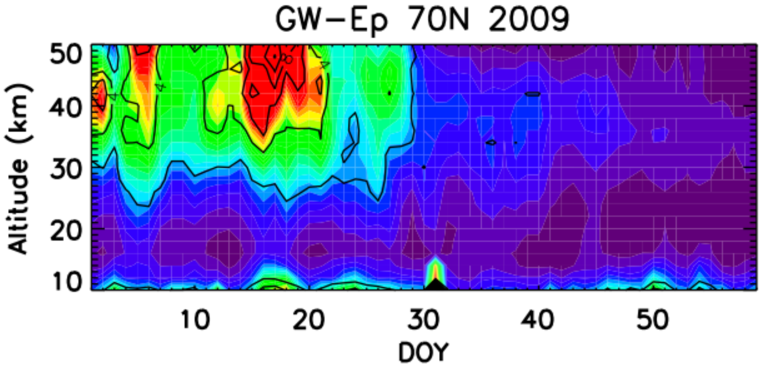

Figure A.5: Variations of daily-zonal mean GW-Ep at 70°N associated with the 2009 SSW.

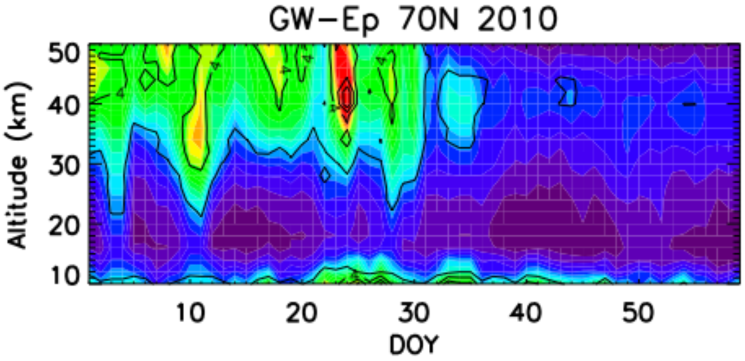

Figure A.6: Variations of daily-zonal mean GW-Ep at 70°N associated with the 2010 SSW.

the 2009 SSW. In 2010, multiple peaks of GW-Ep are captured on January 10, 20, 25, and 30, corresponding to the large EP flux divergences.

Summary

GW-Ep variations in 2010 also correspond to the planetary wave enhancements. However, the magnitude of GW-Ep is about factor of two smaller than the peak magnitude of GW-Ep in 2009. Future investigations should be directed towards the studies of characteristics of gravity waves and their potential generation mechanisms.